nature portfolio

https://doi.org/10.1038/s41586-026-11136-9

Supplementary information

Rh^{3+} stabilized in KRh@MFI catalyses regioselective hydroformylation

In the format provided by the authors and unedited

Supplementary Information

Rh^{3+} stabilized in KRh@MFI catalyses regioselective hydroformylation

Minjie Zhao[a], Reisel Millan[a], Alina Skorynina[b], Laura Simonelli[b], Miguel Lopez Haro[c], Jose Juan Calvino[c], Patricia Concepción[a,*], Avelino Corma[a,*]

Affiliations:

[a] *Instituto de Tecnología Química, Consejo Superior de Investigaciones Científicas-Universitat Politècnica de València, Avenida de los Naranjos s/n, 46022 Valencia, Spain.*

[b] *CELLS - ALBA Synchrotron Radiation Facility, Carrer de la Llum 2-26, 08290 Cerdanyola del Vallès, Spain.*

[c] *Departamento de Ciencia de los Materiales e Ingeniería Metalúrgica y Química Inorgánica. Facultad Ciencias. Universidad de Cádiz. Campus Rio San Pedro. Puerto Real, 11510-Cádiz, Spain.*

*Corresponding author.

Email: acorma@itq.upv.es (Avelino Corma); pconcepc@itq.upv.es (Patricia Concepción).

Table of content

1. Synthesis of KRh@MFI samples 4
1.1. Chemical reagents. 4
1.2. Catalyst synthesis. 4
1.3. Characterization methods. 5
1.4. DFT calculation methods. 6
2. Alkenes hydroformylation (Long-chain α-olefin, LAO) 9
2.1. Characterizations of Rh@MFI-Cal and KRh@MFI-Cal catalysts before reaction 9
2.2. Hot-filtration experiments on Rh@MFI-Cal and KRh@MFI-Cal catalysts. 14
2.3. HAADF-STEM and iDPC images of KRh@MFI-Cal catalyst after 1-hexene hydroformylation reaction 16
2.4. 1-Hexene hydroformylation (C6 LAO) 18
2.5. Hydroformylation of trans-2-hexene on KRh@MFI-Cal catalyst 20
2.6. Hydroformylation of trans-3-hexene on KRh@MFI-Cal catalyst 22
2.7. Reaction order of 1-hexene hydroformylation and isomerization 24
2.8. 1-Hexene isomerization on homogeneous and heterogeneous Rh catalysts 27
2.9. CO pretreatment on KRh@MFI-Cal catalyst for 1-hexene hydroformylation and isomerization 29
2.10. 1-Hexene hydroformylation on KRh@MFI-Cal, KRh@MFI-CalRed-CO and KRh@MFI-CalRed-CO-500MP catalysts 31
2.11. Hydroformylation on homogeneous and heterogeneous systems with DFT calculations 33
2.12. 1-Hexene hydroformylation in the presence of organic molecules 46
2.13. Spectroscopic characterization of spent samples 49
2.14. Stability of Rh active sites and theoretical IR analysis 51
2.15. Catalytic performance of 1-hexene hydroformylation on KRh@MFI-Cal and KRh@MFI-Cal-500MP catalysts 54
2.16. Exclude mass transport limitations 56
2.17. Apparent activation energy of KRh@MFI-Cal catalyst for 1-hexene hydroformylation and isomerization 57
2.18. Apparent activation energy of KRh@MFI-Cal catalyst for 1-hexene hydroformylation and isomerization in the presence of N-methylpyrrolidine 58
2.19. Apparent activation energy of $RhHCO(PPh_3)_3$ catalyst for 1-hexene hydroformylation 59
2.20. Reaction orders of 1-hexene, CO and H_2 on KRh@MFI-Cal, KRh@MFI-CalRed-CO and KRh@MFI-Cal-500MP catalysts 61
2.21. Optimum loading of organic additives (MP and NMP) in 1-hexene hydroformylation 62
2.22. 1-Octene hydroformylation (C8 LAO) 69
2.23. Apparent activation energy of KRh@MFI-Cal catalyst for 1-octene hydroformylation 71
2.24. 1-Decene hydroformylation (C10 LAO) 73
2.25. 1-Decene hydroformylation at scaled-up concentration on KRh@MFI-Cal catalyst

in the presence of NMP or MP 75
2.26. Apparent activation energy of KRh@MFI-Cal catalyst for 1-decene hydroformylation 77
2.27. Apparent activation energy of $RhHCO(PPh_3)_3$ catalyst for 1-decene hydroformylation 79
3. Appendix 96
3.1. Compare $RhHCO(PPh_3)_3$ and $RhCl(PPh_3)_3$ catalyst 96
3.2. XAS Analysis 97
3.3. Quantification of Rh^{3+}/Rh^{+} species ratio based on IR-CO 98
3.4. Quantification of Rh^{3+}/Rh^{+} species ratio based on XAS 105
3.5. 1-Decene hydroformylation on Rh@zeolite with different topology type zeolite . 113
3.6. Hydroformylation of bulky olefins over KRh@MFI-Cal 119
3.7. Summary of the identification of Rh species by IR-CO 122
4. Reference 123

1. Synthesis of KRh@MFI samples

1.1. Chemical reagents.

All chemicals and materials were obtained from commercial sources and used without further purification unless otherwise specified. Tetrapropylammonium bromide (TPABr), tetraorthoethylsilicate (TEOS), ethylenediamine (EDA), rhodium (III) chloride hydrate ($RhCl_3 \cdot 3H_2O$), potassium hydroxide (KOH), 1-hexene, 1-octene, 1-decene, decane, isooctane, toluene, acetone, 1-methyl-2-pyrrolidone (NMP), furfural, 5-methyl-furfural, N-methylpyrrolidine (MP), cyclopentanone, N-methyldiphenylamine, 1-benzylpyrrolidine-2,5-dione, rhodium(I) dicarbonyl acetylacetonate, rhodium(III) acetylacetonate and commercial homogeneous Wilkinson-type catalyst $RhHCO(PPh_3)_3$ and $RhCl(PPh_3)_3$ were purchased from Sigma Aldrich, 99.9% purity. Anion exchange resin (Amberlite® IRN-78) was purchased from Thermo Scientific. Tetrapropylammonium hydroxide (TPAOH) was obtained by ionic exchange of TPABr with anion exchange resin. Deionized (DI) water from Milli-Q integral water purification system (Millipore, 18.2 $M\Omega \cdot cm^{-1}$).

1.2. Catalyst synthesis.

KRh@MFI is synthetized by conventional hydrothermal synthesis with tetraorthoethylsilicate (TEOS) as silica source and tetrapropylammonium hydroxide (TPAOH) as organic template. For the synthesis of KRh@MFI, molar ratio SiO_2: TPAOH: H_2O: Rh: K=1: 0.4: 25: 0.0012: 0.09 are used, representing KRh@MFI with 0.2wt% Rh and 1wt% K loading. Normally, 0.263g $RhCl_3 \cdot 3H_2O$ is dissolved in 80g H_2O, then 20g EDA is added and stirring overnight until a clear light-yellow colour of Rh-EDA solution. For the synthesis of KRh@S-1, for example, 8.32g TEOS, 8g TPAOH (40wt%), 20g Milli-Q water, 0.2g KOH are mixed and kept stirring overnight. Then 4.67g Rh-EDA is added into the clear zeolite synthesis gel and transferred to a 35mL Teflon-lined autoclave and heated to 100 °C under static for 48h for crystallization. When the crystallization was finished, the solid product was collected by filtration and washed thoroughly with distilled water and dried in air at 100 °C. The dried sample is calcined in a tubular oven with 50 mL/min air at a heating rate of 1.5 °C/min to 550 °C and maintain 6 hours. The obtained sample is stored in air and aged naturally inside glass bottle for 60 days before activity tests and characterizations, this sample is named as

KRh@MFI-Cal. For the preparation of KRh@MFI-CalRed-CO, the KRh@MFI-Cal sample is firstly ex-situ reduced in a tubular oven with 50 mL/min pure H_2 at a heating rate of 10 °C/min to 600 ºC for 3h. The reduced sample was then transferred into a glove box and loaded into a batch reactor. Prior to the catalytic reaction, the reactor is pressurized with 5 bar H_2 and maintained at 150 ºC under stirring for 1h, after which the H_2 is released. Subsequently, the reactor is pressurized with 5 bar of pure CO and stirred at 90 ºC for 2h. For the preparation of KRh@MFI-Cal-CO/H_2, the KRh@MFI-Cal is loaded into batch reactor together with 4 mL of toluene. The reactor was then pressurized with 40 bar CO/H_2/Ar and maintained under stirring at 80 ºC for 2h. Rh@MFI-Cal is prepared similarly to KRh@MFI-Cal without KOH in the synthesis gel and hydrothermally crystallized at 175 ºC for 96h.

1.3. Characterization methods.

Samples for electron microscopy studies were prepared by dropping the suspension of KRh@MFI catalysts, using CH_2Cl_2 as the solvent, directly onto holey-carbon-coated Cu grids. The measurements were performed using a JEOL 2100F microscope operating at 200 kV, both in transmission (TEM) and scanning-transmission modes (STEM). HR-HAADF-STEM and iDPC imaging were performed using a double aberration-corrected, monochromated FEI Titan3 Themis 60-300 microscope operating at 300 kV. Specifically, 2048 x 2048 HAADF-iDPC image pairs were acquired with a convergence angle of 18.6 mrad and collection angles of 48-198 mrad. This configuration optimized signal collection on the HAADF and FEI DF4 detectors. To minimize electron beam damage, a fast image recording protocol was employed, utilizing a beam current of 10 pA, a 1.25-µs dwell time (corresponding to a dose rate of 2500 $e^-/Å^2$), and automated fine-tuning alignment of A1 and C1 using OptiSTEM software. Inductively Coupled Plasma Mass Spectrometry (ICP) was carried out with a Varian 715-ES ICP-Optical Emission spectrometer and analyzed with a SCHN FISONS elemental analyzer. Powder X-ray diffraction was performed with a HTPhilips X'Pert MPD diffractometer equipped with a PW3050 goniometer using Cu Kα radiation and a multisampling handler ($\lambda = 0.15406$ nm). IR spectra of CO adsorbed on KRh@MFI-Cal and corresponding after reaction samples were recorded with Bruker 70V spectrometer under -65 ºC.

In-situ and *ex-situ* X-ray absorption spectra (XAS) spectroscopy was acquired at CLÆSS beamline 22 of the ALBA synchrotron[1]. The synchrotron radiation generated by a multipole wiggler source

was monochromatized by a Si(311) double-crystal monochromator. The beam was focused horizontally and vertically by a Pt-coated toroidal mirror resulting in a spot size of 450x450 μm^2. Rh K-edge spectra were collected under ambient conditions in transmission mode for the standard reference materials (Rh foil, Rh_2O_3 and $Rh(CO)_2(acac)$) and in fluorescence mode for the catalysts using a multi-channel silicon drift detector (SDD). Several XAS repeats were collected to ensure reproducibility and statistics. The KRh@MFI-Cal and KRh@MFI-Cal-500MP after reaction samples and KRh@MFI-Cal-CO/H_2 were loaded in liquid phase in the NMR quartz tube. The KRh@MFI-CalRed-CO catalyst was pressed into a 5 mm diameter pellet and placed in a solid-gas reactor available at the beamline. The sample was first reduced under a flow of pure H_2 at 400 °C for 2 hours, followed by a treatment in pure CO at 90 °C and 5 bar for an additional 2 hours. Finally cooling the sample to room temperature under a He atmosphere at 1 bar. X-ray absorption spectra were continuously collected throughout all experimental steps for *in-situ* experiments. All XAS data were processed using the Demeter package[2]. Extended X-ray absorption fine structure (EXAFS) were extracted using the AUTOBK algorithm employing a spline in the range of 0 to 15.9 $Å^{-1}$ having an R_{bkg} of 1.05. The FEFF6 code[3,4] was used for scattering path generation, and multi (k^1, k^2, k^3)-weighted fits of the data were carried out in r-space over r- and k- ranges as indicated in the Supporting Information. The S_0^2 value was set to 0.9, and a global E_0 was employed with the initial E_0 value set to the maximum inflection point of the rising edge. Single scattering paths were fit in terms of a Δreff and σ^2, which represent the deviation from the expected interatomic distances and the structural disorder, respectively. Co-linear Rh-C=O paths were fit with a common Δreff and σ^2. To assess the goodness of the fits both the R_{factor} (%R) and the reduced χ^2 (χ^2_v) were minimized, with a number of variables always below the limit imposed by the Nyquist theorem ($\frac{2\Delta k \Delta r}{\pi}$), ensuring that the data was not over-fit. Best fit models were determined using a grid search with fixed values for path coordination numbers (CN) by employing Larch, the Python implementation of Artemis[5].

1.4. DFT calculation methods.

Periodic density functional theory (DFT) calculations were performed to describe Rh species confined within the MFI zeolite framework using the Perdew-Burke-Ernzerhof (PBE) exchange-correlation functional within the generalized gradient approximation (GGA)[6,7], as implemented in

the Vienna *ab initio* Simulation Package (VASP, version 5.4.4)[8]. The valence electronic density was expanded in a plane-wave basis set with a kinetic energy cutoff of 520 eV. Core-valence interactions were described using the projector augmented-wave (PAW) method[9]. All calculations were spin-polarized. Brillouin zone integrations were carried out using Γ-point sampling, which is sufficient for the large periodic MFI supercell employed.

The MFI zeolite framework was modelled using a periodic supercell in which one Si atom in the sinusoidal channel was removed and a H atom was added to one or three out of the four uncoordinated O atoms, thus leaving one or three negative charges, respectively. Subsequently Rh species were located in the defects, coordinated to the previously mentioned siloxy species. Hydrides species were created by one H on the Rh and one H atom on the siloxy forming a silanol group. In the case of Rh^{3+} to four H atoms were added, one on Rh and the rest on siloxy oxygen atoms. The framework atoms were fully relaxed unless otherwise stated. Geometry optimizations were performed using a conjugate-gradient algorithm until the residual forces on all atoms were below 0.01 eV $Å^{-1}$.

Transition state (TS) structures were located using the DIMER method[10], and vibrational frequencies were calculated numerically by finite differences to confirm the nature of stationary points (zero imaginary frequencies for minima and a single imaginary frequency for transition states). Dispersion interactions were accounted for using Grimme's D3 correction with Becke-Johnson damping[11].

For each elementary step, the total energies of the reactant complex (E(R)), transition state (E(TS)), and product complex (E(P)) were obtained, including zero-point energy (ZPE) corrections. Unless otherwise stated, all reported energies throughout the text correspond to ZPE-corrected values.

The absolute Gibbs free energy (G) of each species was computed as:

$$G = E_{tot} + Z_{zpe} + RT + E_{vib} - TS_{vib}$$

where E_{tot} is the electronic energy obtained from the DFT calculation, E_{ZPE} is the zero-point energy correction, E_{vib} is the vibrational thermal energy contribution, and S_{vib} is the vibrational entropy. The zero-point energy and vibrational contributions to the energy and entropy were calculated within the harmonic approximation using the vibrational frequencies ν_i obtained from the DFT calculations:

$$E_{zpe} = \sum_{i=1}^{3N-6} \frac{1}{2} h\nu_i$$

$$E_{vib} = R \sum_{i=1}^{3N-6} \frac{h\nu_i}{k_B \left(e^{h\nu_i/k_B T} - 1\right)}$$

$$S_{vib} = R \sum_{i=1}^{3N-6} \left[\frac{h\nu_i}{k_B T \left(e^{h\nu_i/k_B T} - 1\right)} - ln(1 - e^{h\nu_i/k_B T})\right]$$

For gas-phase molecules and the complex systems, translational and rotational contributions to the energy and entropy were also included. The translational and rotational thermal energy contributions are given by:

$$G = E_{tot} + Z_{zpe} + E_{vib} + E_{rot} + E_{trans} + RT - T(S_{vib} + S_{rot} + S_{trans})$$

where $E_{rot} = E_{trans} = 3/2RT$, and the rotational and translational contributions to the entropy are given by:

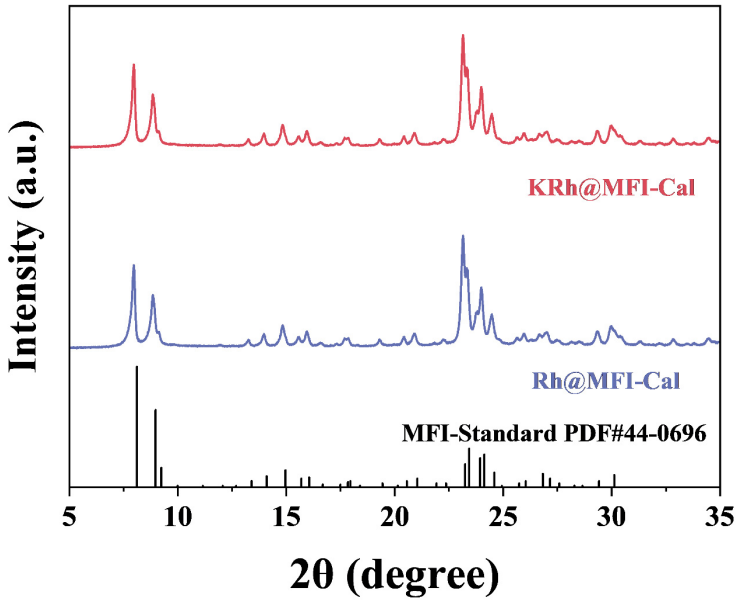
$$S_{rot} = R\left\{ln\left[\frac{\sqrt{\pi I_A I_B I_C}}{\sigma} \left(\frac{2\Pi k_B T}{h^2}\right)^{3/2}\right] + \frac{3}{2}\right\}$$

$$S_{trans} = R\left\{ln\left[\left(\frac{2\Pi M k_B T}{h^2}\right)^{3/2} V\right] + \frac{3}{2}\right\}$$

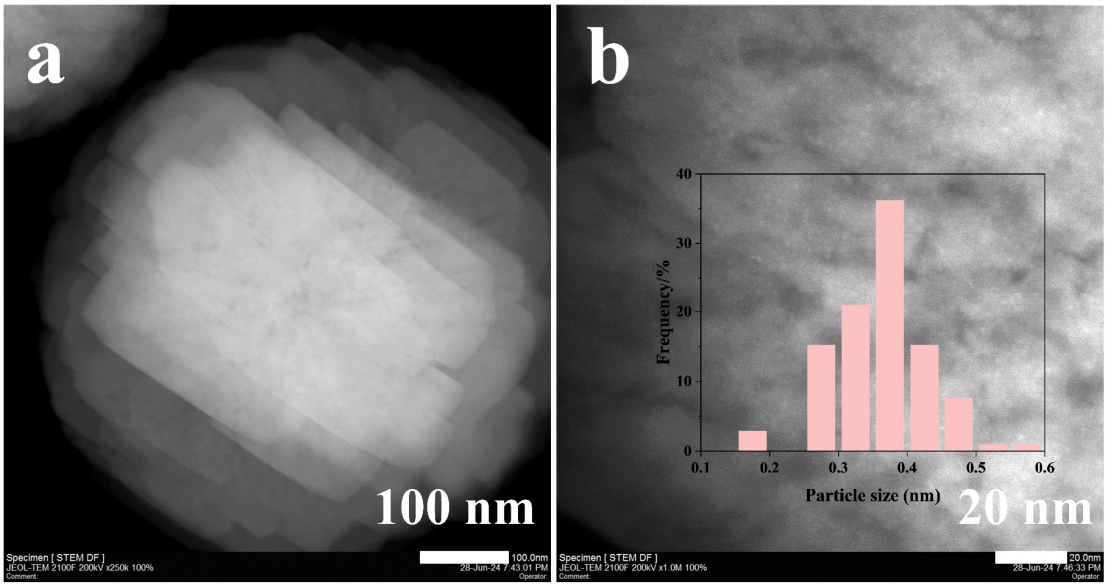
To improve the accuracy of the calculated vibrational frequencies and enable a more reliable comparison with experimental infrared (IR) spectra, additional cluster-model calculations were performed using the hybrid PBE0 exchange-correlation functional as implemented in the ORCA quantum chemistry package (version 6.1.0)[12]. Vibrational frequencies were calculated numerically using a partial Hessian approach, in which only the carbon and oxygen atoms of the CO ligands were included in the dynamical matrix. Geometry optimizations for selected reaction intermediates and transition states along the reaction mechanism were also carried out at the PBE0 level using ORCA. Calculations on the gas phase complex systems were also performed with PBE0 functional in ORCA.

2. Alkenes hydroformylation (Long-chain α-olefin, LAO)

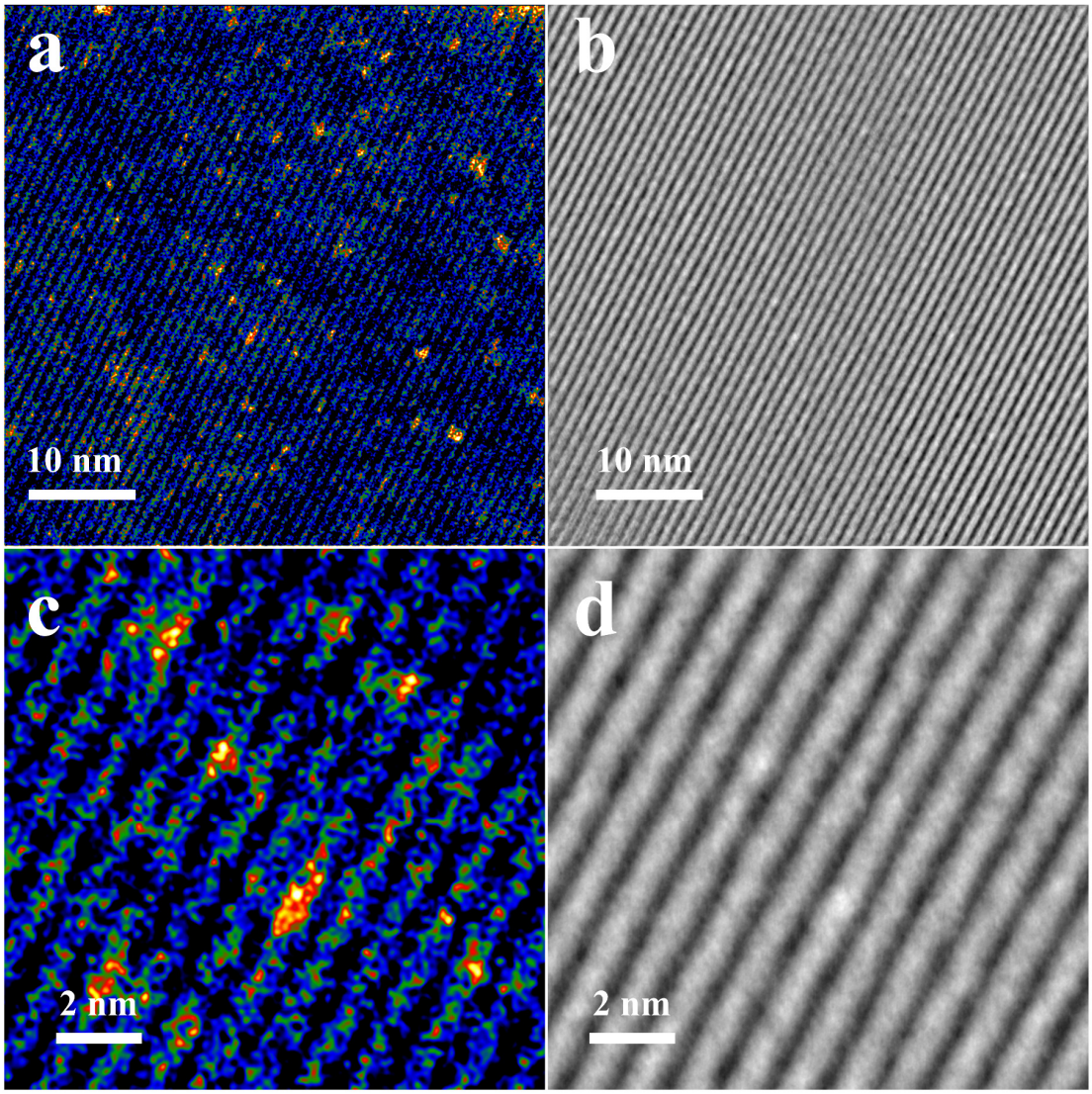
2.1. Characterizations of Rh@MFI-Cal and KRh@MFI-Cal catalysts before reaction



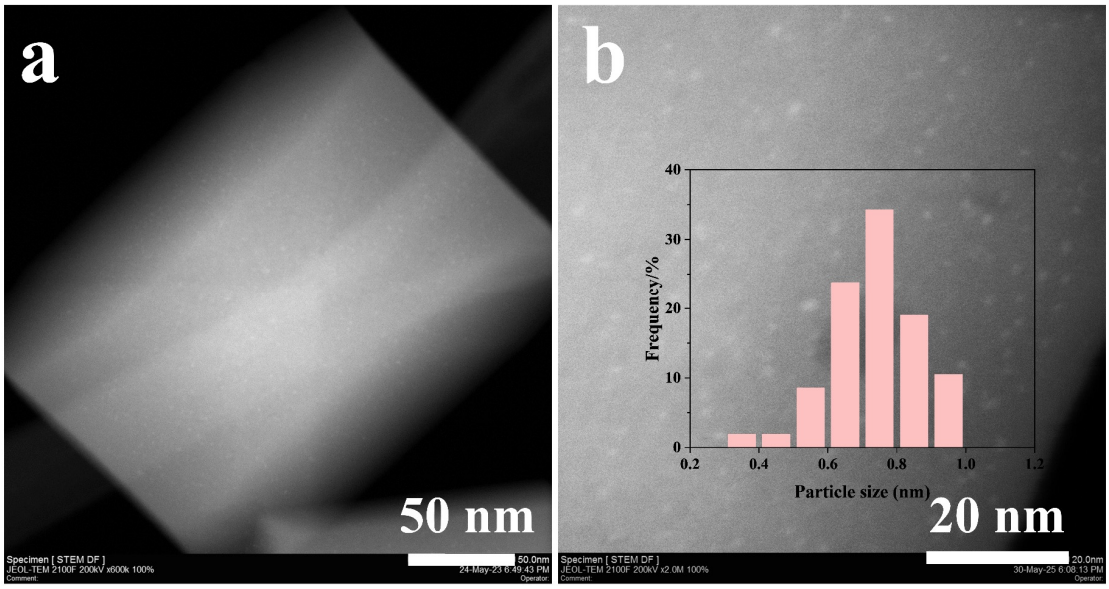
Supplementary Fig. 1. X-ray Diffraction results. XRD of KRh@MFI-Cal and Rh@MFI-Cal.



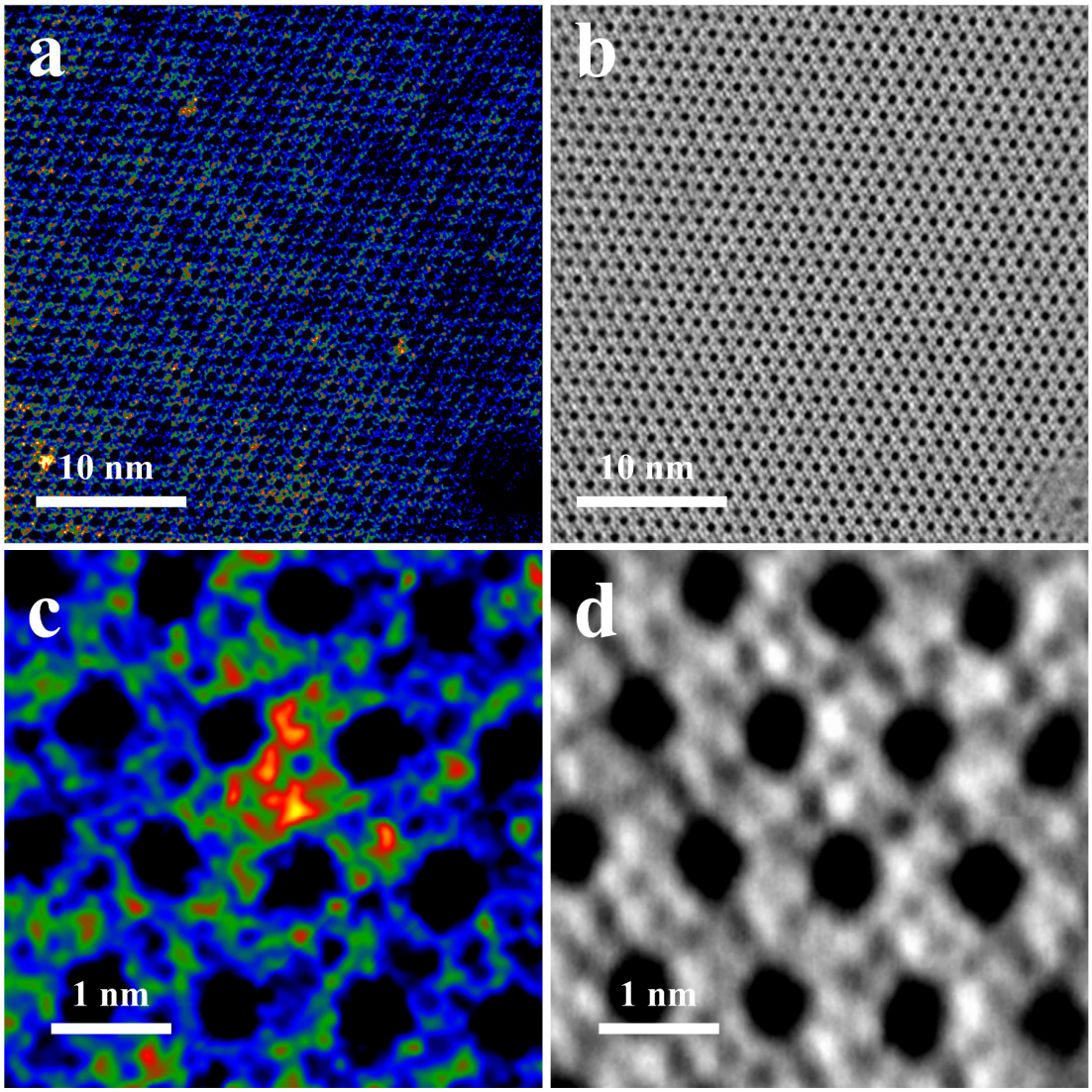
Supplementary Fig. 2. Microscopic results. STEM images of KRh@MFI-Cal.



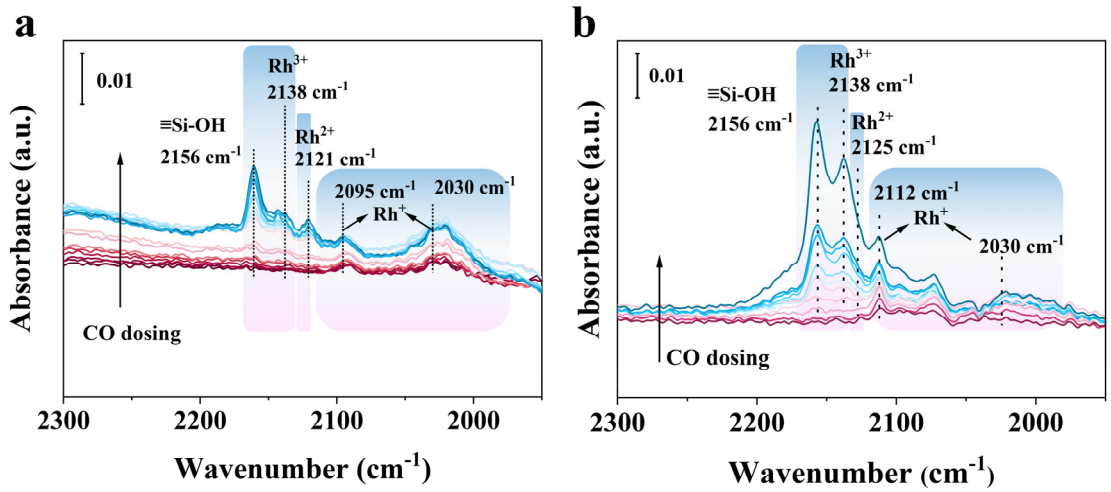
Supplementary Fig. 3. High-resolution high-angle annular dark-field scanning transmission electron microscopy (HR-HAADF-STEM) combined with integrated differential phase contrast (iDPC) imaging of fresh sample. (a, c) HAADF-STEM and (b, d) iDPC images of KRh@MFI-Cal.



Supplementary Fig. 4. Microscopic results. STEM images of Rh@MFI-Cal.

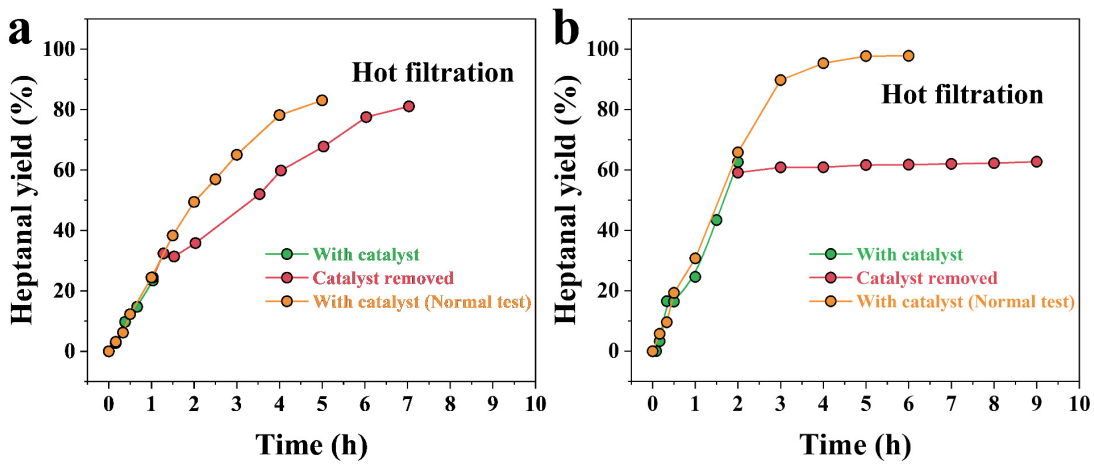


Supplementary Fig. 5. High-resolution high-angle annular dark-field scanning transmission electron microscopy (HR-HAADF-STEM) combined with integrated differential phase contrast (iDPC) imaging of fresh sample. (a, c) HAADF-STEM and (b, d) iDPC images of Rh@MFI-Cal.



Supplementary Fig. 6. IR-CO results. IR-CO at −65 ºC and at increasing CO coverage (0.01-2 mbar) for (a) KRh@MFI-Cal and (b) Rh@MFI-Cal (Taken from ref [13]) samples.

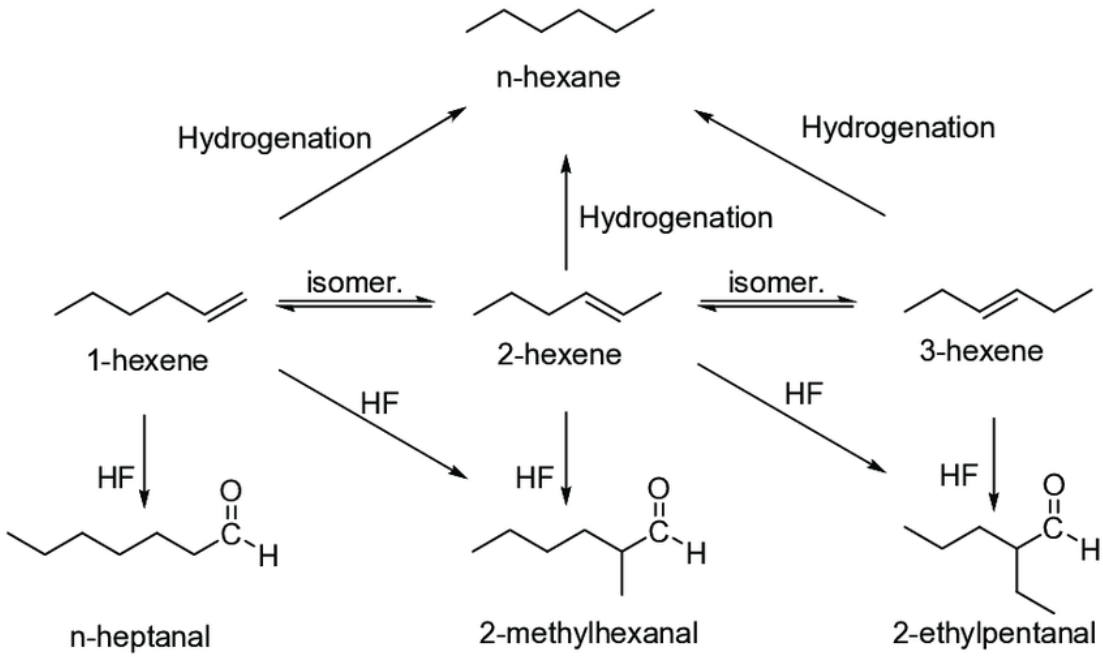
2.2. Hot-filtration experiments on Rh@MFI-Cal and KRh@MFI-Cal catalysts.



Supplementary Fig. 7. Rh stability tests. Hot-filtration experiments on Rh@MFI-Cal (a) and KRh@MFI-Cal (b) catalysts. Reaction condition: 1 mmol LAO, 20 mg catalyst (0.00038 mmol Rh), 20 mg decane (internal standard), 4 mL toluene, 40 bar $CO/H_2/Ar$ (45/45/10 vol%), 80 °C, 800 rpm.

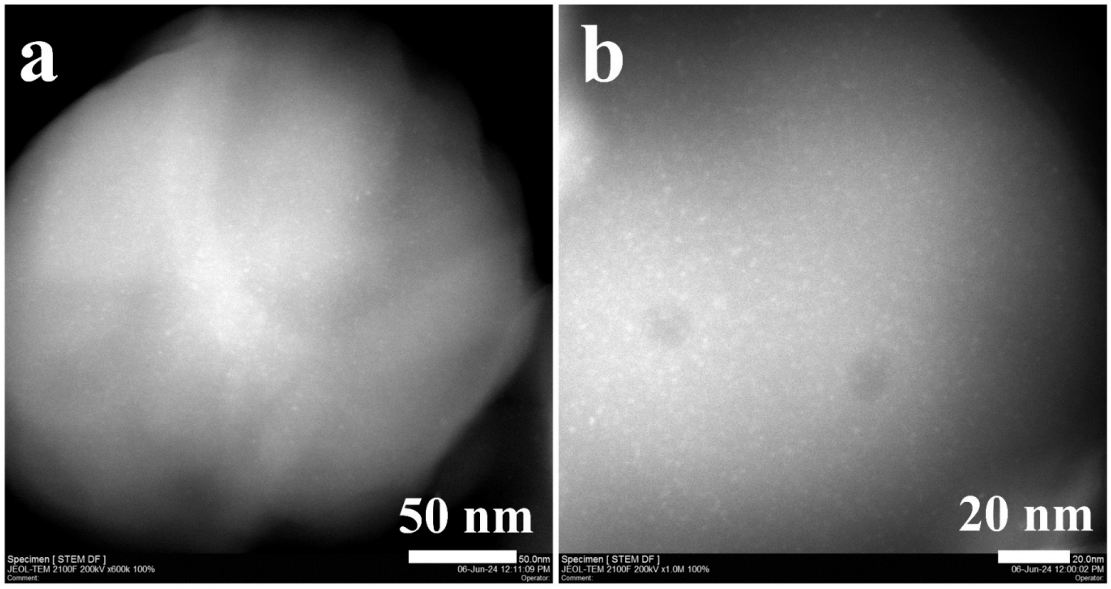
Notes: Rh is readily leached out from the Rh@MFI-Cal catalyst during 1-hexene hydroformylation, where Rh leaching is effectively suppressed on KRh@MFI-Cal. As demonstrated by the catalytic results in Supplementary Fig. 8 and 11a, b, the leached Rh species could catalyze homogeneous hydroformylation with significantly lower aldehyde regioselectivity.

Therefore, suppressing Rh leaching during the reaction is essential for maintaining the high aldehyde regioselectivity.

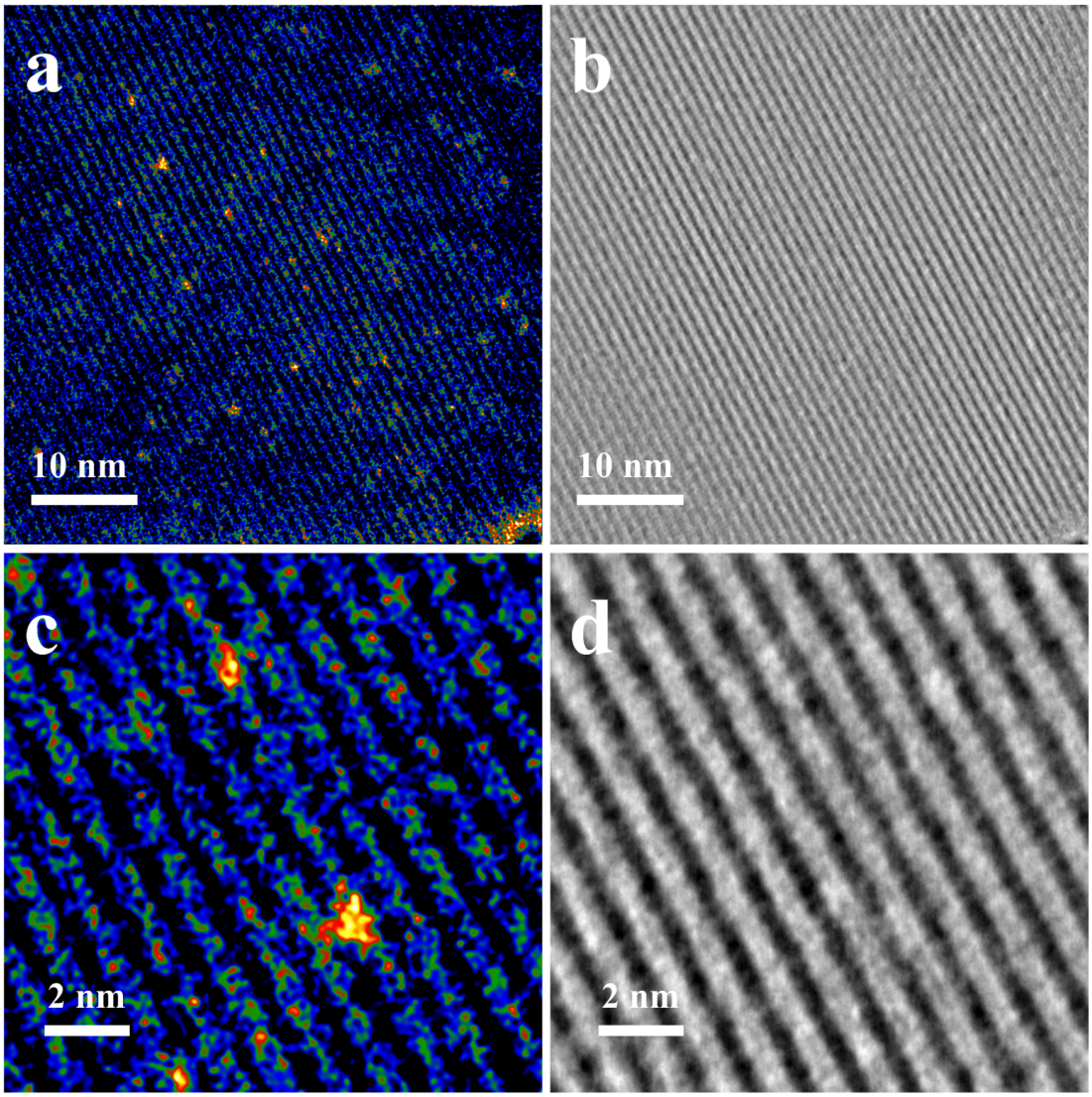


Supplementary Fig. 8. Products distribution illustration. Possible products on 1-hexene hydroformylation reaction (Taken from ref [14]).

2.3. HAADF-STEM and iDPC images of KRh@MFI-Cal catalyst after 1-hexene hydroformylation reaction

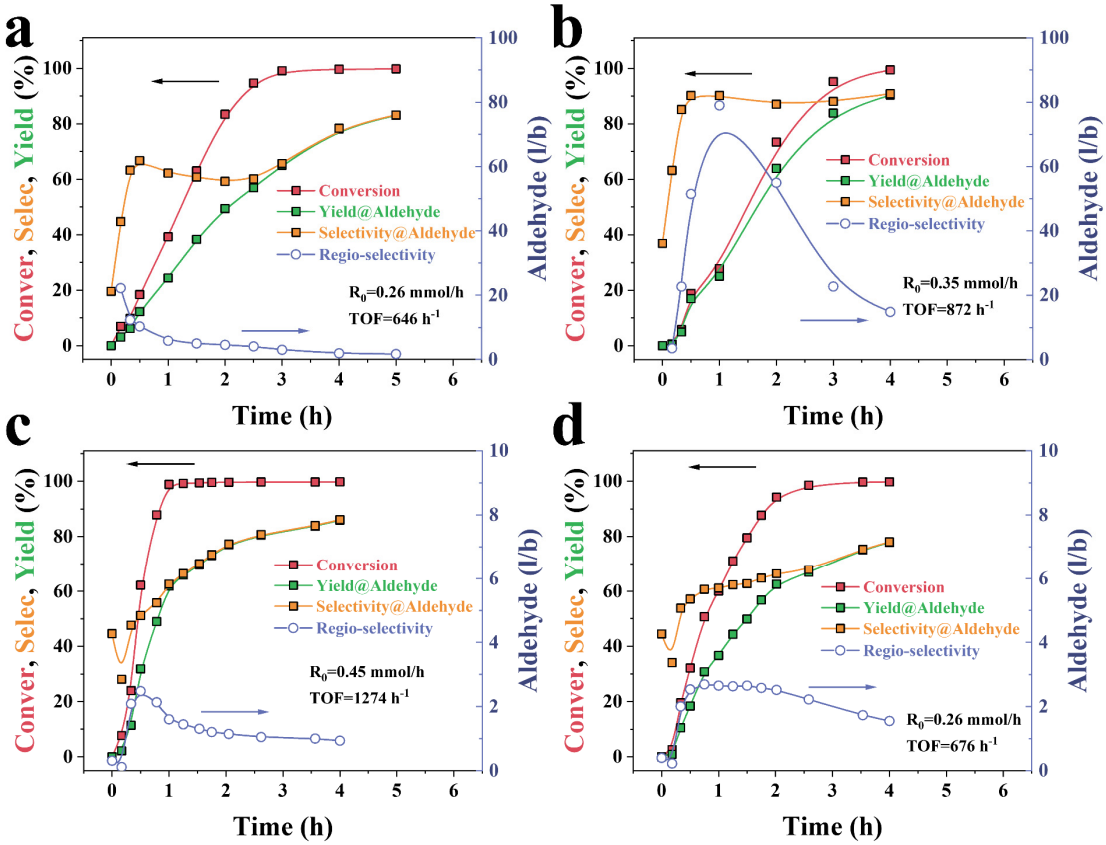


Supplementary Fig. 9. Microscopic results. STEM images of KRh@MFI-Cal after 1-hexene hydroformylation reaction.



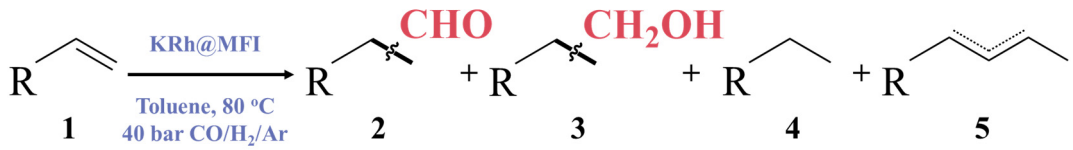
Supplementary Fig. 10. High-resolution high-angle annular dark-field scanning transmission electron microscopy (HR-HAADF-STEM) combined with integrated differential phase contrast (iDPC) imaging of fresh sample. (a, c) HAADF-STEM and (b, d) iDPC images of KRh@MFI-Cal after 1-hexene hydroformylation reaction.

2.4. 1-Hexene hydroformylation (C6 LAO)



Supplementary Fig. 11. 1-hexene hydroformylation activity. (a) K-free Rh@MFI-Cal, (b) KRh@MFI-Cal catalysts, (c) homogeneous Wilkinson's type catalyst $RhHCO(PPh_3)_3$ and (d) in the presence of 500/1 molar ratio of MP/Rh. Reaction condition: 1 mmol LAO, 0.36 mg catalyst (0.00038 mmol Rh), 20 mg decane (internal standard), 4 mL toluene, 40 bar $CO/H_2/Ar$ (45/45/10 vol%), 80 °C, 800 rpm, R_0, TOF and TON are values for linear aldehyde formation.

Supplementary Table 1. 1-hexene hydroformylation activity. Catalytic results for KRh@MFI catalyst of 1-hexene hydroformylation at 80 ºC.[a]



Entry	Catalyst	Conv. (%)	Selec. (%) Aldehyde (L)[b]	l/b[c]	Yield (%)				R_0 (mmol/h)[d] L-Aldehyde	R_0 (mmol/h)[d] Iso-Alkenes	TON[e]	TOF (h^{-1})[f]
					2	3	4	5				
1	Rh@MFI-Cal	99.7	78.4 (51.4)	1.9	78.2	0	0.5	21.0	0.26	0.16	1289	646
2	KRh@MFI-Cal	99.5	90.9 (85.1)	15	90.4	0	1.1	8.0	0.35	0.05	2024	872
3[g]	$RhHCO(PPh_3)_3$	98.8	62.6 (38.5)	1.6	61.9	0	0.3	36.7	0.45	0.54	760	1274
4[h]	$RhHCO(PPh_3)_3$-500MP	94.2	66.4 (47.5)	2.5	62.5	0	0.3	31.4	0.26	0.20	861	676

[a] Reaction conditions: 1 mmol LAO, 20 mg catalyst (0.00038 mmol Rh), 20 mg decane (internal standard), 4 mL toluene, 40 bar $CO/H_2/Ar$ (45/45/10 vol%), 80 ºC, 800 rpm and 4h reaction. For $RhHCO(PPh_3)_3$ catalyst, 0.36 mg catalyst with 0.00038 mmol Rh is used.

[b] Total aldehyde selectivity (L = Linear aldehyde selectivity).

[c] Ratio of the linear aldehyde to the branched aldehyde.

[d] Reaction rate for linear aldehyde formation and reaction rate for isomerized alkenes formation, mmol/h, calculated when LAO conversion is < 20%.

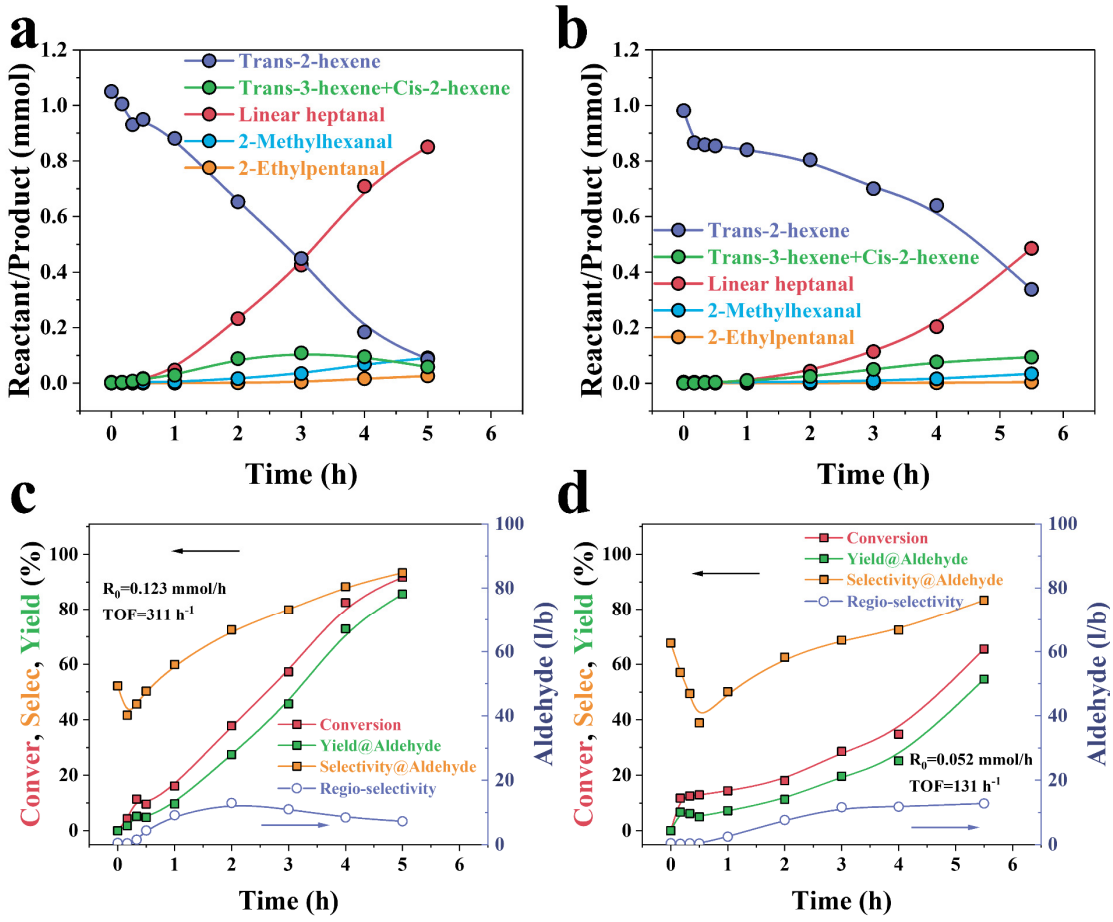
[e] mmol of linear aldehyde/total mmol of Rh at 4h reaction time.

[f] Rate for the formation of linear aldehyde/total mmol of Rh.

[g] 1h reaction.

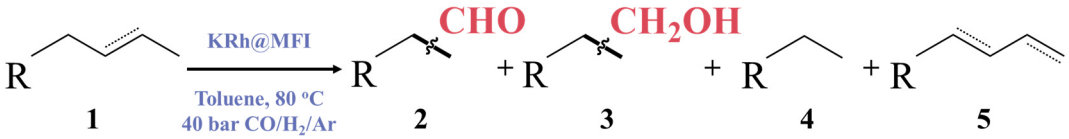
[h] 2h reaction.

2.5. Hydroformylation of trans-2-hexene on KRh@MFI-Cal catalyst



Supplementary Fig. 12. Trans-2-hexene hydroformylation activity of KRh@MFI-Cal catalyst. (a, c) Without and (b, d) with a molar ratio MP/Rh = 500/1 additive. Reaction condition: 1 mmol trans-2-hexene, 20 mg catalyst (0.00038 mmol Rh), 20 mg decane (internal standard), 4 mL toluene, 40 bar $CO/H_2/Ar$ (45/45/10 vol%), 80 ºC, 800 rpm, R_0, TOF and TON are values for linear aldehyde formation.

Supplementary Table 2. Trans-2-hexene hydroformylation activity. Catalytic results for KRh@MFI-Cal catalyst of trans-2-hexene hydroformylation with and without 1-Methylpyrrolidine promoter at 80 ºC.[a]



Entry	Catalysts	Conv. (%)	Selec. (%) Aldehyde (L)[b]	l/b[c]	Yield (%)				R_0 (mmol/h)[d]	TON[e]	TOF (h^{-1})[f]
					2	3	4	5			
1	KRh@MFI-Cal	82.5	88.3 (78.9)	8.4	72.8	0	0.8	8.9	0.12	1797	311
2	KRh@MFI-Cal-500MP	34.8	72.4 (66.7)	11.8	25.2	0	0.6	9.0	0.05	517	131

[a] Reaction conditions: 1 mmol trans-2-hexene, 20 mg catalyst (0.00038 mmol Rh), 20 mg decane (internal standard), 4 mL toluene, 40 bar $CO/H_2/Ar$ (45/45/10 vol%), 80 ºC, 800 rpm and 4h reaction.

[b] Total aldehyde selectivity (L = Linear aldehyde selectivity).

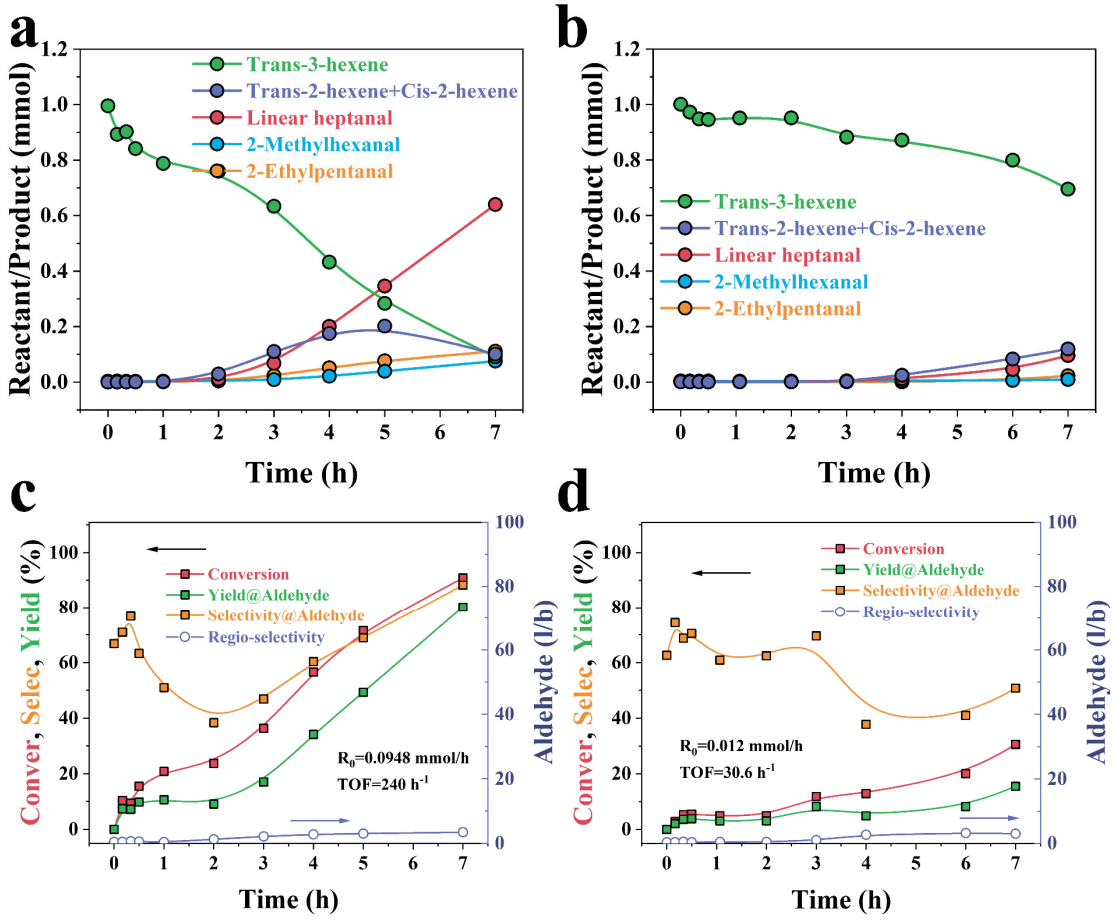
[c] Ratio of the linear aldehyde to the branched aldehyde.

[d] Reaction rate for linear aldehyde formation, mmol/h, calculated when trans-2-hexene conversion is < 20%.

[e] mmol of linear aldehyde/total mmol of Rh at 4h reaction time.

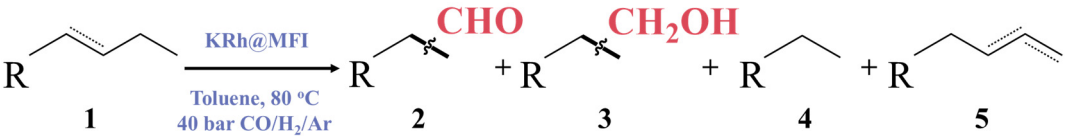
[f] Rate for the formation of linear aldehyde/total mmol of Rh.

2.6. Hydroformylation of trans-3-hexene on KRh@MFI-Cal catalyst



Supplementary Fig. 13. Trans-3-hexene hydroformylation activity of KRh@MFI-Cal catalyst. (a, c) Without and (b, d) with a molar ratio MP/Rh = 500/1 additive. Reaction condition: 1 mmol trans-3-hexene, 20 mg catalyst (0.00038 mmol Rh), 20 mg decane (internal standard), 4 mL toluene, 40 bar $CO/H_2/Ar$ (45/45/10 vol%), 80 ºC, 800 rpm, R_0, TOF and TON are values for linear aldehyde formation.

Supplementary Table 3. Trans-3-hexene hydroformylation activity. Catalytic results for KRh@MFI-Cal catalyst of trans-3-hexene hydroformylation with and without 1-Methylpyrrolidine promoter at 80 ºC.[a]



Entry	Catalysts	Conv. (%)	Selec. (%) Aldehyde (L)[b]	l/b[c]	Yield (%)				R_0 (mmol/h)[d]	TON[e]	TOF (h^{-1})[f]
					2	3	4	5			
1	KRh@MFI-Cal	56.6	60.4 (44.2)	2.7	34.2	0	0.5	21.9	0.09	508	240
2	KRh@MFI-Cal - 500MP	12.9	37.8 (27.6)	2.7	4.9	0	0.8	7.2	0.01	30	30.6

[a] Reaction conditions: 1 mmol trans-3-hexene, 20 mg catalyst (0.00038 mmol Rh), 20 mg decane (internal standard), 4 mL toluene, 40 bar $CO/H_2/Ar$ (45/45/10 vol%), 80 ºC, 800 rpm and 4h reaction.

[b] Total aldehyde selectivity (L = Linear aldehyde selectivity).

[c] Ratio of the linear aldehyde to the branched aldehyde.

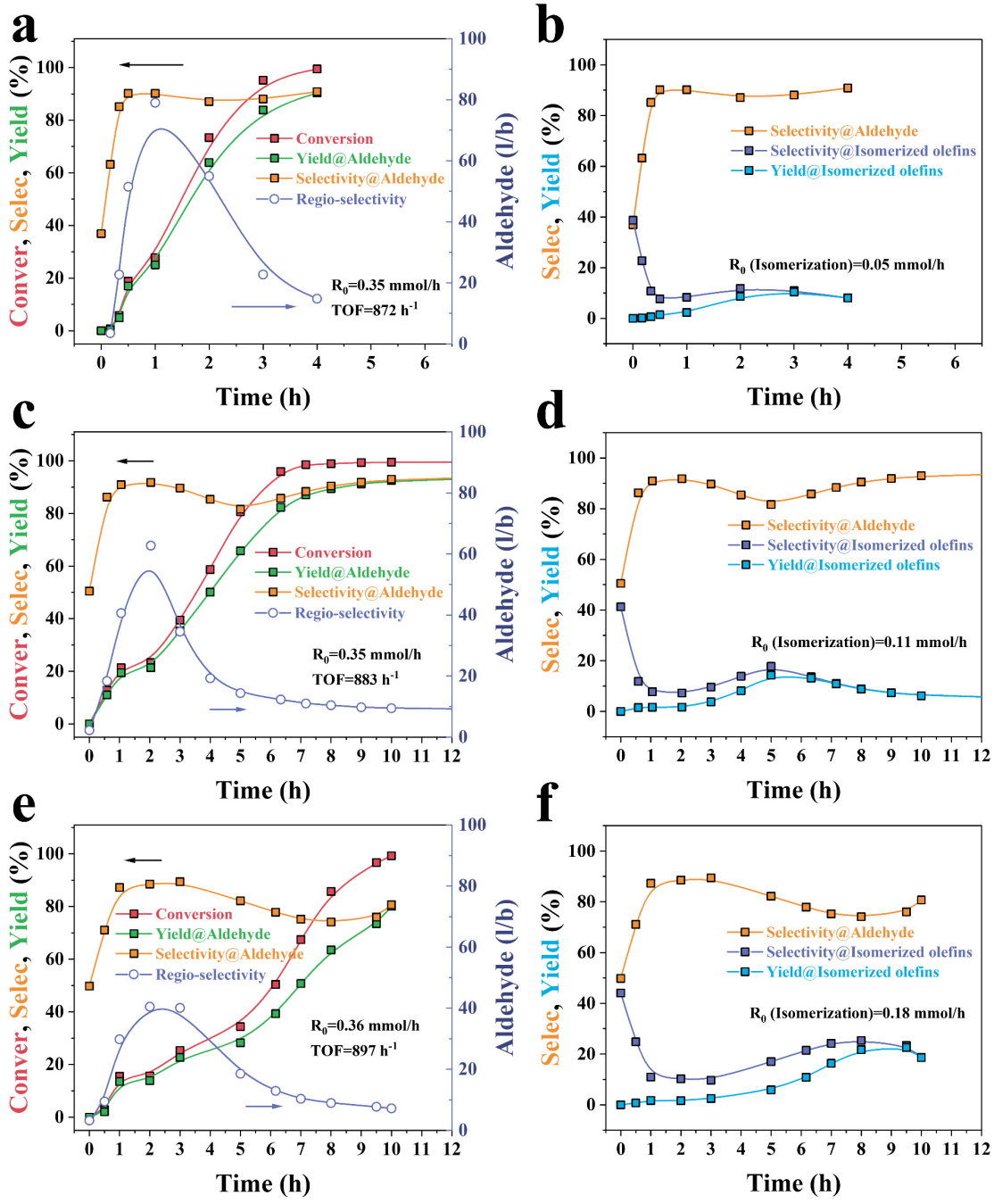
[d] Reaction rate for linear aldehyde formation, mmol/h, calculated when trans-3-hexene conversion is < 20%.

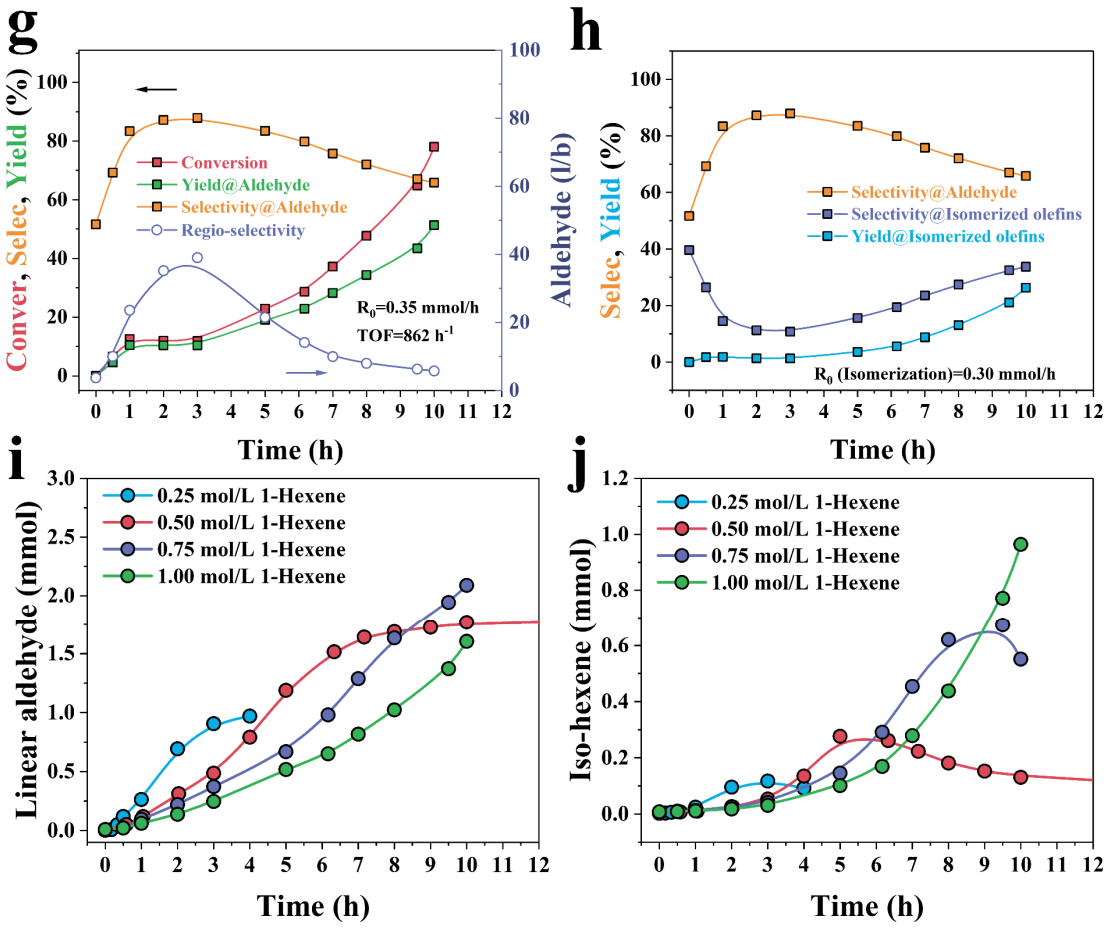
[e] mmol of linear aldehyde/total mmol of Rh at 4h reaction time.

[f] Rate for the formation of linear aldehyde/total mmol of Rh.

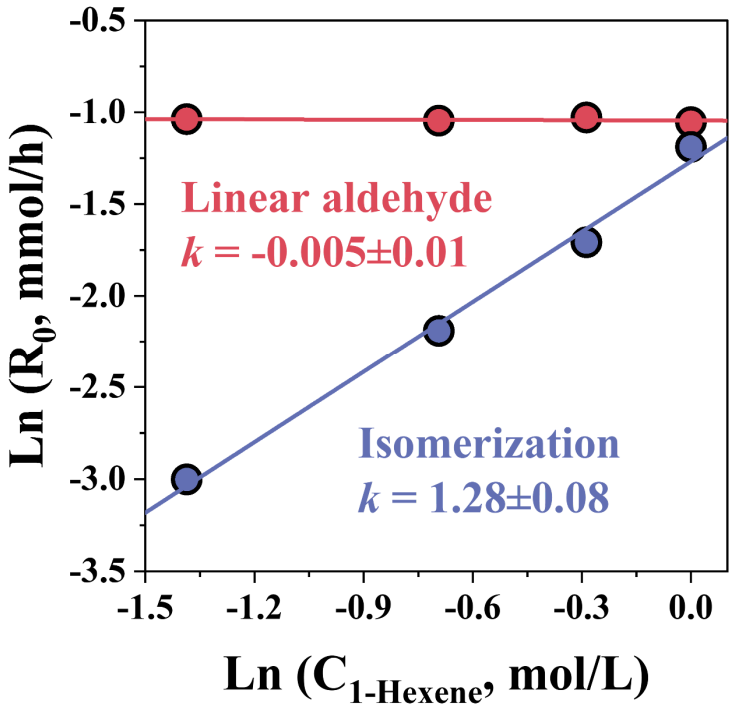
2.7. Reaction order of 1-hexene hydroformylation and isomerization

Varying the concentration of 1-hexene at a fixed Rh loading





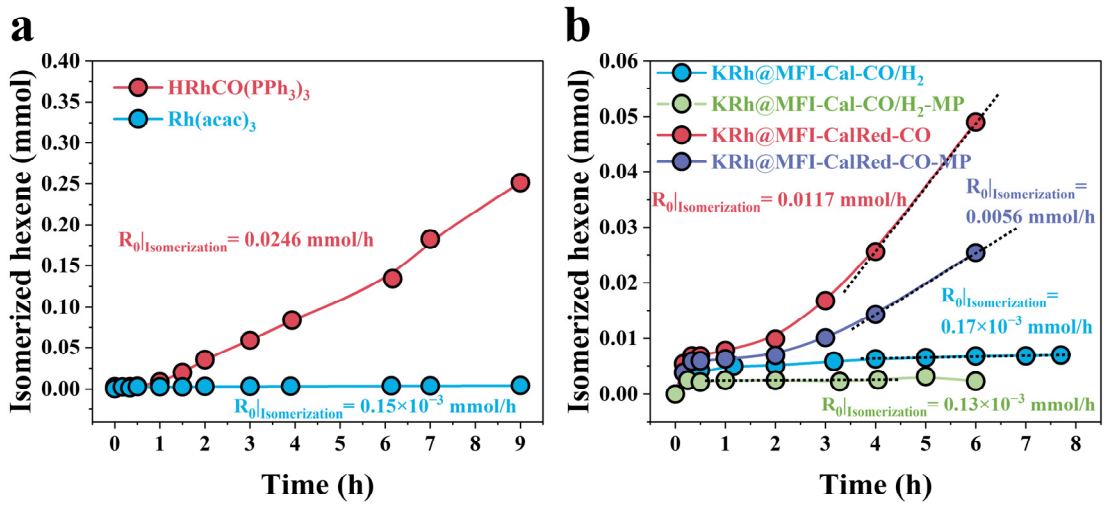
Supplementary Fig. 14. 1-hexene hydroformylation activity under different substrate concentration. Conversion of 1-hexene, aldehyde yield and selectivity, regioselectivity (l/b), isomerized olefins selectivity and yield on KRh@MFI-Cal sample under different 1-hexene concentrations (a, b) 0.25 mol/L, (c, d) 0.5 mol/L, (e, f) 0.75 mol/L, (g, h) 1.0 mol/L and (i, j) time profiles of linear aldehyde and isomerized olefins concentration during reaction. Reaction condition: 1-4 mmol 1-hexene, 20 mg catalyst (0.00038 mmol Rh), 20-80 mg decane (internal standard), all liquid components were dissolved in toluene to a final volume of 4 mL, 40 bar $CO/H_2/Ar$ (45/45/10 vol%), 80 °C, 800 rpm, R_0 and TOF are values for linear aldehyde formation.



Supplementary Fig. 15. Kinetics. Reaction order of 1-hexene hydroformylation and isomerization on KRh@MFI-Cal sample.

Notes: As shown in Supplementary Fig. 14 and 15, increasing the concentration of 1-hexene leads to a more pronounced enhancement in the isomerization reaction than in hydroformylation. For instance, when the 1-hexene concentration exceeds 1 mol/L, the accumulation of isomerized internal olefins results in a substantial decline in both aldehyde selectivity and overall yield. Moreover, the hydroformylation of these internal olefins predominantly generates branched aldehydes, leading to a markedly lower linear-to-branched (l/b) regioselectivity under high 1-hexene concentrations (l/b < 10 at high 1-hexene conversion).

2.8. 1-Hexene isomerization on homogeneous and heterogeneous Rh catalysts

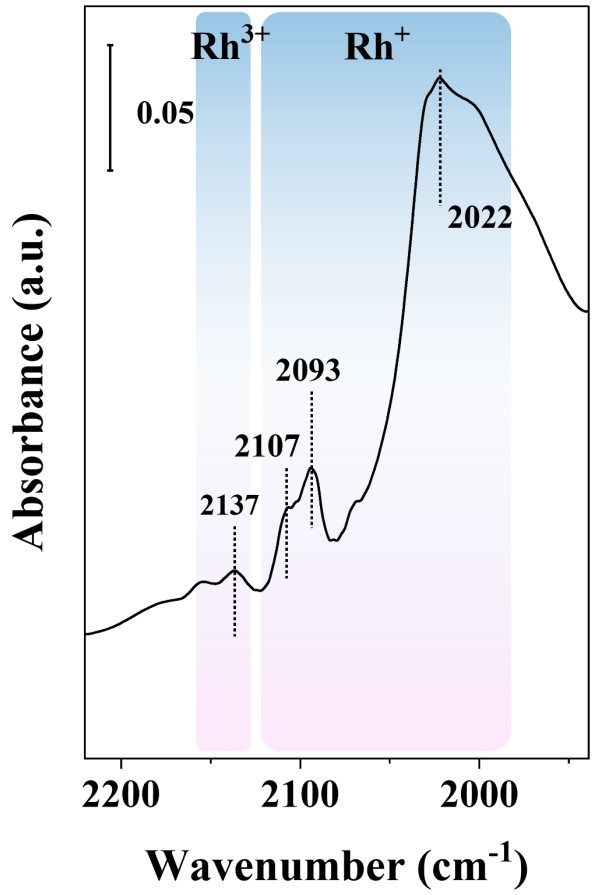


Supplementary Fig. 16. Time profiles of 1-hexene isomerization activity of 1-hexene isomerization activity. (a) Homogeneous $RhHCO(PPh_3)_3$ and $Rh(acac)_3$ catalysts, (b) heterogeneous KRh@MFI-Cal-CO/H_2, KRh@MFI-Cal-CO/H_2-MP, KRh@MFI-CalRed-CO and KRh@MFI-CalRed-CO-MP catalysts at 40 bar N_2. Reaction condition: Isomerization: 1 mmol LAO, 20 mg catalyst (0.00038 mmol Rh), 20 mg decane (internal standard), 4 mL toluene, 40 bar N_2, 80 °C, 800 rpm, molar ratio of MP/Rh = 500/1 if used.

Notes: Isomerization experiments are conducted using homogeneous $RhHCO(PPh_3)_3$, and $Rh(acac)_3$ catalysts, representing Rh^+ and Rh^{3+} oxidation states, respectively. As shown in Supplementary Fig. 16a, $RhHCO(PPh_3)_3$ exhibits significantly higher isomerization activity, whereas $Rh(acac)_3$ showed nearly zero activity for 1-hexene isomerization.

To evaluate the isomerization activity of the heterogeneous KRh@MFI catalysts, a set of parallel experiments was conducted by replacing the standard 40 bar CO/H_2 syngas atmosphere with 40 bar N_2. The catalysts: KRh@MFI-Cal-CO/H_2, KRh@MFI-Cal-CO/H_2-MP, KRh@MFI-CalRed-CO, and KRh@MFI-CalRed-CO-MP were pretreated under controlled conditions to generate primarily Rh^{3+}/Rh^+, pure Rh^+, and Rh^+ sites selectively blocked by MP, respectively. The KRh@MFI-CalRed-CO sample was prepared following the procedure described below for obtaining pure Rh^+. The KRh@MFI-Cal-CO/H_2 sample was prepared starting from KRh@MFI-Cal sample and then pretreated under 40 bar CO/H_2 with toluene solvent at 80 °C for 2h. As shown in Supplementary Fig. 17 and discussed in Appendix 3.3 for the semi-quantitative analysis of IR peak intensities, the KRh@MFI-Cal-CO/H_2 sample shows predominately Rh^{3+} versus Rh^+.

As shown in Supplementary Fig. 16b, the isomerization rate of KRh@MFI-CalRed-CO sample (**Red line**) is approximately two orders of magnitude higher than that of the same catalyst in the presence of MP additive (**Violet-blue line**), and in both cases higher than that of the KRh@MFI-Cal-CO/H_2 sample (**Blue line**), in which Rh^{3+} species are predominant. In this sample the 1-hexene isomerization rate is close to zero (0.17×10^{-3} mmol/h), and further decrease by a factor of ~20% upon addition of the MP additive.

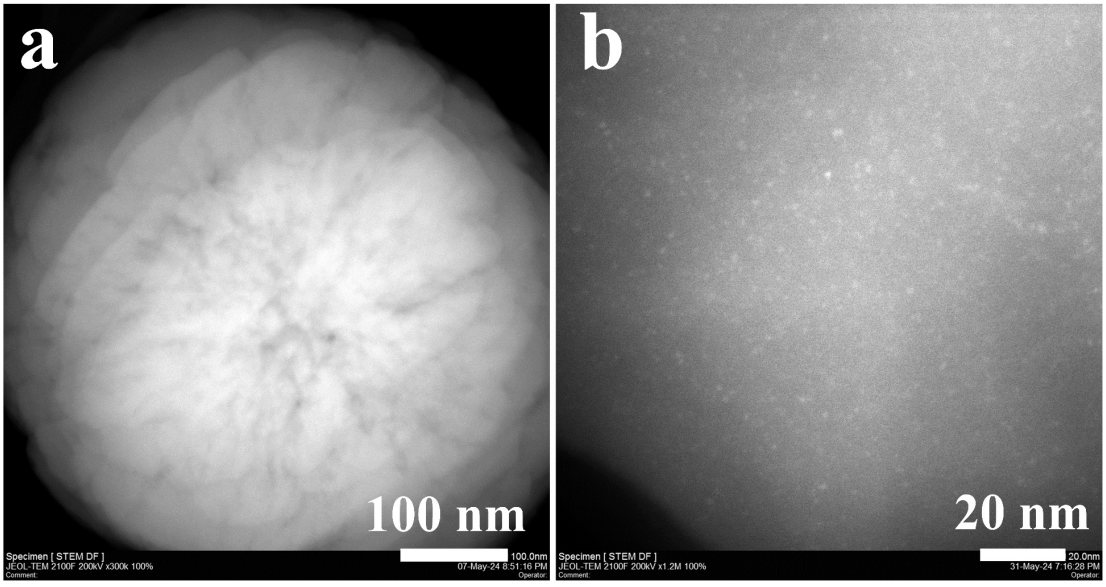


Supplementary Fig. 17. IR-CO results. IR-CO at −65 ºC and 2 mbar CO coverage for KRh@MFI-Cal sample after syngas pretreatment. Pretreatment: 40 mg of KRh@MFI-Cal was stirred in 4 mL toluene under 40 bar CO/H_2/Ar (45/45/10 vol%) at 80 ºC for 2 h.

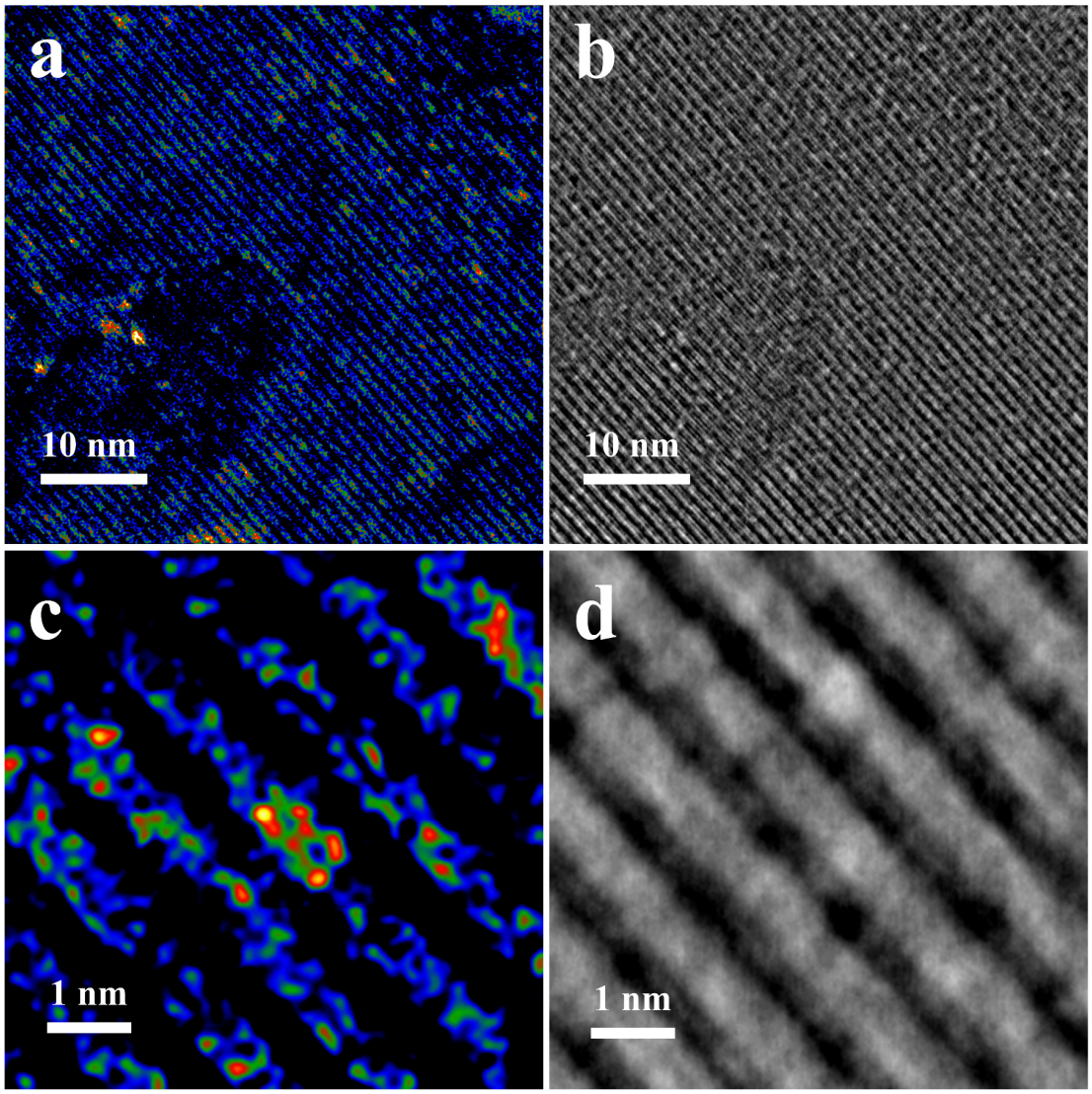
2.9. CO pretreatment on KRh@MFI-Cal catalyst for 1-hexene hydroformylation and isomerization

Pretreatment: Cao and co-workers reported the generation of Rh(I)-gem-dicarbonyl centres inside MEL zeolite channel by H_2 pre-activation and subsequent CO disruption[15]. Herein, KRh@MFI-Cal is firstly *ex-situ* reduced at 600 ºC under pure H_2 for 3h, followed by loading into batch reactor inside glove box. Before reaction, reactor is pressurized to 5 bar H_2 and stirred at 150 ºC for 1h, after which the H_2 is released. Subsequently, the reactor is pressurized 5 bar CO and stirred at 90 ºC for 2h. For comprehensive propose, the CO activated catalyst is labelled herein as KRh@MFI-CalRed-CO. After catalyst pretreatment, reactants are injected inside reactor with 10 mL syringe and the system is pressurized with mixed CO/H_2/Ar (45/45/10 vol%) to 40 bar for reaction.

Catalyst characterizations of XAS and IR-CO of KRh@MFI-CalRed-CO sample are included in the main text of Figure 2i-k.

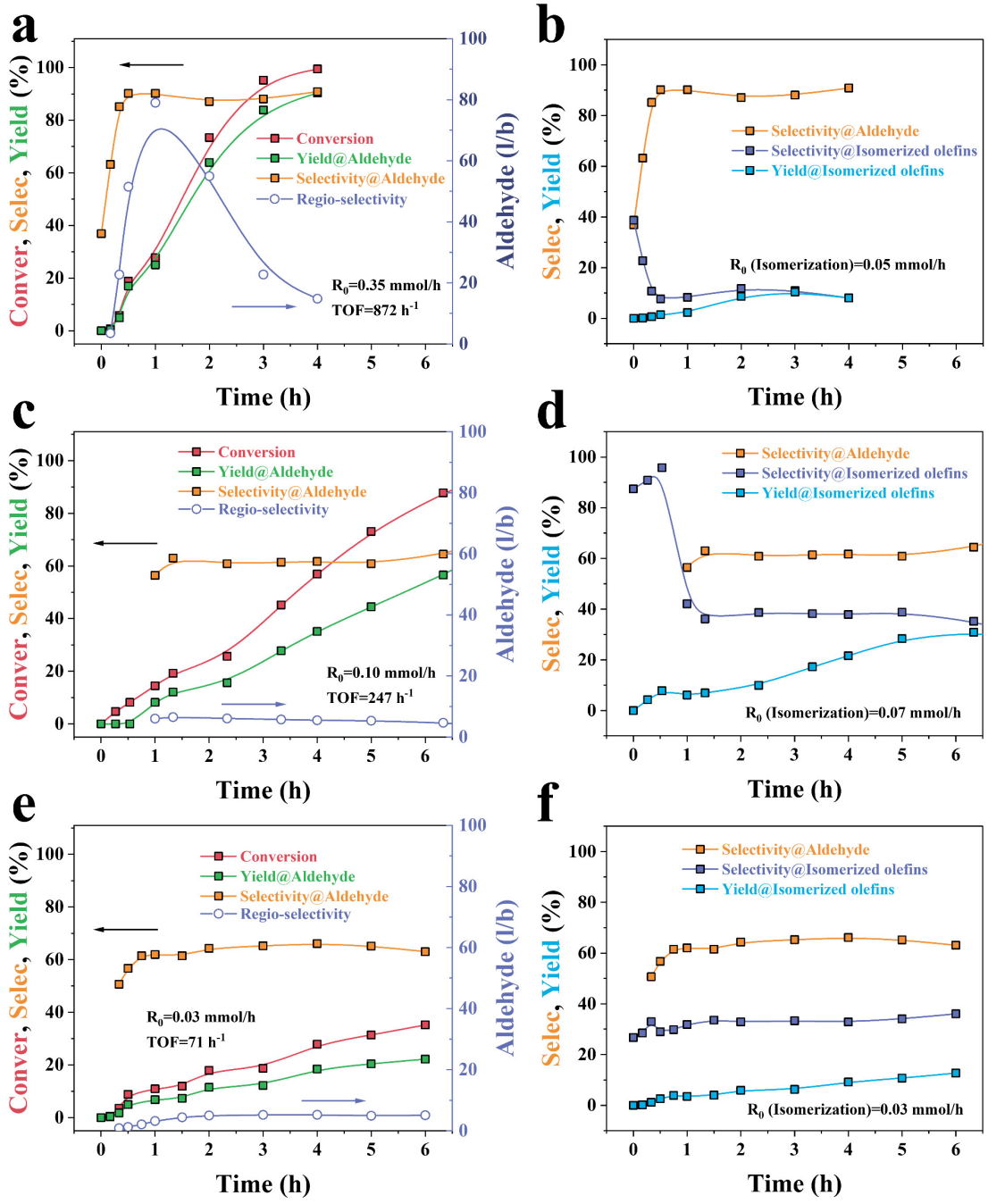


Supplementary Fig. 18. Microscopic results. STEM of KRh@MFI-CalRed-CO.



Supplementary Fig. 19. High-resolution high-angle annular dark-field scanning transmission electron microscopy (HR-HAADF-STEM) combined with integrated differential phase contrast (iDPC) imaging of fresh sample. (a, c) HAADF-STEM and (b, d) iDPC images of KRh@MFI-CalRed-CO.

2.10. 1-Hexene hydroformylation on KRh@MFI-Cal, KRh@MFI-CalRed-CO and KRh@MFI-CalRed-CO-500MP catalysts



Supplementary Fig. 20. 1-hexene hydroformylation activity. (a, b) KRh@MFI-Cal, (c, d) KRh@MFI-CalRed-CO and (e, f) KRh@MFI-CalRed-CO-500MP catalysts (1-Hexene conversion, aldehyde selectivity and yield, regioselectivity (l/b), isomerized hexene selectivity and yield). Reaction condition: 1 mmol LAO, 20 mg catalyst (0.00038 mmol Rh), 20 mg decane (internal standard), 4 mL toluene, 40 bar $CO/H_2/Ar$ (45/45/10 vol%), 80 °C, 800 rpm, R_0, TOF and TON are values for linear aldehyde formation.

Notes: As shown in Supplementary Fig. 20, both the hydroformylation and isomerization activities of 1-hexene over KRh@MFI-CalRed-CO are significantly suppressed in the presence of the organic additive MP (molar ratio MP/Rh = 500). These findings confirm that MP, featuring a nucleophilic -:N-CH_3 functional group, can selectively coordinate to Rh^+ centres, leading to site blockage and consequently a marked decrease in hydroformylation activity.

2.11. Hydroformylation on homogeneous and heterogeneous systems with DFT calculations

In the present work, the Rh^+ system was used as a reference to evaluate the plausibility of a full catalytic cycle occurring on a single Rh^{3+} center. The goal was not to reproduce known Rh^+ chemistry, but to assess whether the key transformations of hydroformylation: migratory insertion, CO insertion, and hydrogenolysis, remain kinetically accessible when the metal is maintained in a higher oxidation state. This approach allows a direct comparison between well-established Rh^+ energetics and hypothetical Rh^{3+} behaviour within a common mechanistic framework.

For the Rh^{3+} system, a hypothetical complex was constructed based on two criteria: (i) maintaining close structural similarity to the Rh^+ analogue by retaining the two phosphine ligands (PH_3), and (ii) mimicking the silanol/siloxy environment of a zeolite by introducing two negatively charged OH^- ligands. The Rh^{3+} mechanism was explored following the same sequence of elementary steps as for Rh^+; however, the oxidative addition and reductive elimination processes were replaced by σ-bond metathesis type step to ensure that the +3 oxidation state of rhodium was preserved throughout the catalytic cycle.

2.11.1 Rh^+ (Reference) Mechanism

The Rh^+ catalytic cycle follows the generally accepted sequence of elementary steps: competitive adsorption of propene (S1-2); migratory insertion to form the propyl intermediate (S2-3); CO adsorption (S3-4); CO insertion yielding the propionyl species (S4-5); oxidative addition of H_2 (S5-6), comprising H_2 coordination (S5-6a) and H-H bond cleavage (S6a-6b); and finally, *n*-butanal formation (S6-7). Labels in the step name refer to the reactant and product intermediate numbering.

The computed free energy profiles for the formation of linear *n*-butanal and branched 2-methylpropanal on Rh^+ are presented in Supplementary Fig. 21 and the reaction and activation free energies are given in Supplementary Table 4. The initial step S1-2, which is common to both pathways, is disfavoured, in terms of free energy, by approximately 46.8 kJ/mol, reflecting the need for propene to displace the more strongly adsorbed CO ligand from the Rh^+ center. In the resulting π-complex (*I2*), the C=C bond of propene adopts an orientation perpendicular to the Rh-H bond

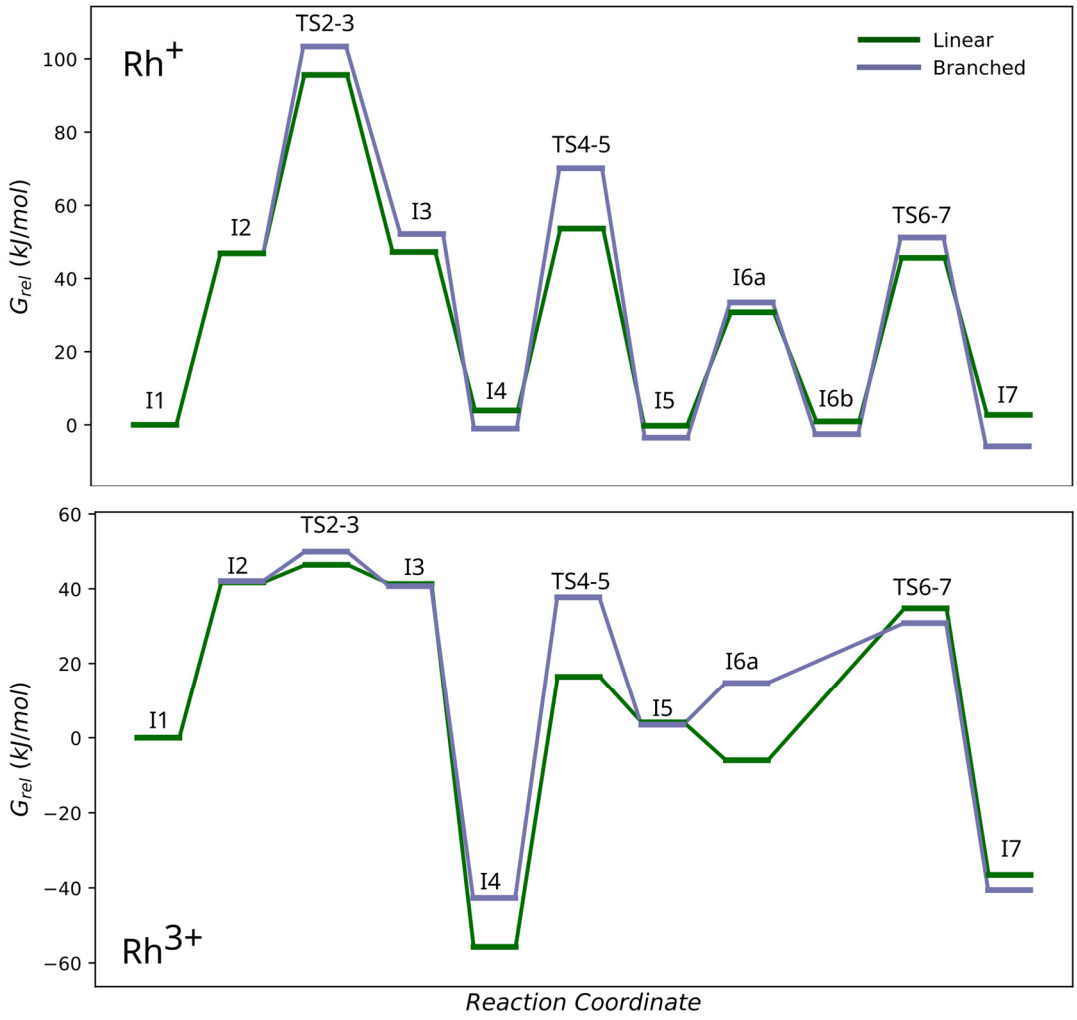
(Supplementary Fig. 22 and 23), enabling hydride transfer to either the C1 or C2 carbon atoms and thus giving rise to the linear (PL) and branched (PB) pathways, respectively. These hydride transfer steps exhibit activation free energies of 48.9 and 56.4 kJ/mol for the PL and PB pathways, respectively, leading to the formation of primary and secondary propyl intermediates (I2).

Following the favourable adsorption of CO ($\Delta G = -43$ kJ/mol), the subsequent CO insertion steps (S4-5) display activation free energy barriers of 49.7 and 71.6 kJ/mol for the PL and PB pathways, respectively, with only slightly positive reaction free energies. The oxidative addition of H_2, leading to the formation of Rh^{3+} species, proceeds without an activation barrier for either pathway, being the H_2 coordination endergonic ($\Delta G > 30$ kJ/mol) and the H_2 splitting exergonic ($\Delta G = -29.7$ and -35.9 kJ/mol for PL and PB, respectively). Finally, product formation (steps S6-7) proceeds with relatively low activation barriers of 44.7 and 53.4 kJ/mol for the PL and PB pathways, respectively.

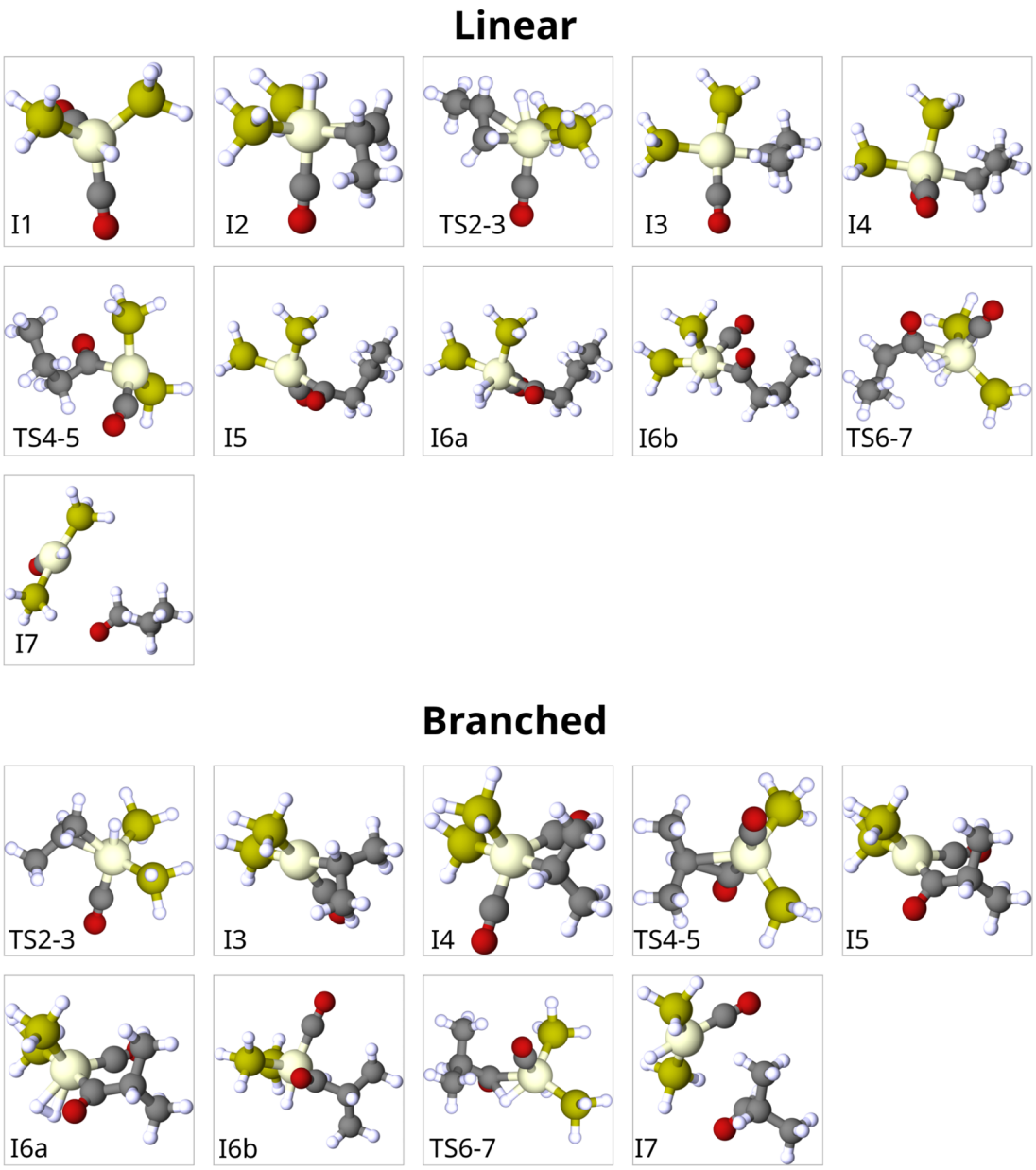
Overall, no highly endergonic steps are observed, confirming the kinetic and thermodynamic feasibility of the Rh^{+}-catalyzed sequence even at low temperatures. The consistently higher barriers along the PB pathway, especially S2-3 and S4-5, reflect the increased steric hindrance at the secondary carbon center and the reduced accessibility of the β-hydride migration transition state. These results are consistent with experimental selectivity trends, where linear aldehydes dominate the product distribution under standard hydroformylation conditions[16]. Taken together, the Rh^{+} mechanism establishes a quantitative benchmark for comparison with alternative catalytic systems.

Supplementary Table 4. DFT calculation results. Calculated free energy (G) and enthalpy (H) changes for reaction (ΔX_{react}) and activation (ΔX_{act}) steps at 300 K, covering all elementary steps of propene hydroformylation with the isolated complex models $RhH(CO)_2(PH_3)_2$ and $RhH(OH)_2(PH_3)_2$. All energies are given in kJ/mol.

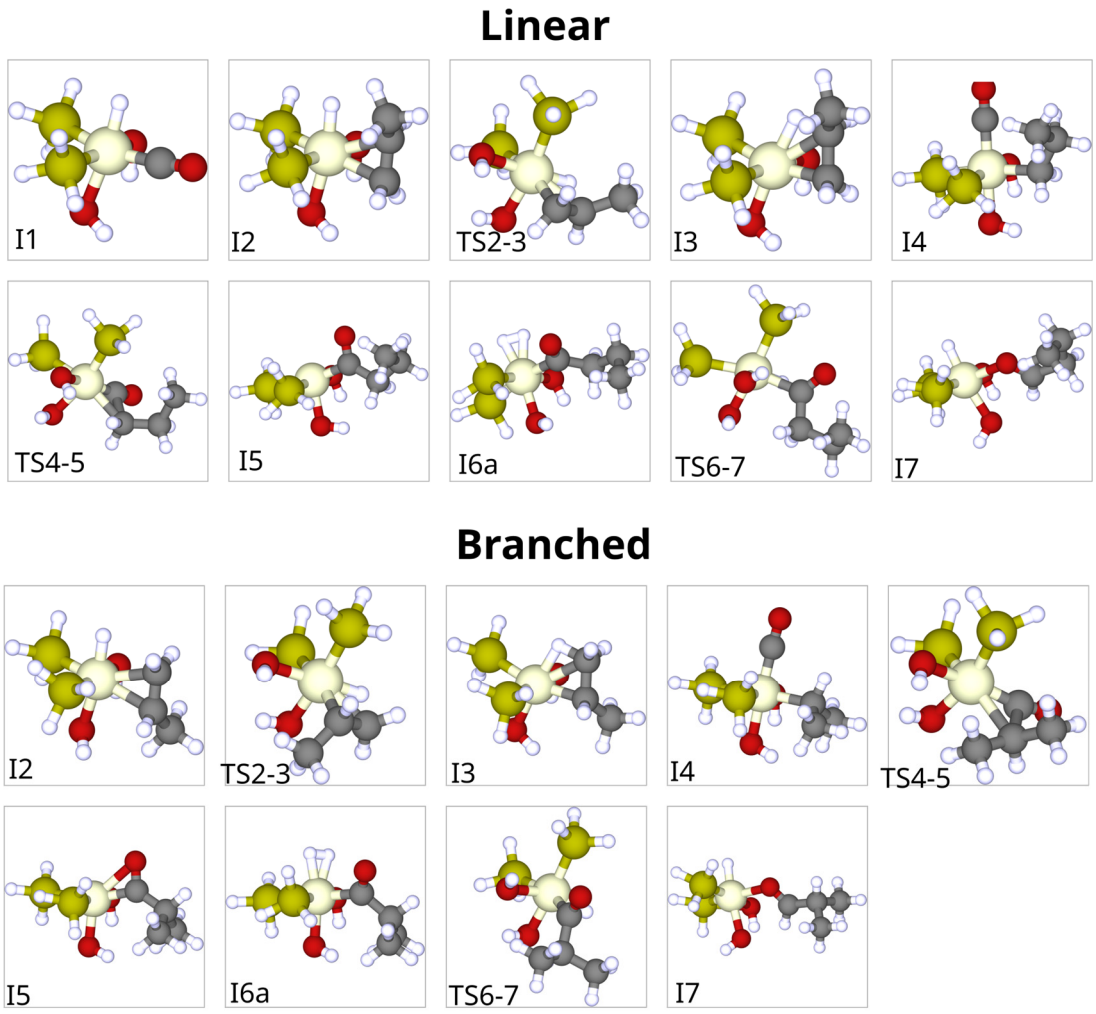
Step	Rh^+				Rh^{3+}			
	ΔG_{act} (ΔH_{act})		ΔG_{react} (ΔH_{react})		ΔG_{act} (ΔH_{act})		ΔG_{react} (ΔH_{react})	
	PL	**PB**	**PL**	**PB**	**PL**	**PB**	**PL**	**PB**
S1-2	-	-	46.8 (37.3)		-	-	41.5 (34.9)	42 (34.2)
S2-3	48.9 (56.2)	56.4 (62.7)	0.4 (5.0)	5.4 (8.8)	4.6 (8.4)	8.0 (13.1)	−0.4 (−1.5)	−1.3 (−0.4)
S3-4	-	-	−43 (−91.6)	−53.1 (−99.6)	-	-	−97.2 (−144)	−83.8 (−131.5)
S4-5	**49.7 (57.5)**	**71.6 (75.4)**	−4.18 (−3.8)	−2.5 (−2.0)	**72.1 (79.3)**	**80.4 (85.8)**	60 (70.8)	46 (54.3)
S5-6a	-	-	31 (−6.8)	36.8 (−1.3)	-	-	−10.1 (−52.4)	11.3 (−28.2)
S6a-6b	-	-	−29.7 (−31.5)	−35.9 (−38.0)	-	-	-	-
S6-7	44.7 (52.7)	53.4 (58.8)	1.7 (18.4)	−3.3 (10.8)	40.6 (42.5)	15.9 (17.2)	−30.6 (−31.1)	−55.2 (−53.8)



Supplementary Fig. 21. Energy profiles. Calculated free energy profiles of hydroformylation of propene on Rh^{+} (upper panel) and Rh^{3+} (lower panel) leading to the formation of *n*-butanal (green) and methylpropanal (violet) aldehydes. Free energy was calculated at 300 K.



Supplementary Fig. 22. Model structure. Optimized structures of minima involved in homogeneous hydroformylation on Rh^{+}.



Supplementary Fig. 23. Model structure. Optimized structures of minima involved in homogeneous hydroformylation on Rh^{3+}.

2.11.2 Rh^{3+} Mechanism on a hypothetical complex

The Rh^{3+}-catalyzed mechanism also begins with the competitive adsorption of propene. In this case, two distinct adsorption geometries are identified: parallel and antiparallel relative to the Rh-H bond, with comparable free energy penalties of 41.5 and 42 kJ/mol, respectively. Although both configurations are energetically similar, the parallel orientation favours the formation of branched aldehydes, whereas the antiparallel arrangement leads to linear aldehydes following hydride insertion. The presence of two well-defined adsorption modes arises from the increased steric constraints imposed by the octahedral coordination environment, which prevents the alkyl substituent from overlapping with the PH_3 and OH ligands in the equatorial plane. Despite a low rotation barrier of approximately 21 kJ/mol between these two orientations, the restricted flexibility

of the octahedral Rh^{3+} center could, in principle, offer greater control over regioselectivity compared to Rh^{+} systems, owing to the more rigid coordination geometry.

Formation of the alkyl intermediates (S2-3) is highly facile, with free energy barriers of only ~5-8 kJ/mol for both PL and PB. As in the Rh^{+} system, CO adsorption significantly stabilizes the complex, but in this case with a stronger adsorption free energy of > −80 kJ/mol. The subsequent CO insertion (S4-5) represents the rate-determining step, with barriers of 72.1 and 80.4 kJ/mol for PL and PB, respectively, and the resulting acyl intermediates (I5) are relatively unstable (ΔG = +70 kJ/mol). I5 is slightly stabilized upon H_2 coordination (S5a) in the PL pathway, (−10 kJ/mol), whereas no such stabilization is observed for PB. Nevertheless, this step is more favourable than in the Rh^{+} system, where H_2 adsorption is endergonic. Finally, product formation, yielding *n*-butanal (PL) and 2-methylpropanal (PB), occurs via a σ-bond metathesis-type step with low activation barriers of 41 and 16 kJ/mol, confirming that the hydroformylation cycle is kinetically accessible even at low temperatures, while maintaining the +3 oxidation state of rhodium throughout.

In terms of selectivity, the rate-determining CO insertion step (S4-5) in the PB pathway is higher in energy by ~ 4 kJ/mol, and the corresponding intermediates are systematically less stable, reflecting the greater steric effect associated with branched intermediates. These trends closely parallel those observed for the Rh^{+} system, suggesting that Rh^{3+} is expected to exhibit similar regioselectivity, favouring formation of the linear (PL) aldehyde product.

2.11.3 Comparative Mechanistic Analysis

Mechanistically, both Rh^{+} and Rh^{3+} pathways are similar, but their electronic profiles differ markedly. In Rh^{+} catalysis, the metal alternates between $16e^{-}$ and $18e^{-}$ configurations through two-electron oxidative addition and reductive elimination steps, stabilizing the hydride and acyl intermediates. In contrast, Rh^{3+} species are formally d^6 and may proceed through associative or σ-bond metathesis-type mechanisms, rather than formal redox processes. Nonetheless, the resulting transition states exhibit comparable overall energetics. The comparative analysis thus establishes Rh^{+} as a quantitative and mechanistic reference, against which Rh^{3+} shows comparable energy barriers and favourable thermodynamics. While Rh^{+} remains the experimentally verified active

species in hydroformylation, these results indicate that Rh^{3+} complexes can be, in principle, catalytically active showing similar selectivity as the Rh^{+} complexes. Overall, the data support the view that Rh^{3+}-mediated hydroformylation is energetically plausible, expanding the conceptual space for designing rhodium catalysts.

2.11.4 Mechanism on MFI

Having established that the mechanism is kinetically feasible for Rh^{3+}, we extended our study to the hydroformylation reaction on an MFI periodic model, to account for the local environment of Rh^{+}/Rh^{3+} cations within a zeolite framework.

The active sites are modelled as Z-Rh^{+}-H^{-} and Z-Rh^{3+}-H^{-} species, i.e., a zeolite-bound Rh^{+} and Rh^{3+} center charge-compensated by one hydride ligand and (for Rh^{3+}) two negatively charged siloxy groups (Supplementary Fig. 26). Up to acyl formation, the reaction mechanisms are, involving competitive propene adsorption, hydride-driven propyl formation, CO coordination, and CO insertion. However, subsequent steps differ from the classical oxidative addition-reductive elimination sequence characteristic of Rh^{+}. Instead, for Rh^{3+} the mechanism proceeds via H_2 coordination followed by aldehyde formation through a σ-bond metathesis-type step, such that the formal oxidation state of rhodium remains +3 throughout the catalytic cycle. Desorption of the products regenerates the initial Z-Rh^{+}-H^{-} and Z-Rh^{3+}-H^{-} active sites. Pathways leading to linear and branched aldehydes are denoted PL and PB, respectively, and the corresponding activation free energies are summarised in Supplementary Table 5.

The computed free energy profile for the Z-Rh^{+}-H^{-} system is presented in Supplementary Fig. 24. The initial intermediate corresponds to a square-planar $Rh^{+}H^{-}(CO)_3$ complex, which is essentially detached from the zeolite framework because the adsorption of three CO molecules onto the pre-stabilized Z-Rh^{+}-H^{-} species in the silanol nest is highly exothermic, with a stabilization energy of approximately −553 kJ/mol. This large value highlights the much stronger interaction of CO with the Rh^{+} center compared to the silanol groups, suggesting that the catalytic behaviour should resemble that of the homogeneous system in terms of ligand effects but the geometric confinement at the zeolite channel intersections may restrict molecular rotation and thereby enhance

regioselectivity. The weak interaction between the Rh^{+} complex and the framework suggests limited structural stability, especially during the hydroformylation of olefins.

In the $Rh^{+}H^{-}(CO)_3$ mechanism, the formation of propyl intermediate (I3) has low activation barriers, approximately 2.9 and 2.6 kJ/mol for the PL and PB pathways, with exergonic reaction free energies −27.8 and −8.2 kJ/mol respectively. Subsequent CO adsorption further stabilizes the complex by −5.2 and −64.6 kJ/mol. Intermediate I4, in contrast to the homogenous mechanism (trigonal-bipyramidal), is square planar reflecting the stabilizing effect of the zeolite framework (Supplementary Fig. 25 and 26). As in the homogeneous case, CO insertion (S4-5) constitutes the rate-determining step, with an associated barrier of 58.8 and 50.1 kJ/mol for PL and PB respectively. The oxidative addition of H_2 is a spontaneous one-step process, being exothermic in both pathways, PL and PB, leading to the formation of a square pyramidal Rh^{3+} hydride complex. Finally, *n*-butanal formation occurs via surmounting a low barrier of 23.6 kJ/mol, regenerating the initial square-planar $Rh^{+}H^{-}(CO)_3$ species and closing the catalytic cycle.

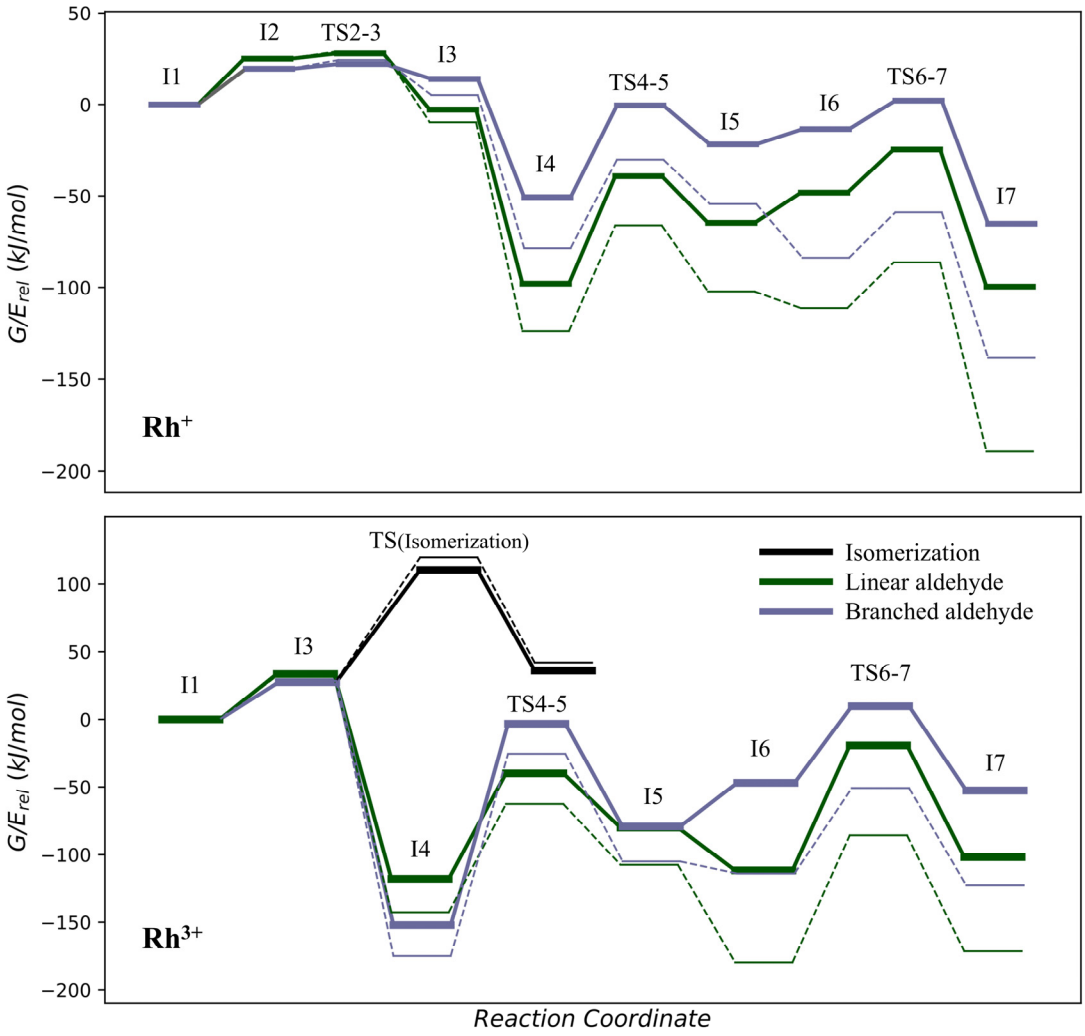
The computed free energy profile for the hydroformylation on Z-Rh^{3+}-H^{-} site (Supplementary Fig. 24) reveals a multistep sequence in which the key elementary steps differ between the two pathways, PL and PB. The adsorption of propene (S1-2) is similarly endergonic for both routes (33.5 and 27.5 kJ/mol). Subsequent propyl formation and CO coordination steps (S2-3 and S3-4) are spontaneous and significantly exothermic, −151.3 and −179.6 kJ/mol for PL and PB respectively, driving the system downhill toward I4. From this point, the two pathways differ: for PL, the next transformation (S4-5) occurs with a barrier of 77.9 kJ/mol and a reaction energy of 37.8 kJ/mol while for PB the corresponding step is kinetically and thermodynamically more disfavoured (ΔG_{act} = 148.8, ΔG_{reac} = 72.8 kJ/mol). This step is the rate-determining step for PB and thus constitutes a key selectivity-determining point, where the linear route (PL) becomes strongly preferred. Subsequent adsorption of H_2 (S5-6) is exergonic for PL (−31.6 kJ/mol) but endergonic for PB (32.3 kJ/mol). The final formation of butanal proceeds with barriers of 92 and 56 kJ/mol for PL and PB, respectively.

Isomerization reactions are in general less favoured than hydroformylation since the transfer of C3-H atom to Rh^{3+} cation from secondary propyl intermediates compete with the exothermic adsorption of CO. In Rh^{3+} sites this adsorption is even more exothermic and thus isomerization is more strongly hindered at this active site. Furthermore, an additional key distinction between the Rh^{3+} centers

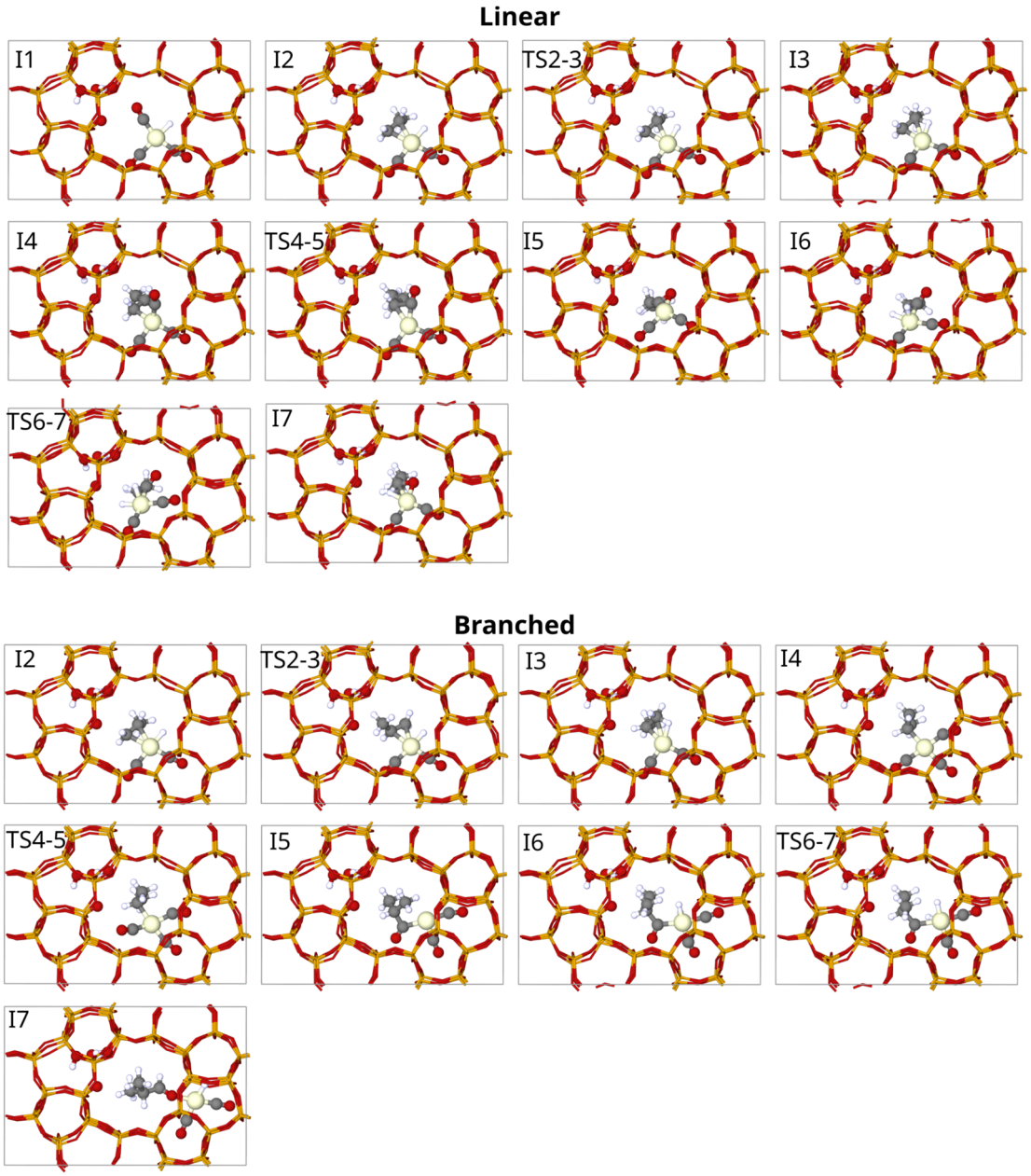
stabilized within the zeolite framework and either the homogeneous Rh^{3+} species or the Rh^{+}-MFI model (which resembles the homogeneous complex in its ligand environment) is the rigidity of the coordination sphere. In the Rh^{3+}-MFI system, the ligands (siloxys and silanol groups) are spatially constrained. As a result, the H-C3 bond cleavage required for double-bond migration from C1 = C2 to C2 = C3 would necessitate a major ligand rearrangement, feasible for Rh^{+} but not for Rh^{3+}. This geometric rigidity is thus reflected in the relatively high activation barrier calculated for alkene isomerization, 91.2 kJ/mol, implying that conversion to internal (2-) alkenes is expected to be significantly slow.

Supplementary Table 5. DFT calculation results. Calculated free energy (G) and enthalpy (H) changes for reaction (ΔX_{react}) and activation (ΔX_{act}) steps at 350 K, covering all elementary steps of propene hydroformylation within the periodic MFI model. All energies are given in kJ/mol.

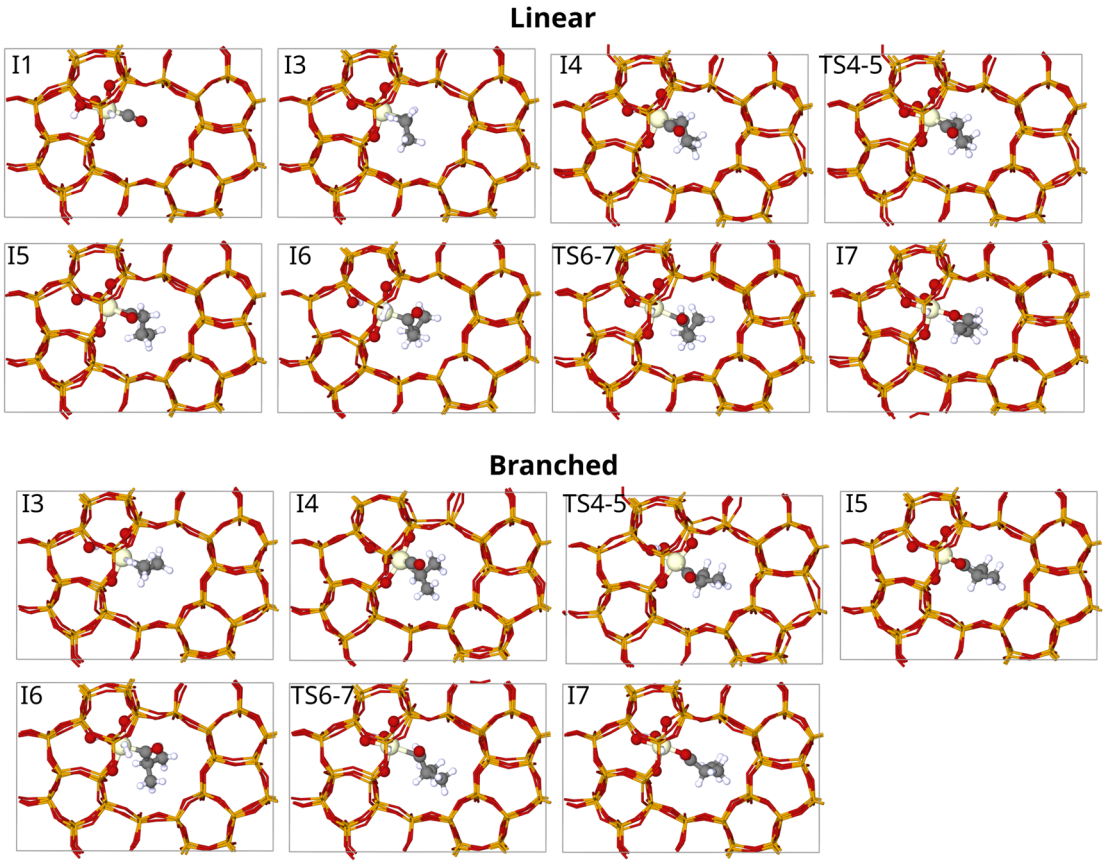
Step	**Rh^{+}**				**Rh^{3+}**			
	ΔG_{act} (ΔH_{act})		**ΔG_{react} (ΔH_{react})**		**ΔG_{act} (ΔH_{act})**		**ΔG_{react} (ΔH_{react})**	
	PL	**PB**	**PL**	**PB**	**PL**	**PB**	**PL**	**PB**
S1-2	-	-	25 (25.4)	19.5 (20.3)	-	-	33.5 (34.3)	27.5 (30.7)
S2-3	2.9 (3.7)	2.6 (1.1)	−27.8 (−29.3)	−8.2 (−11.1)	-	-	-	-
S3-4	-	-	−95.2 (−111.5)	−64.6 (−80.9)	-	-	−151.3 (−169.0)	−179.6 (−199.0)
S4-5	**58.8 (55.2)**	**50.1 (46.0)**	**33.3 (26.3)**	**28.9 (25.0)**	**77.9 (75.2)**	**148.8 (145.7)**	**37.8 (36.8)**	**72.8 (71.0)**
S5-6	-	-	16.5 (−11.6)	8.3 (−26.7)	-	-	−31.6 (−67.2)	32.3 (−2.1)
S6-7	23.6 (19.9)	15.6 (19.1)	−51.4 (−62.5)	−51.7 (−46.7)	92.3 (91.6)	56.6 (59.8)	9.8 (12.3)	−5.6 (−4.3)



Supplementary Fig. 24. Energy profiles. Free energy (solid line) and energy (dashed line) profiles of hydroformylation on Rh^{+} (upper panel) leading to the formation of *n*-butanal (green) and methylpropanal (violet), and on Rh^{3+} (lower panel) for *n*-butanal (green) and methylpropanal (violet) and isomerized alkene (black), within the periodic MFI model.

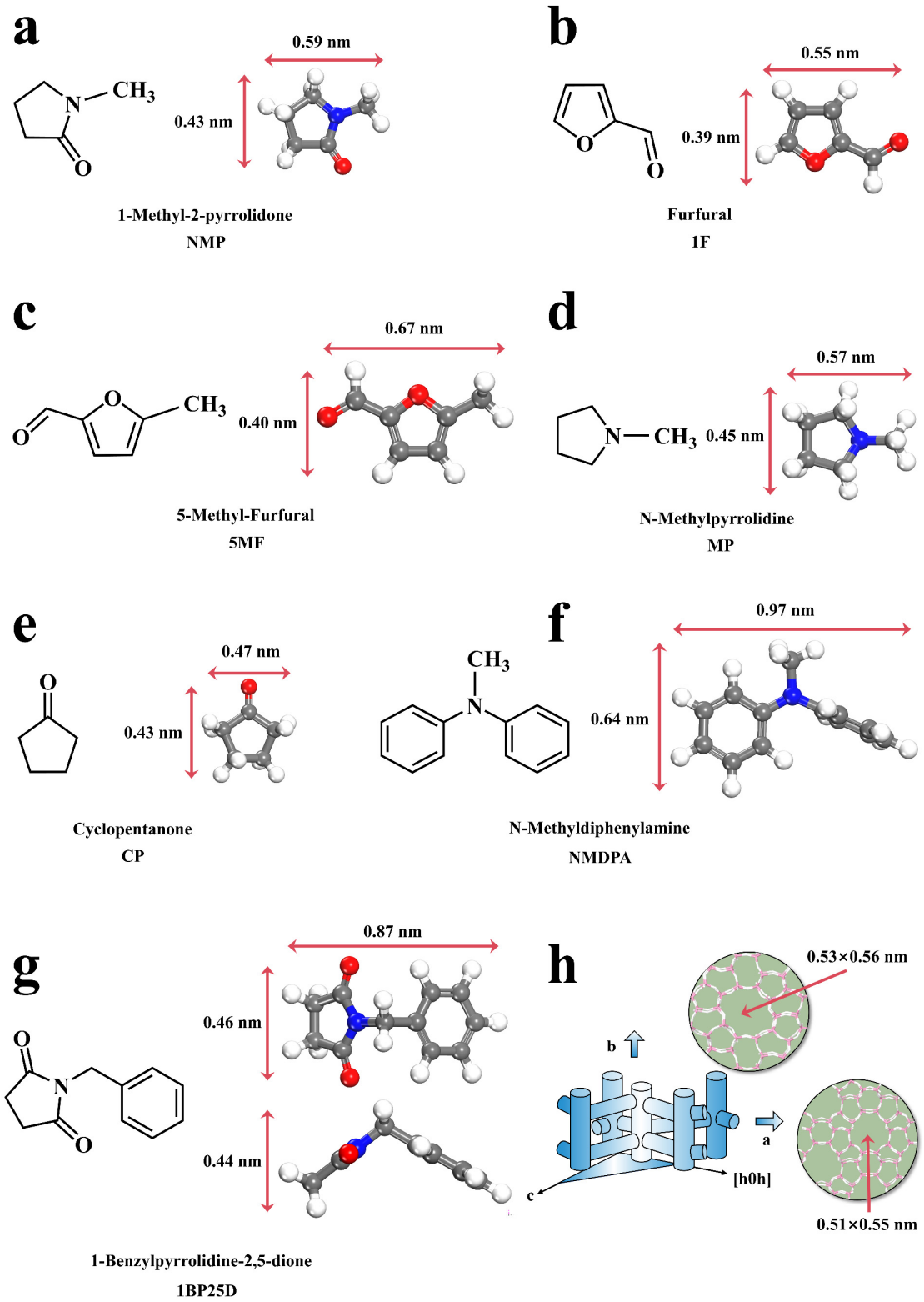


Supplementary Fig. 25. Model structure. Optimized structures of minima involved in hydroformylation on Rh^+ within the periodic MFI model.

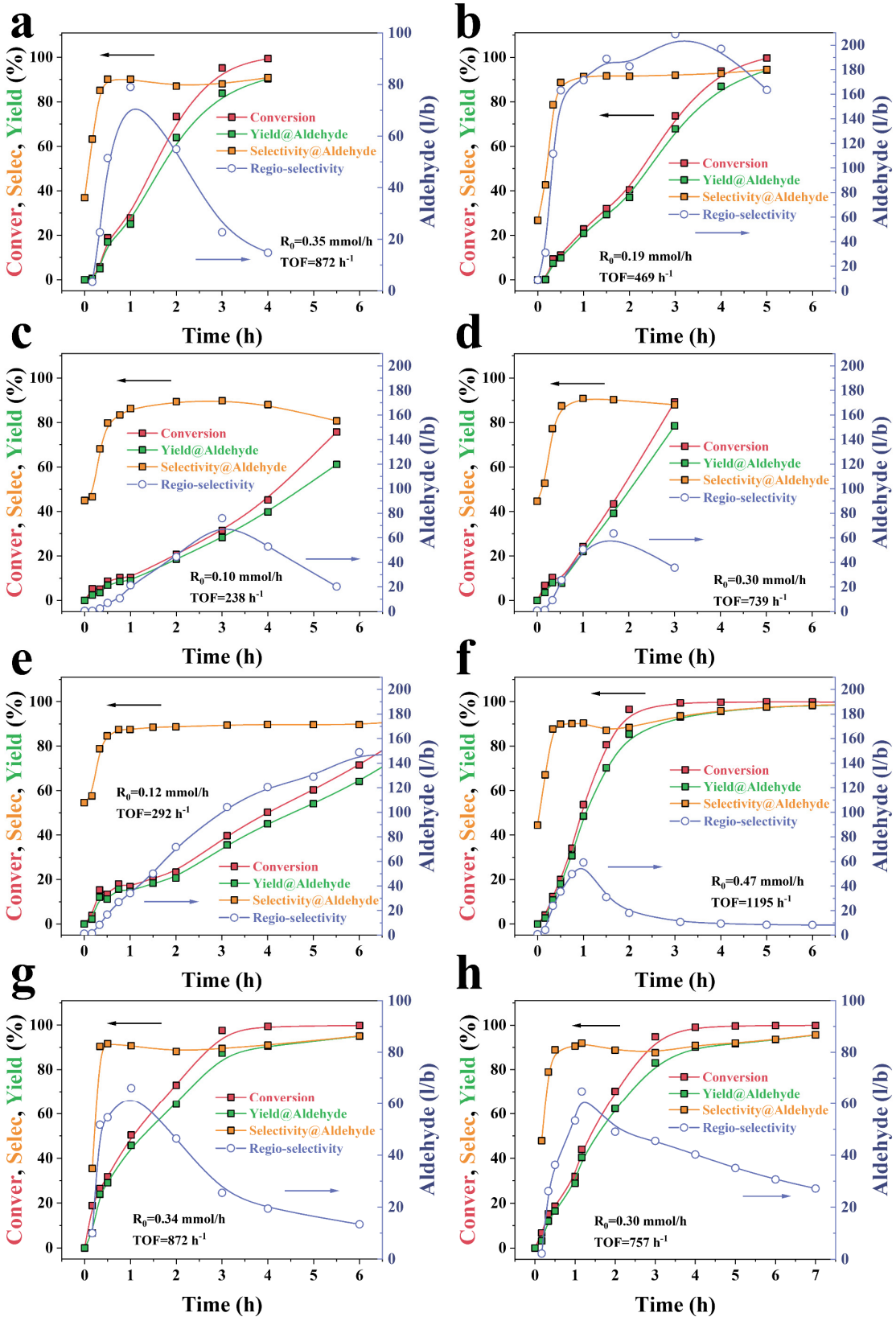


Supplementary Fig. 26. Model structure. Optimized structures of minima involved in hydroformylation on Rh^{3+} within the periodic MFI model.

2.12. 1-Hexene hydroformylation in the presence of organic molecules



Supplementary Fig. 27. Organic additives molecules and kinetic diameter. (a) 1-Methyl-2-Pyrrolidone (NMP), (b) Furfural, (c) 5-Methyl-Furfural, (d) N-Methylpyrrolidine (MP), (e) Cyclopentanone, (f) N-Methyldiphenylamine, (g) 1-Benzylpyrrolidine-2,5-dione and (h) MFI zeolite structure and corresponding kinetic dimensions.



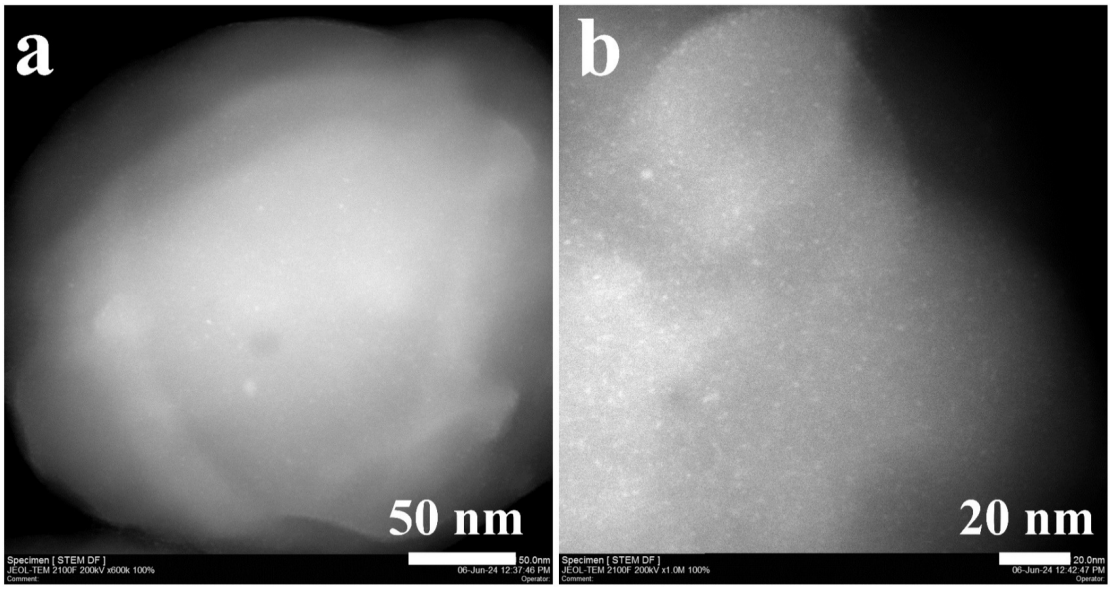
Supplementary Fig. 28. 1-hexene hydroformylation activity of KRh@MFI-Cal catalyst. (a) Without and with (b) 1-Methyl-2-Pyrrolidone (NMP), (c) Furfural, (d) 5-Methyl-Furfural, (e) N-Methylpyrrolidine (MP), (f) Cyclopentanone (g) N-Methyldiphenylamine and (h) 1-Benzylpyrrolidine-2,5-dione organic ligand additives (Molar ratio of organic ligand/Rh = 4000).

Reaction condition: 1 mmol LAO, 20 mg catalyst (0.00038 mmol Rh), 20 mg decane (internal standard), 4 mL toluene, 40 bar $CO/H_2/Ar$ (45/45/10 vol%), 4000/1 molar ratio additive/Rh, 80 ^oC, 800 rpm, R_0, TOF and TON are values for linear aldehyde formation.

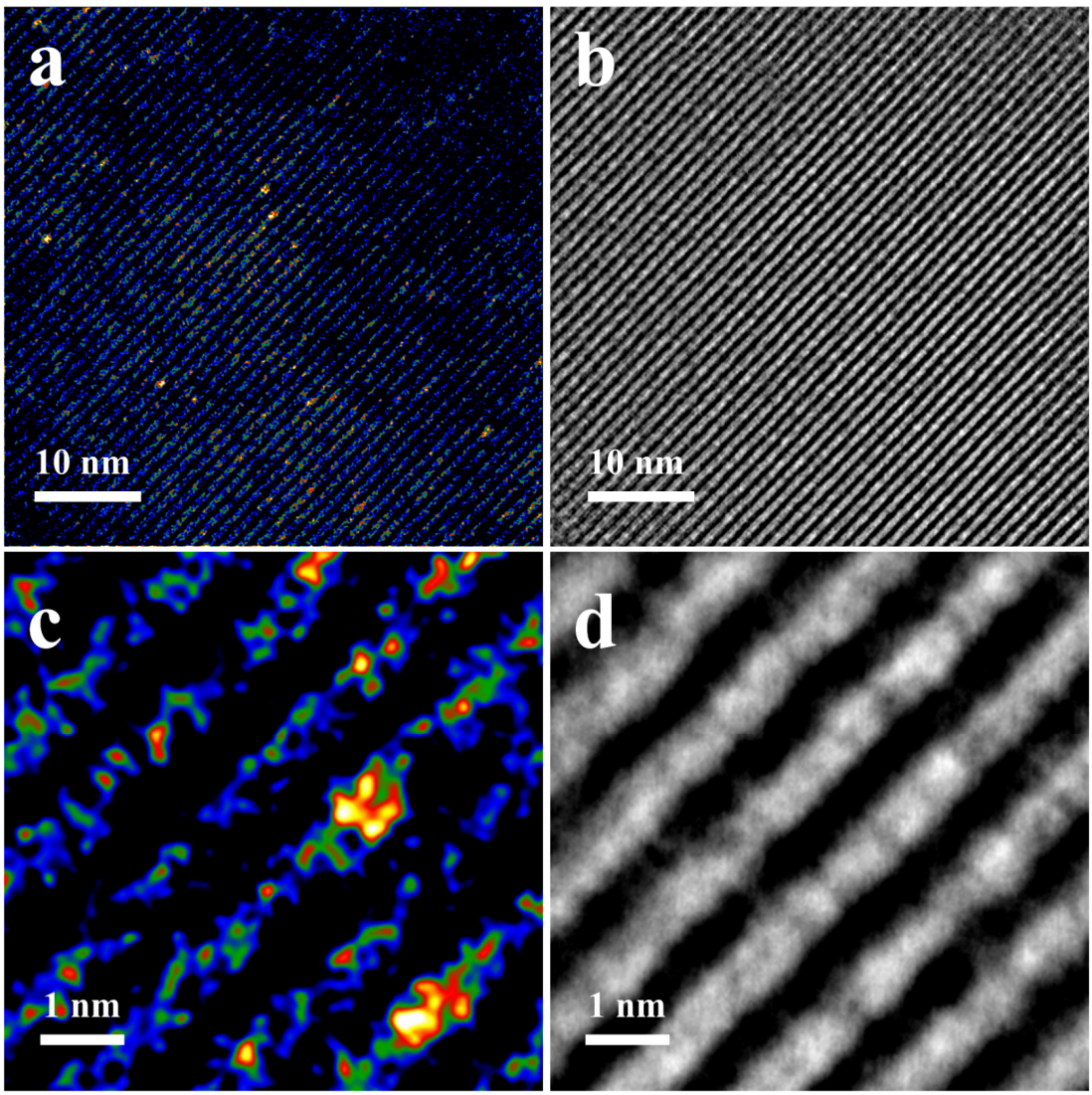
Notes: It is clearly observed NMP and N-methylpyrrolidine have strong influence on the regioselectivity of aldehyde, while furfural, 5-methyl furfural and cyclopentanone with -C=O functional group only influence reaction rates. Thus, it confirmed -:N-CH_3 functional group is key to increase the regioselectivity of aldehyde during hydroformylation. However, N-methyldiphenylamine and 1-benzylpyrrolidine-2,5-dione with same -:N-CH_3 functional group but larger molecular size, fail to improve the regioselectivity of aldehyde. This highlights the importance of molecular diffusion, where only small Lewis base molecules capable of accessing the MFI zeolite channels can effectively modulate the local environment and enhance regioselectivity.

2.13. Spectroscopic characterization of spent samples

HAADF-STEM and iDPC images of KRh@MFI-Cal-500MP catalyst after 1-hexene hydroformylation



Supplementary Fig. 29. Microscopic results. STEM images of KRh@MFI-Cal-500MP after 1-hexene hydroformylation reaction.



Supplementary Fig. 30. High-resolution high-angle annular dark-field scanning transmission electron microscopy (HR-HAADF-STEM) combined with integrated differential phase contrast (iDPC) imaging of fresh sample. (a, c) HAADF-STEM and (b, d) iDPC images of KRh@MFI-Cal-500MP after 1-hexene hydroformylation reaction.

2.14. Stability of Rh active sites and theoretical IR analysis

The experimental infrared spectra of the Rh carbonyl species show characteristic ν(CO) bands that provide direct insight into the electronic properties of the Rh center and the effect of molecular adsorption. For the Rh^{+}-2CO complex, the symmetric and asymmetric stretching modes appear at 2092 and 2065 cm^{-1}, respectively, whereas the Rh^{3+}-CO species displays a single band at 2173 cm^{-1}. Upon exposure to the N-methylpirrolidine (MP) molecule, the dicarbonyl bands of Rh^{+} shift markedly to lower frequencies (2013 and 1996 cm^{-1}), while the vibration of the Rh^{3+} monocarbonyl remains essentially unchanged. This behaviour clearly indicates that MP interacts selectively with the Rh^{+} sites, leading to a net decrease in the Rh-CO bond strength, consistent with an electron-donating effect of MP that enhances back-donation from Rh^{+} to CO.

The DFT-calculated vibrational frequencies, shown in Supplementary Table 6 (models in Supplementary Fig. 31), reproduce these experimental trends with remarkable fidelity. The calculations correctly predict higher ν(CO) values for the Rh^{3+} monocarbonyl (2203 cm^{-1}) compared with the Rh^{+} dicarbonyl (2173 and 2117 cm^{-1}), reflecting the greater electrophilicity of Rh^{3+} and the corresponding reduction in metal-to-CO back-bonding. Moreover, upon adsorption of MP, the computed Rh^{+} symmetric and asymmetric CO stretching modes both shift to lower wavenumbers, from 2173 to 2163 cm^{-1} and from 2117 to 2079 cm^{-1}, respectively, mirroring the experimental redshift and confirming that MP coordination attenuates the Rh-CO bond. Although the calculations also predict a redshift for the Rh^{3+}-CO vibration, this shift is not observed experimentally, confirming that MP does not significantly interact with Rh^{3+} sites, otherwise, a comparable spectral response would be detected. This lack of experimental change is consistent with the energetic analysis presented below, which shows that MP binds much more strongly to Rh^{+} than to Rh^{3+} species.

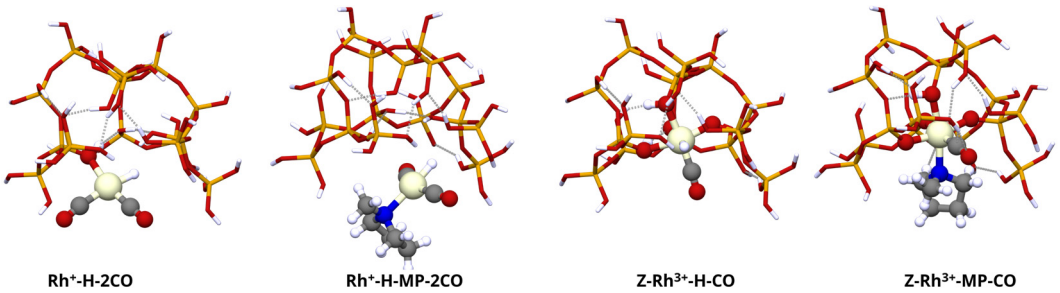
The energetic analysis further supports the vibrational evidence for selective stabilization of the Rh^{+} species upon MP adsorption. The interaction of MP with Rh^{+} is highly exothermic, as reflected by the very low relative energy obtained for Rh^{+}H-MP-2CO (−535 kJ/mol). These values indicate the formation of strongly bound adducts stabilized by electronic interactions between MP and the Rh center. In contrast, the interaction of MP with Rh^{3+} is significantly weaker: the Z-Rh^{3+}-MP-CO adduct exhibits a relative energy of −263 kJ/mol, notably less stable than either Rh^{+} complex and

even less favourable than Z-Rh^{3+}H-CO (−338 kJ/mol). This energetic hierarchy confirms that MP preferentially binds to Rh^{+} sites, in excellent agreement with the spectroscopic observation that only the Rh^{+} carbonyl bands respond to MP exposure.

Overall, the combined experimental and theoretical results provide a coherent picture in which MP adsorption selectively stabilizes Rh^{+} species through a strong donor interaction that enhances metal-CO back-bonding and weakens the CO bonds, producing the observed red-shift in ν(CO). The Rh^{3+} sites, in contrast, remain largely unaffected due to their lower affinity for the MP molecule. The consistent agreement between experimental infrared data, computed vibrational trends, and relative energies lends strong support to the proposed interaction mechanism and validates the theoretical description of these Rh-carbonyl systems.

Supplementary Table 6. Calculated vibrational frequencies of carbonyl C-O stretching of the species resulting from competitive interaction of CO and MP with the Rh^{+} and Rh^{3+} active sites. Relative energies are referenced to the optimized Rh^{+}-H-MFI and Rh^{3+}-H-MFI models plus the energies of the isolated adsorbates.

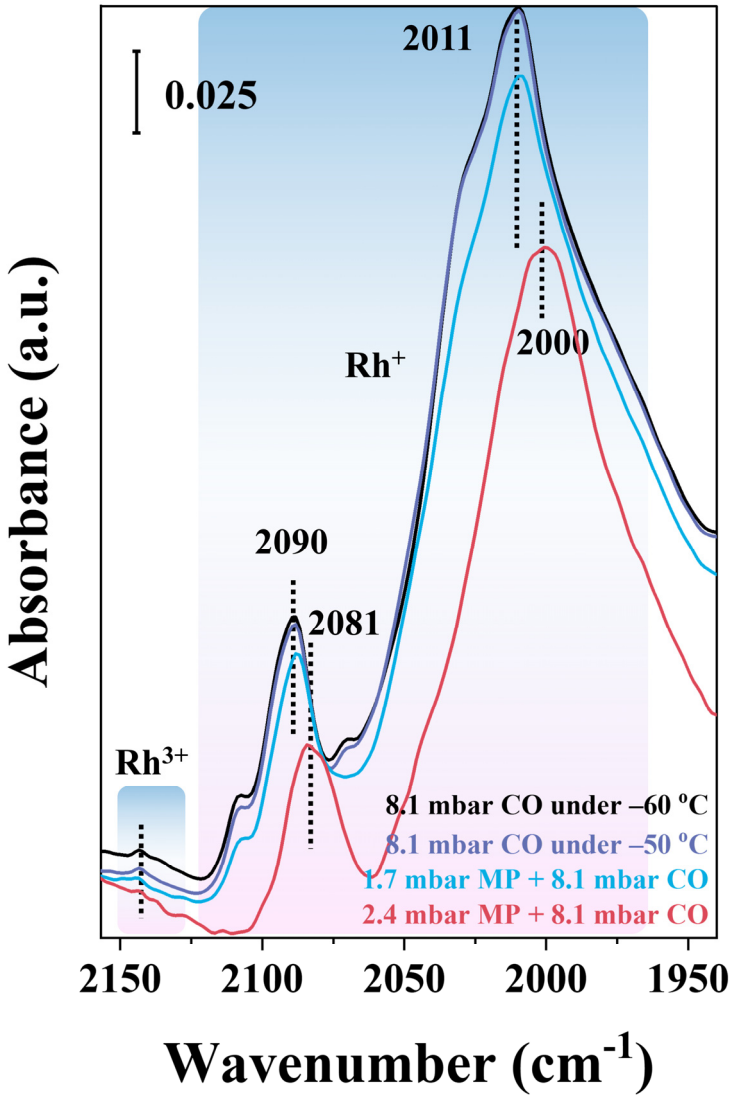
Species	Frequency (cm^{-1})	Relative Energy (kJ/mol)
Rh^{+}		
Rh^{+}-H-2CO	2173, 2117	−457.7
Rh^{+}-H-MP-2CO	2163, 2079	−535
Rh^{3+}		
Z-Rh^{3+}-H-CO	2203	−338.6
Z-Rh^{3+}-MP-CO	2140	−263



Supplementary Fig. 31. Model structure. Optimized geometries of Rh^{+} and Rh^{3+} active sites interacting with the CO and MP, used to perform normal mode analysis presented in **Supplementary Table 6**.

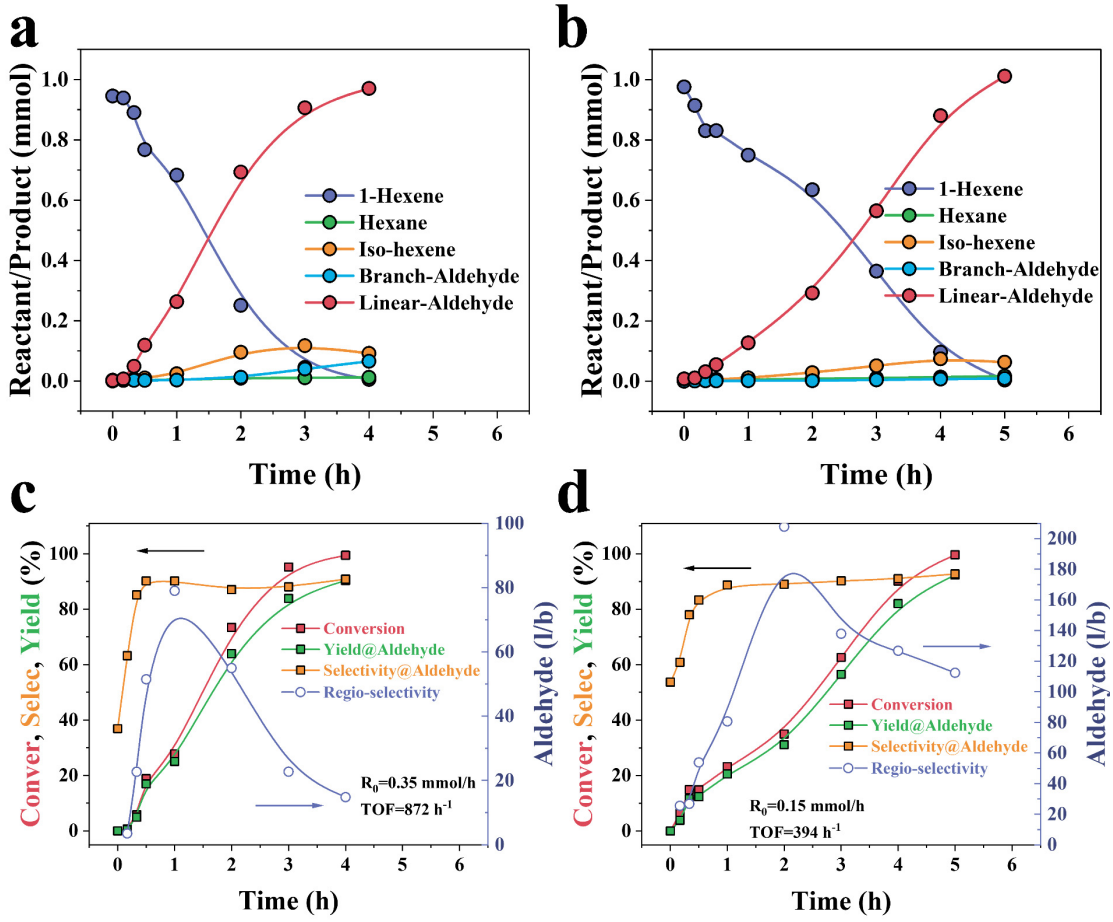
To further confirm the preferentially coordination of MP with Rh^{+}, we performed the titration experiment of MP with KRh@MFI-Cal-CO/H_2 sample, which after low-temperature CO titration, shows both Rh^{3+} and $Rh^{+}(CO)_2$ species (Supplementary Fig. 17).

Subsequently, 1.7-2.4 mbar of MP was co-added into the IR cell. A red-shift of the $Rh^{+}(CO)_2$ bands from 2090 and 2011 cm^{-1} to 2081 and 2000 cm^{-1} was observed upon 2.4 mbar MP dosing, while the position of the Rh^{3+} peak remained unchanged (Supplementary Fig. 32), in line with the IR-CO observed in KRh@MFI-Cal and KRh@MFI-Cal-MP samples in Figure 2k.

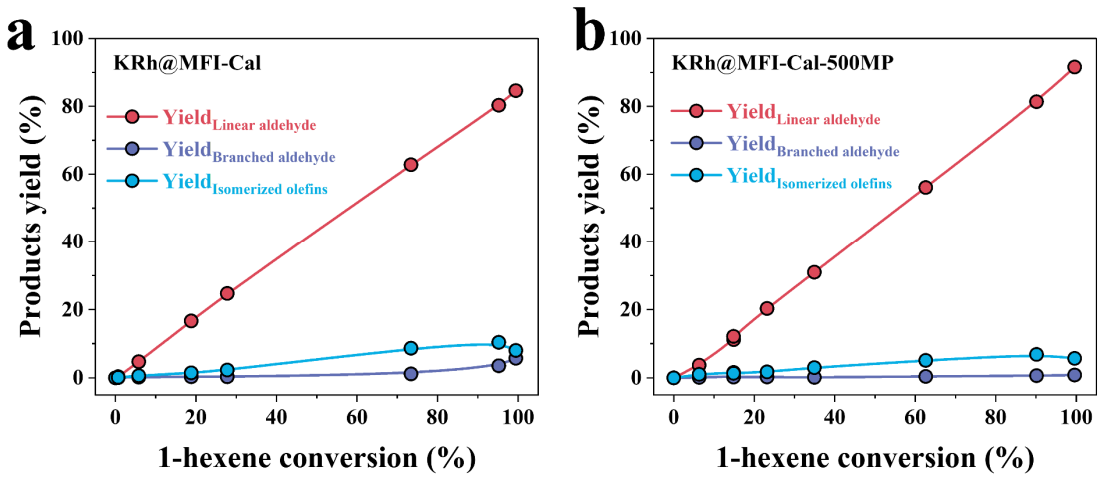


Supplementary Fig. 32. IR-CO results. IR-CO of KRh@MFI-Cal-CO/H_2 sample with MP titration.

2.15. Catalytic performance of 1-hexene hydroformylation on KRh@MFI-Cal and KRh@MFI-Cal-500MP catalysts



Supplementary Fig. 33. 1-hexene hydroformylation activity. (a, c) KRh@MFI-Cal catalyst and (b, d) KRh@MFI-Cal catalyst with a molar ratio MP/Rh = 500/1 additive. Reaction condition: 1 mmol LAO, 20 mg catalyst (0.00038 mmol Rh), 20 mg decane (internal standard), 4 mL toluene, 40 bar $CO/H_2/Ar$ (45/45/10 vol%), 80 ºC, 800 rpm, R_0, TOF and TON are values for linear aldehyde formation.

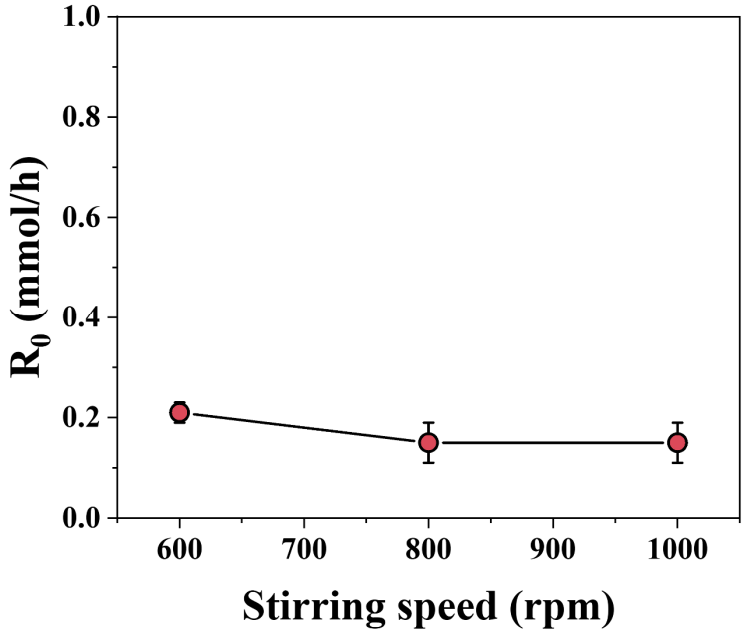


Supplementary Fig. 34. Yield of linear aldehyde, branched aldehyde, isomerized olefins as a function of 1-hexene conversion. (a) KRh@MFI-Cal, and (b) KRh@MFI-Cal-500MP catalysts. Reaction condition: 1 mmol LAO, 20 mg catalyst (0.00038 mmol Rh), 20 mg decane (internal standard), 4 mL toluene, 40 bar $CO/H_2/Ar$ (45/45/10 vol%), 80 °C, 800 rpm.

Notes: With increasing 1-hexene conversion, the yield of linear aldehyde increases nearly linearly, indicating that hydroformylation of terminal olefin is the dominant pathway. However, at conversions above 90%, the yield of isomerized olefins begins to decline, accompanied by a notable increase in branched aldehyde formation. This trend suggests that isomerized olefins serve as intermediates which are further converted into branched aldehydes in the later stage of the reaction, once most of the terminal olefins are consumed.

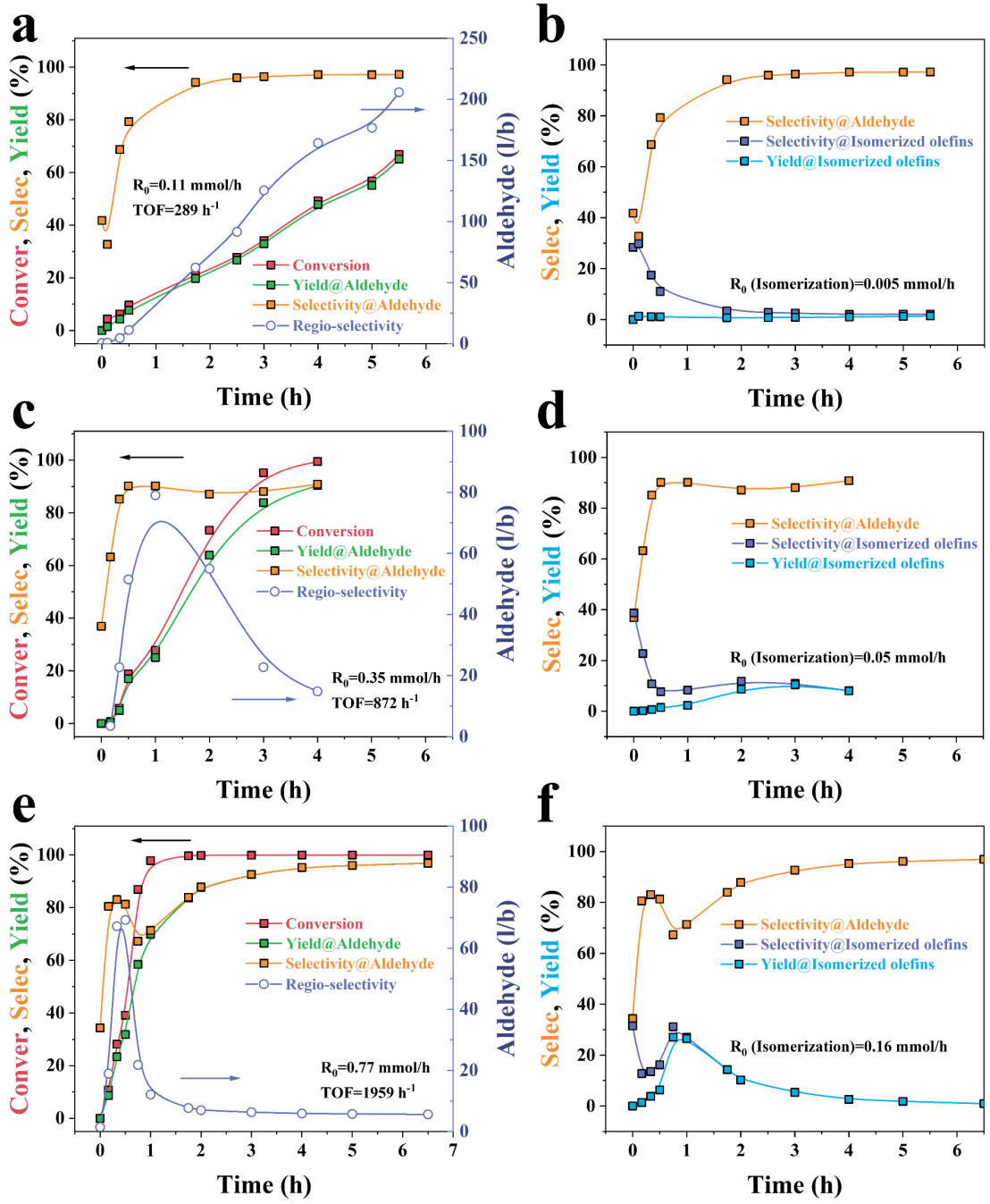
As shown in Supplementary Fig. 34, on the KRh@MFI-Cal-500MP catalyst, the yield for linear aldehyde formation is enhanced at same 1-hexene conversion, while the formation of branched aldehydes from isomerized olefins is suppressed in the presence of MP. This suggests the essential role of the MP additive in inhibiting alkene isomerization and, consequently, achieving high regioselectivity of linear aldehyde formation.

2.16. Exclude mass transport limitations



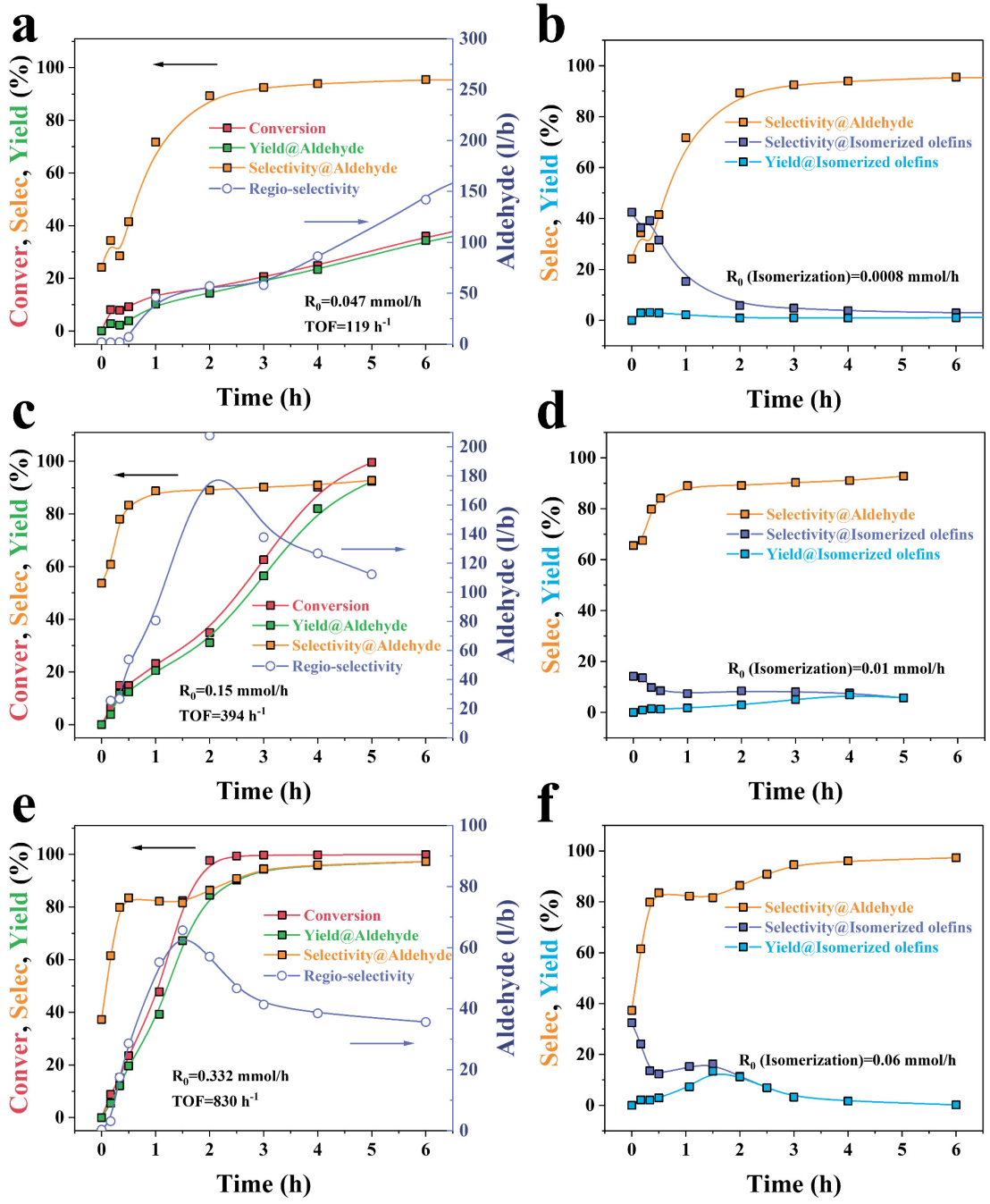
Supplementary Fig. 35. Excluding mass transfer limitations. Comparison of linear aldehyde formation rates for 1-hexene hydroformylation under 600, 800 and 1000 rpm stirring speed on KRh@MFI-Cal catalyst (Molar ratio of 500/1=MP/Rh were used in all tests). Reaction condition: 1 mmol LAO, 20 mg catalyst (0.00038 mmol Rh), 20 mg decane (internal standard), 4 mL toluene, 40 bar $CO/H_2/Ar$ (45/45/10 vol%), 80 °C, 600-1000 rpm, R_0, TOF and TON are values for linear aldehyde formation.

2.17. Apparent activation energy of KRh@MFI-Cal catalyst for 1-hexene hydroformylation and isomerization



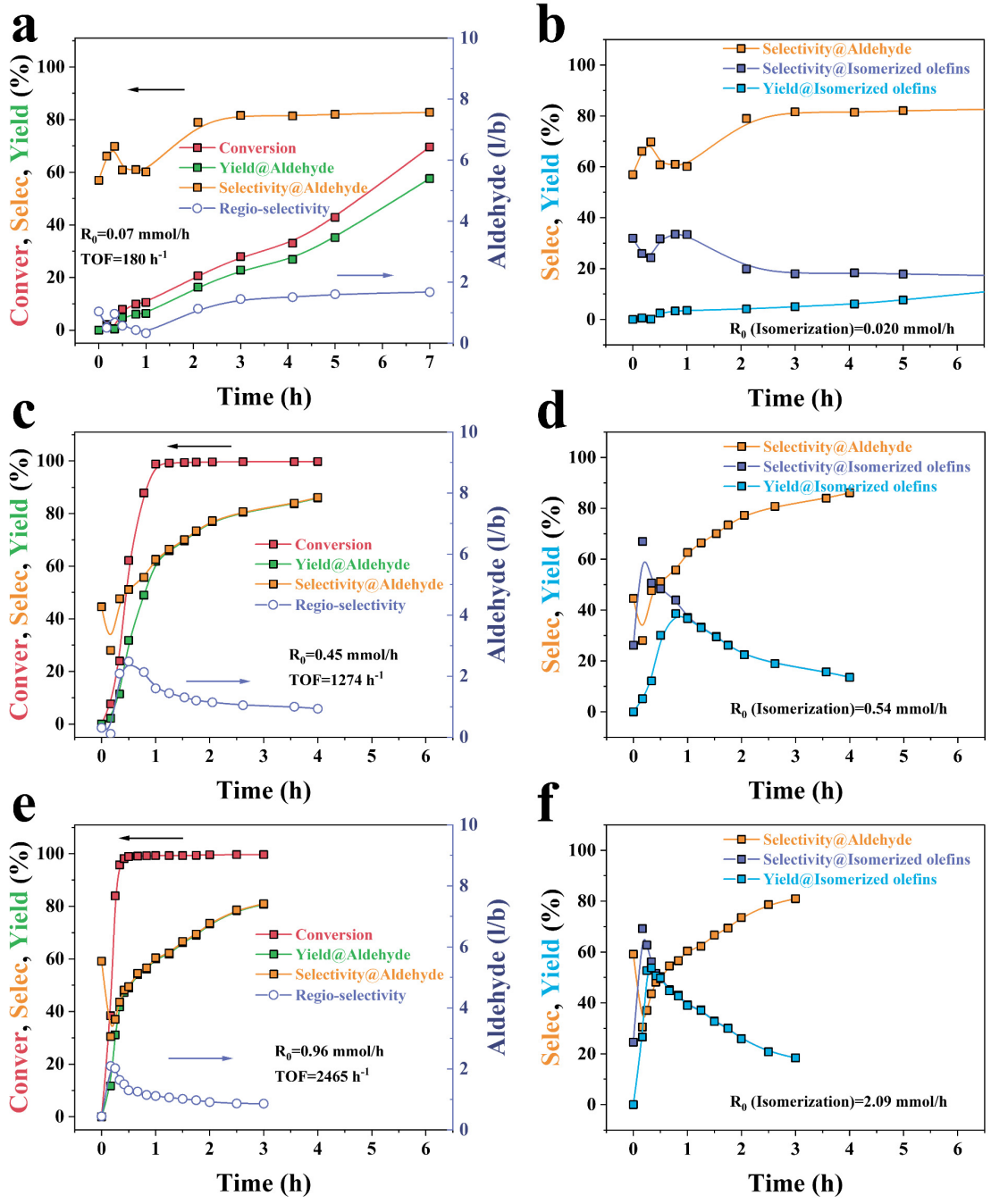
Supplementary Fig. 36. 1-Hexene hydroformylation activity of KRh@MFI-Cal catalyst under different reaction temperatures. (a, b) 50 °C, (c, d) 80 °C, (e, f) 100 °C (1-hexene conversion, aldehyde yield and selectivity, regioselectivity (l/b), isomerized olefins selectivity and yield). Reaction condition: 1 mmol LAO, 20 mg catalyst (0.00038 mmol Rh), 20 mg decane (internal standard), 4 mL toluene, 40 bar $CO/H_2/Ar$ (45/45/10 vol%), 50-100 °C, 800 rpm, R_0, TOF and TON are values for linear aldehyde formation.

2.18. Apparent activation energy of KRh@MFI-Cal catalyst for 1-hexene hydroformylation and isomerization in the presence of N-methylpyrrolidine

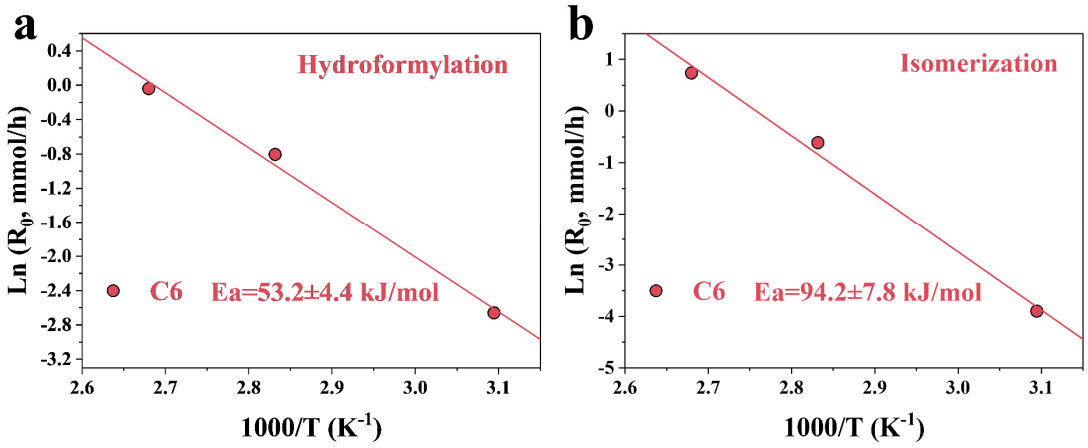


Supplementary Fig. 37. 1-Hexene hydroformylation activity of KRh@MFI-Cal catalyst with N-methylpyrrolidine additive under different reaction temperatures. (a, b) 50 °C, (c, d) 80 °C, (e, f) 100 °C (1-hexene conversion, aldehyde yield and selectivity, regioselectivity (l/b), isomerized olefins selectivity and yield). Reaction condition: 1 mmol LAO, 20 mg catalyst (0.00038 mmol Rh), 20 mg decane (internal standard), 4 mL toluene, 40 bar $CO/H_2/Ar$ (45/45/10 vol%), 50-100 °C, 800 rpm, R_0, TOF and TON are values for linear aldehyde formation.

2.19. Apparent activation energy of $RhHCO(PPh_3)_3$ catalyst for 1-hexene hydroformylation

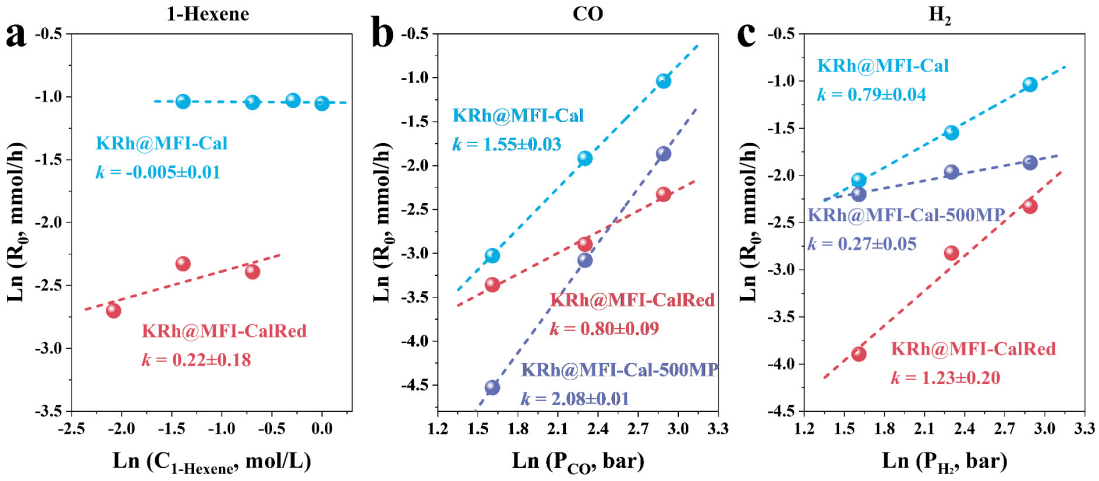


Supplementary Fig. 38. 1-Hexene hydroformylation activity of $RhHCO(PPh_3)_3$ catalyst under different reaction temperatures. (a, b) 50 °C, (c, d) 80 °C, (e, f) 100 °C (1-hexene conversion, aldehyde yield and selectivity, regioselectivity (l/b), isomerized olefins selectivity and yield). Reaction condition: 1 mmol LAO, 0.36 mg catalyst (0.00038 mmol Rh), 20 mg decane (internal standard), 4mL toluene, 40 bar $CO/H_2/Ar$ (45/45/10 vol%), 50-100 °C, 800 rpm, R_0, TOF and TON are values for linear aldehyde formation.



Supplementary Fig. 39. Apparent activation energy of 1-hexene. (a) Hydroformylation and (b) isomerization on $RhHCO(PPh_3)_3$ catalyst.

2.20. Reaction orders of 1-hexene, CO and H_2 on KRh@MFI-Cal, KRh@MFI-CalRed-CO and KRh@MFI-Cal-500MP catalysts



Supplementary Fig. 40. Kinetics. Reaction orders of 1-hexene, CO and H_2 on KRh@MFI-Cal, KRh@MFI-CalRed-CO and KRh@MFI-Cal-500MP catalysts.

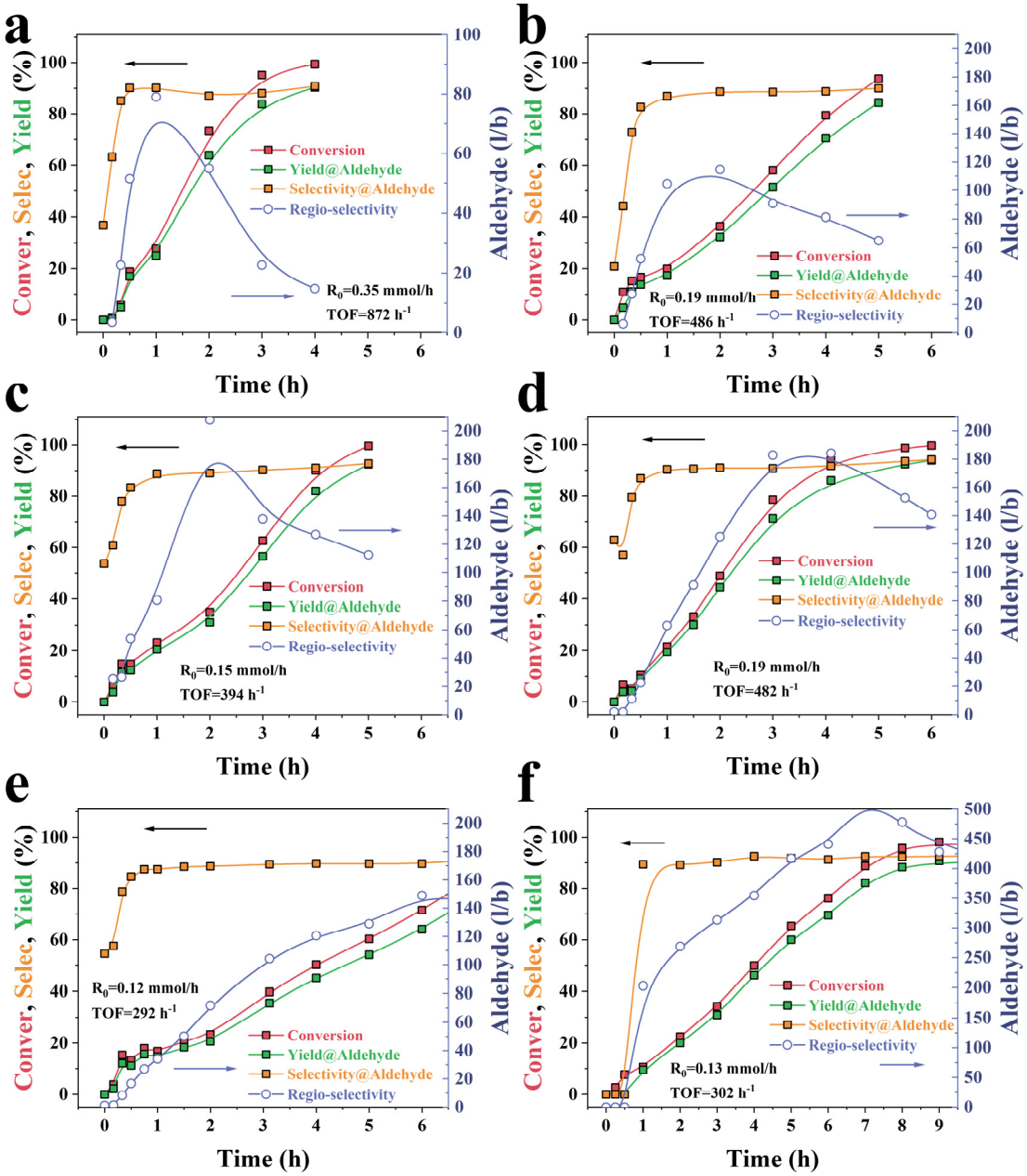
Notes: The reaction orders for linear aldehyde formation on KRh@MFI-Cal, KRh@MFI-CalRed-CO and KRh@MFI-Cal-500MP are shown in Supplementary Fig. 40. The reaction orders with respect to 1-hexene, CO, and H_2 vary significantly among the different catalysts, indicating distinct reaction regimes and rate-determining steps. For all catalysts, the near-zero reaction order in 1-hexene suggests that olefin coordination is not rate-limiting, consistent with strong confinement or saturation of olefin adsorption within the zeolite channels.

With respect to CO, the high positive reaction order for KRh@MFI-Cal and KRh@MFI-Cal-500MP indicate that CO insertion plays a dominant role in determining the reaction rate, whereas the lower CO dependence observed for KRh@MFI-CalRed-CO suggests partial saturation of CO coordination or competitive site occupation. The reaction orders in H_2 further reveal differences in hydrogen activation: the higher H_2 order for KRh@MFI-CalRed-CO points to hydrogenation of the acyl intermediate as a kinetically relevant step, while the moderate H_2 dependence for KRh@MFI-Cal indicates a more balanced contribution of CO insertion and hydrogenation.

Overall, these distinct kinetic dependencies demonstrate that different Rh species inside KRh@MFI catalyst are related to olefin adsorption, CO insertion, and hydrogenation steps, which ultimately governs both activity and regioselectivity in 1-hexene hydroformylation.

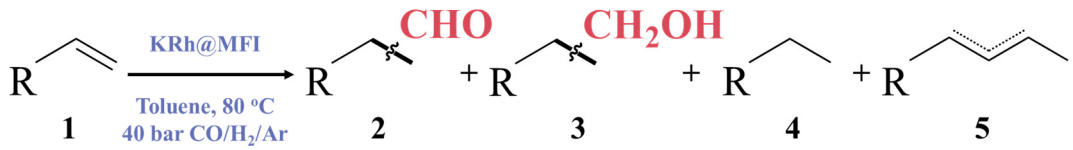
2.21. Optimum loading of organic additives (MP and NMP) in 1-hexene hydroformylation

In order to know the optimum loading of additives during reaction, experiments with different MP/Rh or NMP/Rh molar ratios have been performed.



Supplementary Fig. 41. 1-hexene hydroformylation activity of KRh@MFI-Cal catalyst with different MP additive loading amount. Molar ratio of MP/Rh = (a) 0, (b) 250, (c) 500, (d) 1000, (e) 4000) and (f) MP as solvent. Reaction condition: 1 mmol LAO, 20 mg catalyst (0.00038 mmol Rh), 20 mg decane (internal standard), 4 mL toluene, 40 bar $CO/H_2/Ar$ (45/45/10 vol%), 250-4000/1 molar ratio MP/Rh, 80 °C, 800 rpm, R_0, TOF and TON are values for linear aldehyde formation.

Supplementary Table 7. 1-hexene hydroformylation activity. Catalytic results for KRh@MFI catalyst of 1-hexene hydroformylation in the presence of N-Methylpyrrolidine.[a]



Entry	Organic additive	Molar ratio to Rh	Conv. (%)	Selec. (%) Aldehyde (L)[b]	l/b[c]	Yield (%)				R_0 (mmol/h)[d] L-Aldehyde	R_0 (mmol/h)[d] Iso-Alkenes	TON[e]	TOF (h^{-1})[f]
						2	3	4	5				
1[g]	/	/	99.5	90.9 (85.1)	15	90.4	0	1.1	8.0	0.35	0.050	2024	872
2	MP	250	93.8	90.0 (88.7)	65	84.4	0	1.2	8.1	0.19	0.014	2158	486
3	MP	500	99.6	92.8 (91.9)	112	92.4	0	1.5	5.7	0.15	0.010	2386	394
4[h]	MP	1000	99.6	94.2 (93.6)	141	93.9	0	1.3	4.4	0.19	0.011	2364	482
5[i]	MP	4000	84.4	91.3 (90.6)	145	77.0	0	1.1	6.3	0.12	0.010	1943	292
6[j]	MP	Solvent	98.1	92.6 (92.4)	428	90.9	0	1.4	5.8	0.13	0.009	2216	302

[a] Reaction conditions: 1 mmol LAO, 20 mg catalyst (0.00038 mmol Rh), 20 mg decane (internal standard), 4 mL toluene, 40 bar $CO/H_2/Ar$ (45/45/10 vol%), 80 °C, 800 rpm and 5h reaction.

[b] Total aldehyde selectivity (L = Linear aldehyde selectivity).

[c] Ratio of the linear aldehyde to the branched aldehyde.

[d] Reaction rate for linear aldehyde formation and reaction rate for isomerized alkenes formation, mmol/h, calculated when LAO conversion is < 20%.

[e] mmol of linear aldehyde/total mmol of Rh at 5h reaction time.

[f] Rate for the formation of linear aldehyde/total mmol of Rh.

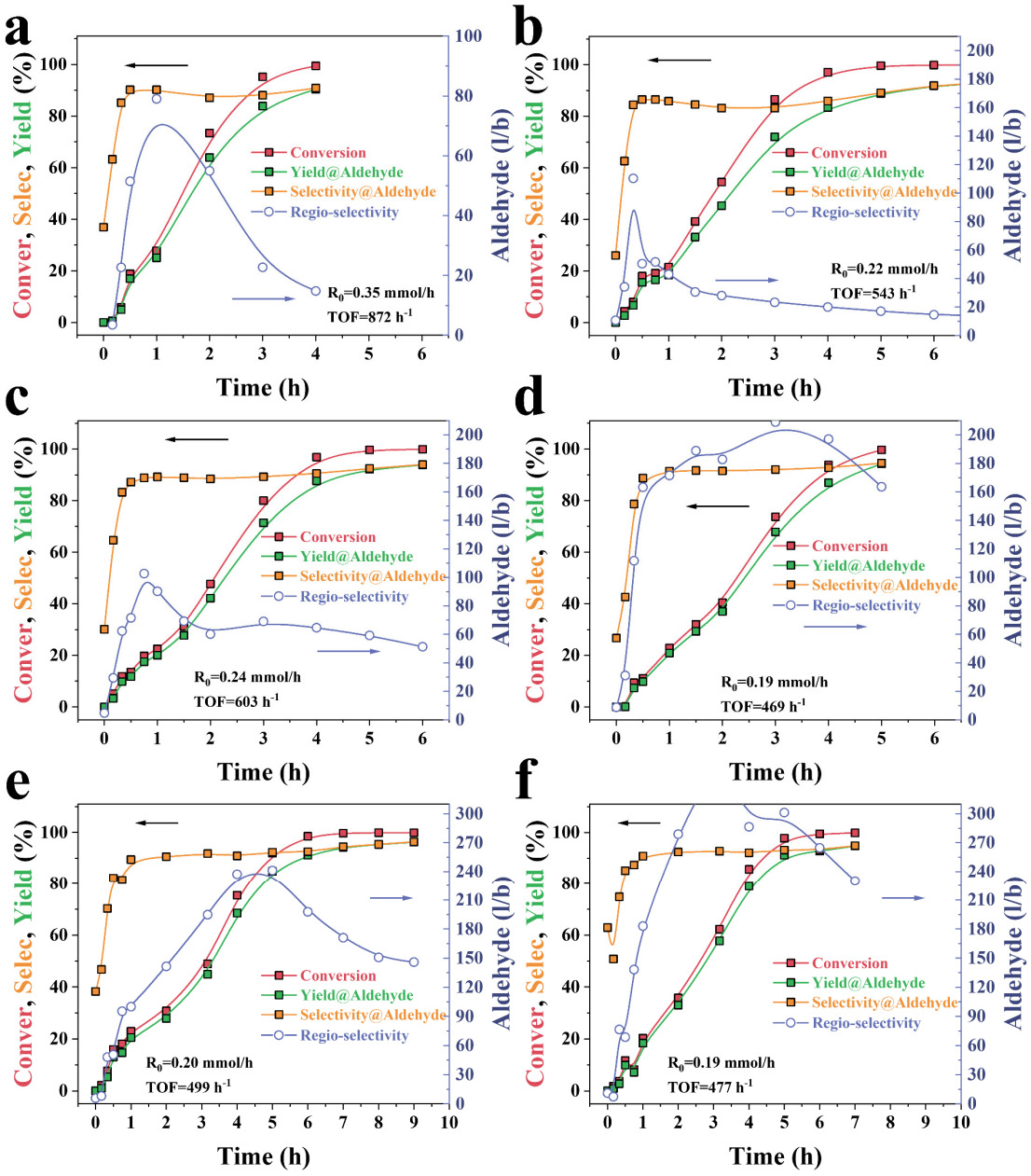
[g] 4h reaction.

[h] 6h reaction.

[i] 7h reaction.

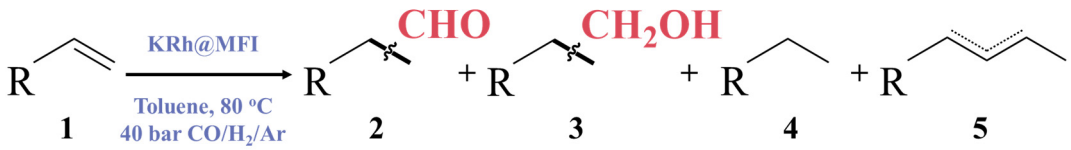
[j] 9h reaction.

Thus, minimum N-methylpyrrolidine loading is MP/Rh = 500/1 molar ratio loading, nearly 92% linear aldehyde with l/b=112 at ~100% conversion.



Supplementary Fig. 42. 1-hexene hydroformylation activity of KRh@MFI-Cal with different NMP additive loading amount. Molar ratio of NMP/Rh = (a) 0, (b) 1000, (c) 2000, (d) 4000, (e) 6000, (f) 8000. Reaction condition: 1 mmol LAO, 20 mg catalyst (0.00038 mmol Rh), 20 mg decane (internal standard), 4 mL toluene, 40 bar $CO/H_2/Ar$ (45/45/10 vol%), 1000-8000/1 molar ratio NMP/Rh, 80 °C, 800 rpm, R_0, TOF and TON are values for linear aldehyde formation.

Supplementary Table 8. 1-hexene hydroformylation. Catalytic results for KRh@MFI-Cal catalyst of 1-hexene hydroformylation in the presence of NMP.[a]



Entry	Organic additive	Molar ratio to Rh	Conv. (%)	Selec. (%) Aldehyde (L)[b]	l/b[c]	Yield (%)				R_0 (mmol/h)[d] L-Aldehyde	R_0 (mmol/h)[d] Iso-Alkenes	TON[e]	TOF (h^{-1})[f]
						2	3	4	5				
1	/	/	99.5	90.9 (85.1)	15	90.4	0	1.1	8.0	0.35	0.050	2024	872
2	NMP	1000	97.1	85.9 (81.8)	20	83.4	0	1.0	12.7	0.22	0.029	2005	543
3	NMP	2000	96.9	90.5 (89.1)	65	87.6	0	1.2	8.1	0.24	0.014	2131	603
4	NMP	4000	93.8	92.7 (92.2)	197	87.0	0	1.1	5.8	0.19	0.013	2205	469
5[g]	NMP	4000	99.7	94.5 (93.9)	164	94.2	0	1.1	4.4	0.19	0.013	2401	469
6	NMP	6000	75.4	90.9 (90.5)	237	68.5	0	1.1	5.8	0.20	0.009	1672	499
7	NMP	8000	85.7	92.1 (91.8)	287	78.9	0	1.1	5.6	0.19	0.008	1856	477
8[h]	NMP	Solvent	27.0	90.2 (90.2)	∞	24.4	0	0.6	2.0	0.03	0.002	435	82

[a] Reaction conditions: 1 mmol LAO, 20 mg catalyst (0.00038 mmol Rh), 20 mg decane (internal standard), 4 mL toluene, 40 bar $CO/H_2/Ar$ (45/45/10 vol%), 80 °C, 800 rpm and 4h reaction.

[b] Total aldehyde selectivity (L = Linear aldehyde selectivity).

[c] Ratio of the linear aldehyde to the branched aldehyde.

[d] Reaction rate for linear aldehyde formation and reaction rate for isomerized alkenes formation, mmol/h, calculated when LAO conversion is < 20%.

[e] mmol of linear aldehyde/total mmol of Rh at 4h reaction time.

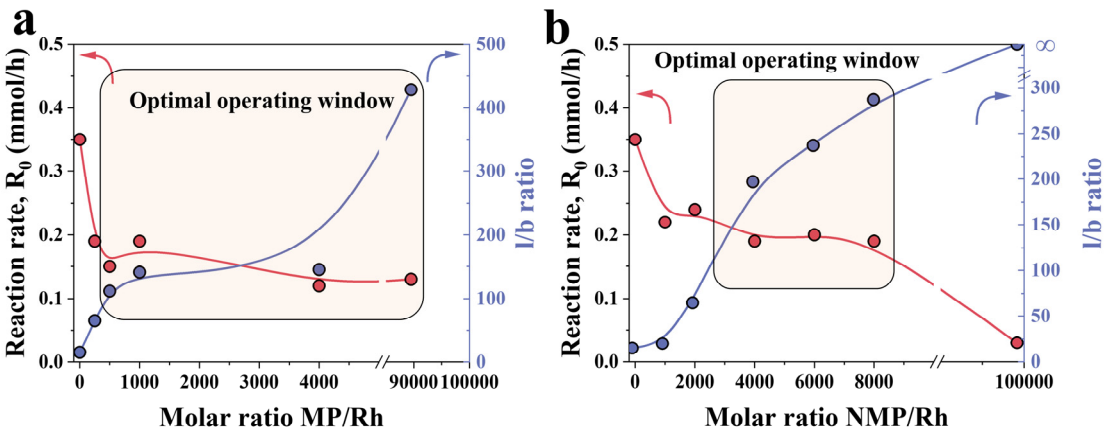
[f] Rate for the formation of linear aldehyde/total mmol of Rh.

[g] 5h reaction.

[h] Herein, NMP is used as solvent for reaction, 6h reaction result.

Thus, optimum NMP loading is NMP/Rh = 4000/1 molar ratio loading, nearly 92.2% linear aldehyde selectivity with l/b=197 at 93.8% conversion, even at 99.6 % conversion, l/b still keep at 164 with 94% linear aldehyde selectivity.

Moreover, when NMP is used as the solvent instead of toluene, the reaction rate becomes very low while only linear aldehyde is formed, indicating a strong steric effect imposed by the bulkier NMP molecules inside MFI zeolite.



Supplementary Fig. 43. Optimum MP or NMP operating windows. Correlation of linear aldehyde formation rate and l/b ratio with (a) MP and (b) NMP additive amount in 1-hexene hydroformylation.

Notes: As Supplementary Fig. 43 shown, increasing the amount of MP and NMP, the reaction rate gradually decreases and reaches a plateau with MP used as solvent. In contrast, the hydroformylation rate drops to a very low level in the presence of NMP as solvent. This difference is reasonable, as MP has a smaller molecular size than NMP and can more readily diffuse in and out of the MFI zeolite channels, whereas excessive NMP may hinder olefin accessibility within the zeolite channels.

Based on these results, we determined an optimal operating windows for MP and NMP, respectively. The optima MP/Rh molar ratio is 500 until MP as solvent, whereas the optimal NMP/Rh molar ratio is approximately 3000-8000.

Herein, elemental analysis was performed on the spent catalysts to quantify the residual MP content after hydroformylation reaction. After reaction, the samples were cooled down, depressurized, and washed several times with toluene. During these post-treatment processes, the weakly coordinated MP molecules and the free MP molecules physically confined inside the MFI channels were mostly desorbed and washed away. The residual MP/Rh molar ratio on the spent catalyst determined by CHNS elemental analysis is 15-19 (Supplementary Table 9, assuming that all detected nitrogen originates exclusively from the MP additive), which is significantly lower than the initial feeding ratio (500-1000). Furthermore, the Rh free K-MFI-Cal-500MP (after reaction) gives similar nitrogen amount, which indicates that the MP coordinated to Rh should be at least stoichiometric molar ratio.

The excessive MP dosage (molar ratio MP/Rh > 500) is required because hydroformylation is performed under elevated temperatures and high CO/H_2 pressures, where CO behaves as a strongly ligand and continuously competes with MP (or NMP) for Rh^+ coordination sites. As a result, ligand exchange between CO and MP is inevitable under reaction conditions. According to Le Chatelier's principle, maintaining a large excess of MP in the liquid phase (MP/Rh > 500) is thermodynamically necessary to shift the equilibrium toward the MP-coordinated Rh^+ state. This high ligand concentration continuously replenishes the Rh^+-MP complexes as MP is displaced by CO during catalysis, thereby ensuring persistent suppression of the isomerization-active Rh^+ species throughout the reaction. In addition to the stoichiometric Rh-MP complex, MP can also interact with MFI through silanol groups (≡Si-OH). The residual MP molecules, particularly those located in the vicinity of Rh^+ centers, may also create a sterically confined microenvironment that suppresses α-olefin insertion into Rh^+-$H(CO)_2$-MP intermediates and inhibits the undesired olefin isomerization pathway catalyzed by Rh^+.

Supplementary Table 9. Characterizations. Elemental analysis results on KRh@MFI catalysts.

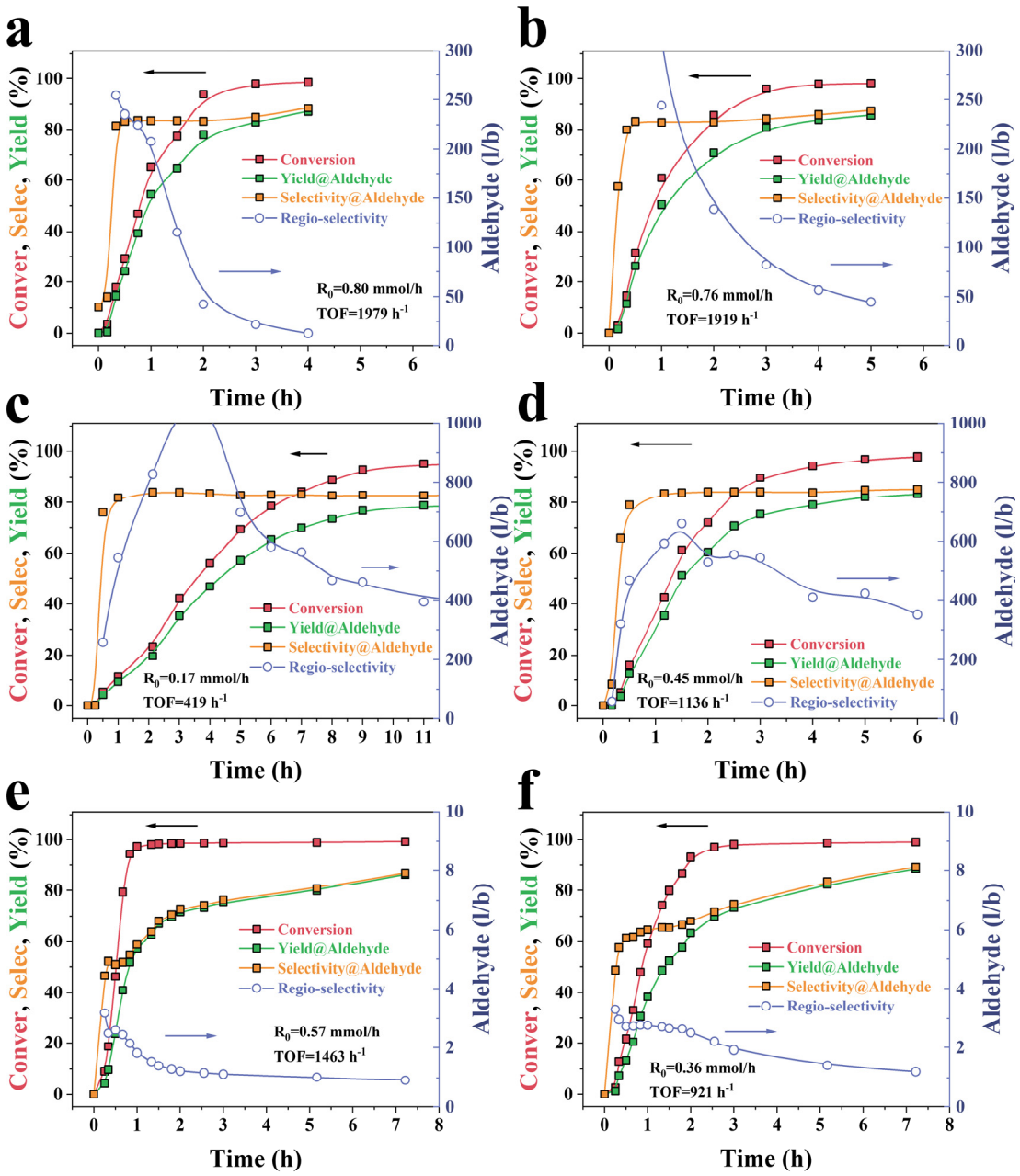
Sample	C (wt%) [a]	H (wt%) [a]	N (wt%) [a]	S (wt%) [a]	Rh (wt%) [b]	MP/Rh molar ratio [c]
K-MFI-Cal-500MP	2.46	0.48	0.29	0	0	-
KRh@MFI-Cal (Before reaction)	1.44	0.29	0	0	0.2	0
KRh@MFI-Cal-500MP (After reaction)	8.47	1.49	0.52	0	0.2	19
KRh@MFI-Cal-MP solvent (After reaction)	2.83	0.58	0.41	0	0.2	15
KRh@MFI-Cal-4000NMP (After reaction)	8.62	1.50	0.29	0	0.2	11

[a] Measured by elemental analysis.

[b] Measured by ICP-OES.

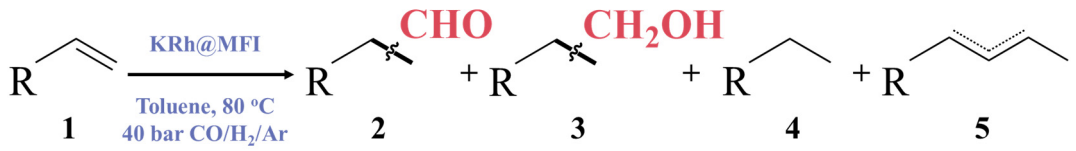
[c] The MP content was calculated based on the nitrogen content, and the molar ratio of residual MP to Rh in the catalyst was determined.

2.22. 1-Octene hydroformylation (C8 LAO)



Supplementary Fig. 44. 1-Octene hydroformylation activity. (a) KRh@MFI-Cal, (b) KRh@MFI-Cal with a molar ratio MP/Rh = 500/1 additive, (c) KRh@MFI-Cal with MP as solvent, (d) KRh@MFI-Cal with a molar ratio NMP/Rh = 4000/1 additive, (e) commercial homogeneous Wilkinson-type catalyst $RhHCO(PPh_3)_3$ and (f) $RhHCO(PPh_3)_3$ with a molar ratio MP/Rh = 500/1 additive. Reaction condition: 1 mmol LAO, 20 mg catalyst (0.00038 mmol Rh), 20 mg decane (internal standard), 4 mL toluene, 40 bar $CO/H_2/Ar$ (45/45/10 vol%), 80 °C, 800 rpm, R_0, TOF and TON are values for linear aldehyde formation.

Supplementary Table 10. 1-Octene hydroformylation activity. Catalytic results for KRh@MFI-Cal catalyst of 1-octene hydroformylation at 80 °C.[a]



Entry	Catalysts	Conv. (%)	Selec. (%) Aldehyde (L)[b]	l/b[c]	Yield (%)				R_0 (mmol/h)[d] L-Aldehyde	R_0 (mmol/h)[d] Iso-Alkenes	TON[e]	TOF (h^{-1})[f]
					2	3	4	5				
1	KRh@MFI-Cal	97.9	84.8 (81.0)	21.7	83.0	0	3.0	11.9	0.80	0.221	1933	1979
2	KRh@MFI-Cal-500MP	96.0	84.2 (83.2)	82.0	80.8	0	1.7	13.5	0.76	0.122	2060	1919
3[g]	KRh@MFI-Cal-MP solvent	92.8	82.8 (82.6)	462	76.9	0	1.2	14.8	0.17	0.026	1977	419
4[h]	KRh@MFI-Cal-4000NMP	97.9	85.0 (84.8)	352	83.2	0	1.5	13.1	0.45	0.079	2122	1136
5[i]	$RhHCO(PPh_3)_3$	97.4	58.8 (38.0)	1.8	57.2	0	8.0	32.1	0.57	0.56	802	1463
6[j]	$RhHCO(PPh_3)_3$-500MP	93.1	68.1 (48.7)	2.5	63.4	0	2.1	27.6	0.36	0.23	1023	921

[a] Reaction conditions: 1 mmol LAO, 20 mg catalyst (0.00038 mmol Rh), 20 mg decane (internal standard), 4 mL toluene, 40 bar $CO/H_2/Ar$ (45/45/10 vol%), 80 °C, 800 rpm and 3h reaction. For $RhHCO(PPh_3)_3$ catalyst, 0.36 mg catalyst with 0.00038 mmol Rh is used.

[b] Total aldehyde selectivity (L = Linear aldehyde selectivity).

[c] Ratio of the linear aldehyde to the branched aldehyde.

[d] Reaction rate for linear aldehyde formation and reaction rate for isomerized alkenes formation, mmol/h, calculated when LAO conversion is < 20%.

[e] mmol of linear aldehyde/total mmol of Rh at 3h reaction time.

[f] Rate for the formation of linear aldehyde/total mmol of Rh.

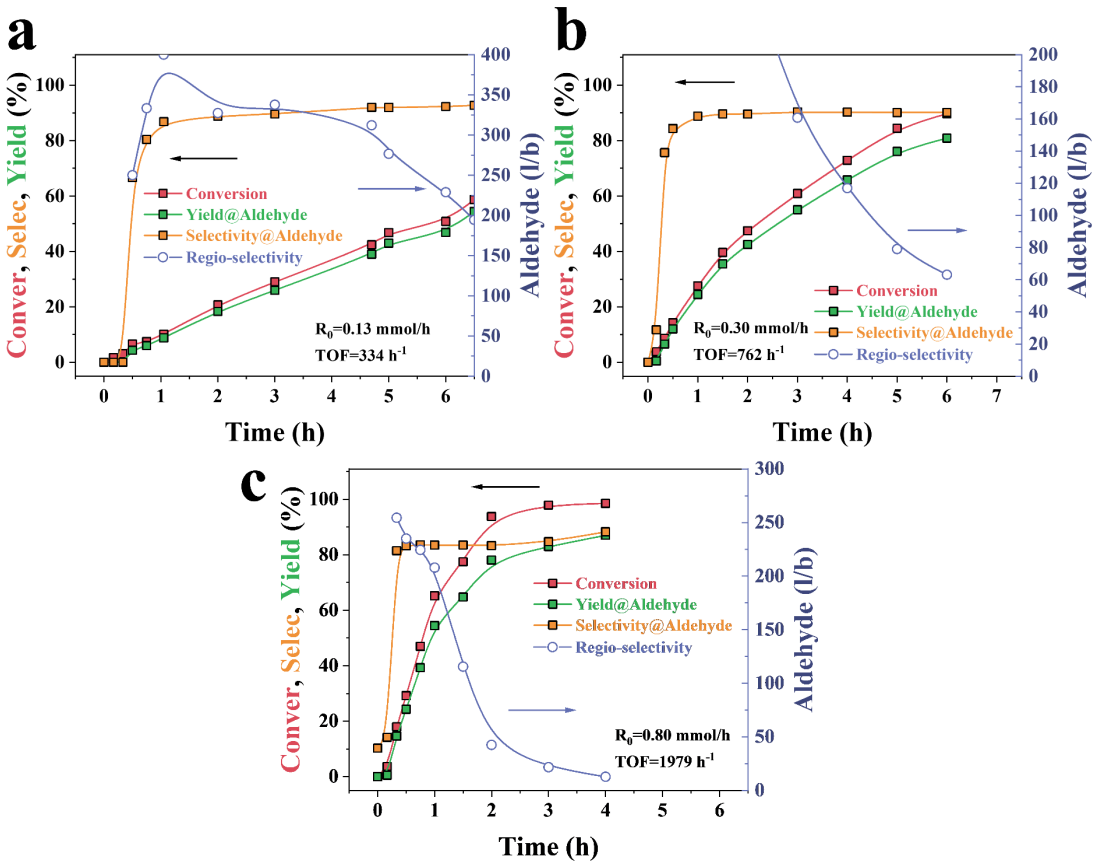
[g] 9h reaction.

[h] 6h reaction.

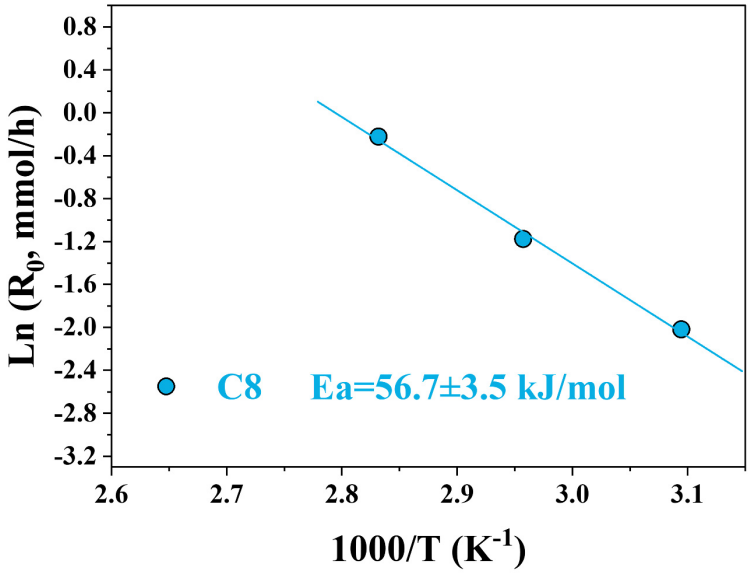
[i] 1h reaction.

[j] 2h reaction.

2.23. Apparent activation energy of KRh@MFI-Cal catalyst for 1-octene hydroformylation

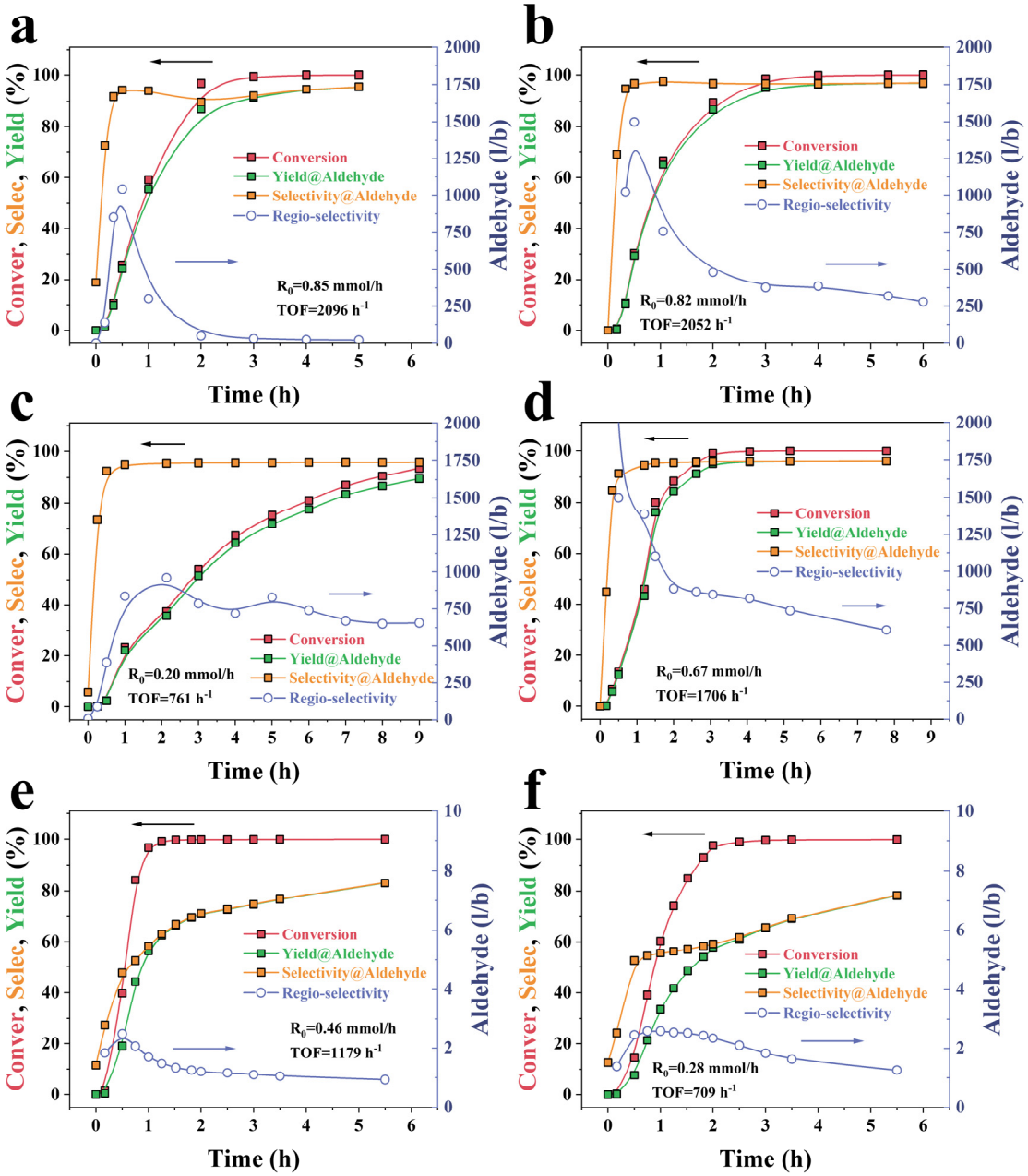


Supplementary Fig. 45. 1-Octene hydroformylation activity of KRh@MFI-Cal catalyst under different reaction temperature. (a) 50 ºC, (b) 65 ºC and (c) 80 ºC (1-octene conversion, aldehyde yield, aldehyde selectivity and regioselectivity). Reaction condition: 1 mmol LAO, 20 mg catalyst (0.00038 mmol Rh), 20 mg decane (internal standard), 4 mL toluene, 40 bar $CO/H_2/Ar$ (45/45/10 vol%), 50-80 ºC, 800 rpm, R_0, TOF and TON are values for linear aldehyde formation.



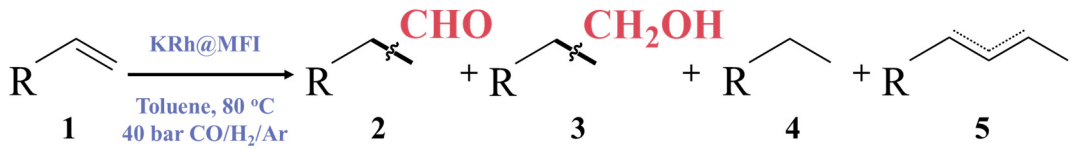
Supplementary Fig. 46. Kinetics. Apparent activation energy of 1-octene hydroformylation on KRh@MFI-Cal catalyst.

2.24. 1-Decene hydroformylation (C10 LAO)



Supplementary Fig. 47. 1-Decene hydroformylation activity. (a) KRh@MFI-Cal, (b) KRh@MFI-Cal with a molar ratio MP/Rh = 500/1 additive, (c) KRh@MFI-Cal with MP as solvent, (d) KRh@MFI-Cal with a molar ratio NMP/Rh = 4000/1 additive, (e) commercial homogeneous Wilkinson-type catalyst $RhHCO(PPh_3)_3$ and (f) $RhHCO(PPh_3)_3$ with a molar ratio MP/Rh = 500/1 additive. Reaction condition: 1 mmol LAO, 20 mg catalyst (0.00038 mmol Rh), 20 mg isooctane (internal standard), 4 mL toluene, 40 bar $CO/H_2/Ar$ (45/45/10 vol%), 80 °C, 800 rpm, R_0, TOF and TON are values for linear aldehyde formation.

Supplementary Table 11. 1-Decene hydroformylation activity. Catalytic results for KRh@MFI-Cal catalyst of 1-decene hydroformylation at 80 °C.[a]



Entry	Catalysts	Conv. (%)	Selec. (%) Aldehyde (L)[b]	l/b[c]	Yield (%)				R_0 (mmol/h)[d] L-Aldehyde	R_0 (mmol/h)[d] Iso-Alkenes	TON[e]	TOF (h^{-1})[f]
					2	3	4	5				
1	KRh@MFI-Cal	99.4	92.1 (89.2)	30	91.6	0	1.2	6.6	0.85	0.036	2137	2096
2	KRh@MFI-Cal-500MP	98.5	96.8 (96.5)	378	95.3	0	0.5	2.6	0.82	0.018	2279	2052
3[g]	KRh@MFI-MP solvent	93.6	95.7 (95.6)	655	89.6	0	1.1	2.9	0.20	0.013	1943	761
4[h]	KRh@MFI-Cal-4000NMP	99.8	95.9 (95.8)	817	95.7	0	1.0	3.1	0.67	0.017	2406	1706
5[i]	$RhHCO(PPh_3)_3$	96.7	58.3 (36.7)	1.7	56.3	0	1.8	38.6	0.46	0.57	816	1179
6[j]	$RhHCO(PPh_3)_3$ -500MP	97.6	59.1 (41.5)	2.3	57.7	0	1.1	38.8	0.28	0.27	811	709

[a] Reaction conditions: 1 mmol LAO, 20 mg catalyst (0.00038 mmol Rh), 20 mg isooctane (internal standard), 4 mL toluene, 40 bar $CO/H_2/Ar$ (45/45/10 vol%), 80 °C, 800 rpm and 3h reaction. For $RhHCO(PPh_3)_3$ catalyst, 0.36 mg catalyst with 0.00038 mmol Rh is used.

[b] Total aldehyde selectivity (L = Linear aldehyde selectivity).

[c] Ratio of the linear aldehyde to the branched aldehyde.

[d] Reaction rate for linear aldehyde formation and reaction rate for isomerized alkenes formation, mmol/h, calculated when LAO conversion is < 20%.

[e] mmol of linear aldehyde/total mmol of Rh at 3h reaction time.

[f] Rate for the formation of linear aldehyde/total mmol of Rh.

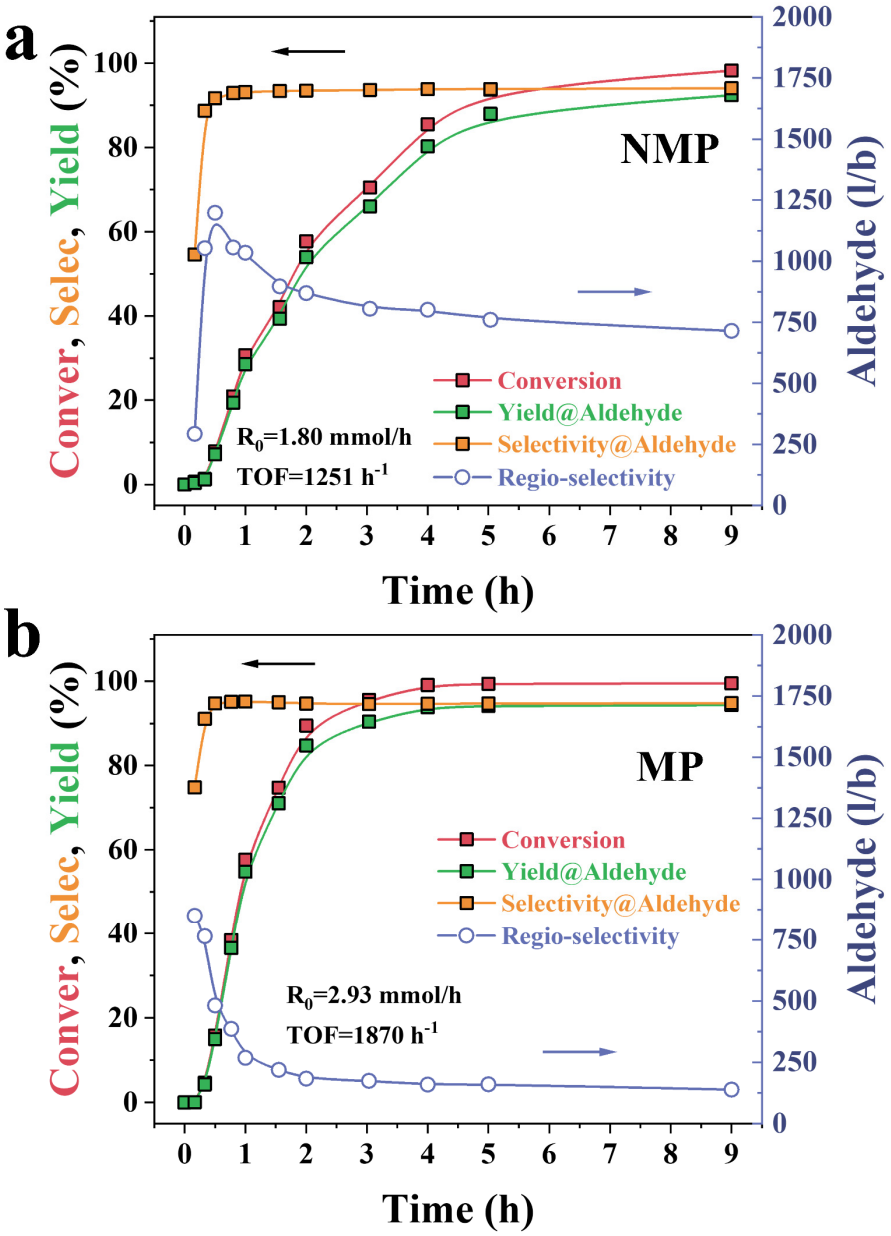
[g] 9h reaction.

[h] 4h reaction.

[i] 1h reaction.

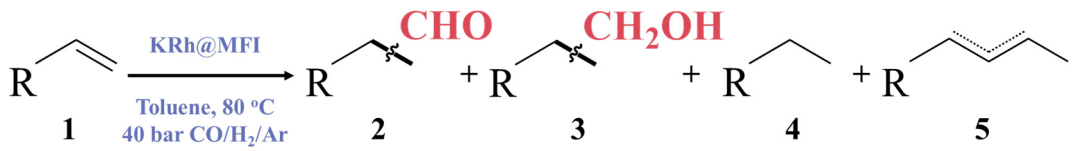
[j] 2h reaction.

2.25. 1-Decene hydroformylation at scaled-up concentration on KRh@MFI-Cal catalyst in the presence of NMP or MP



Supplementary Fig. 48. Scaled-up investigation. 1-Decene hydroformylation activity of KRh@MFI-Cal catalyst with a molar ratio (a) NMP/Rh = 4000/1 and (b) MP/Rh = 500/1 additive under 1 mol/L substrate concentration. Reaction condition: 4 mmol LAO, 80 mg catalyst (0.00152 mmol Rh), 80 mg isooctane (internal standard), all liquid components were dissolved in toluene to a final volume of 4 mL, 40 bar $CO/H_2/Ar$ (45/45/10 vol%), 80 °C, 800 rpm, R_0, TOF and TON are values for linear aldehyde formation.

Supplementary Table 12. Scaled-up investigation. Catalytic results for KRh@MFI-Cal catalyst of 1-decene hydroformylation at 80 °C under 1 mol/L reactant concentration.[a]



Entry	Catalysts	Conv. (%)	Selec. (%) Aldehyde (L)[b]	l/b[c]	Yield (%)				R_0 (mmol/h)[d] L-Aldehyde	R_0 (mmol/h)[d] Iso-Alkenes	TON[e]	TOF (h^{-1})[f]
					2	3	4	5				
1[g]	KRh@MFI-Cal-4000NMP	93.7	93.9 (93.8)	760	88.0	0	1.5	4.3	1.80	0.08	2374	1251
2[h]	KRh@MFI-Cal-4000NMP	98.3	94.1 (93.9)	715	92.4	0	1.5	4.3	1.80	0.08	2528	1251
3[g]	KRh@MFI-Cal-500MP	99.4	94.7 (94.1)	160	94.2	0	0.9	4.4	2.93	0.13	2530	1870
4[h]	KRh@MFI-Cal-500MP	99.5	95.2 (94.5)	148	94.7	0	0.9	4.0	2.93	0.13	2556	1870

[a] Reaction conditions: 4 mmol LAO, 80 mg catalyst (0.00152 mmol Rh), 80 mg isooctane (internal standard), all liquid components were dissolved in toluene to a final volume of 4 mL, 40 bar $CO/H_2/Ar$ (45/45/10 vol%), 80 °C, 800 rpm.

[b] Total aldehyde selectivity (L = Linear aldehyde selectivity).

[c] Ratio of the linear aldehyde to the branched aldehyde.

[d] Reaction rate for linear aldehyde formation and reaction rate for isomerized alkenes formation, mmol/h, calculated when LAO conversion is < 20%.

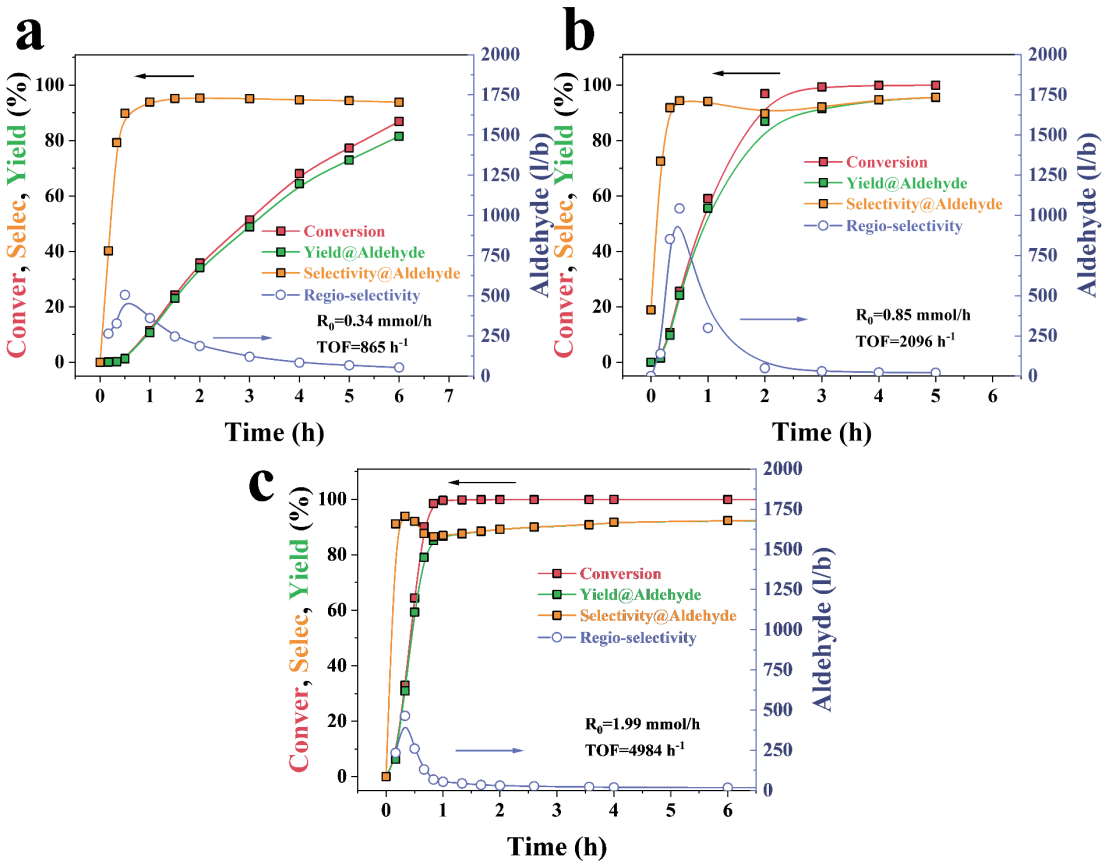
[e] mmol of linear aldehyde/total mmol of Rh at 5 or 9h reaction time.

[f] Rate for the formation of linear aldehyde/total mmol of Rh.

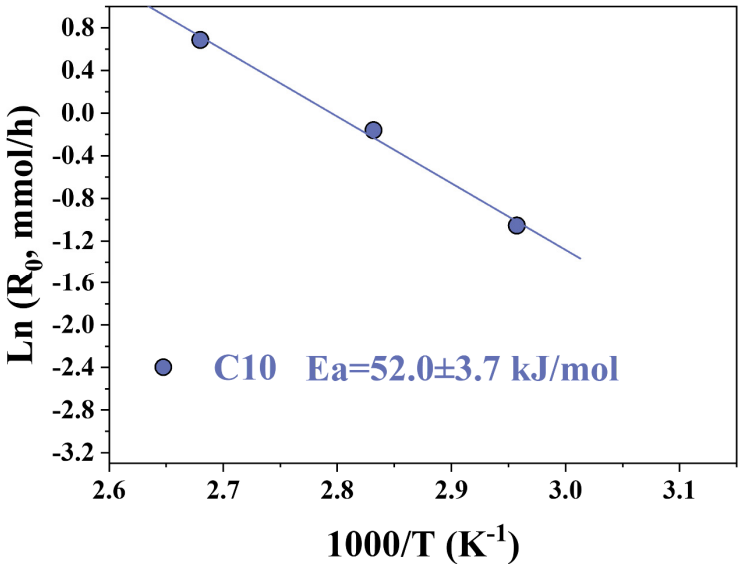
[g] 5h reaction.

[h] 9h reaction.

2.26. Apparent activation energy of KRh@MFI-Cal catalyst for 1-decene hydroformylation

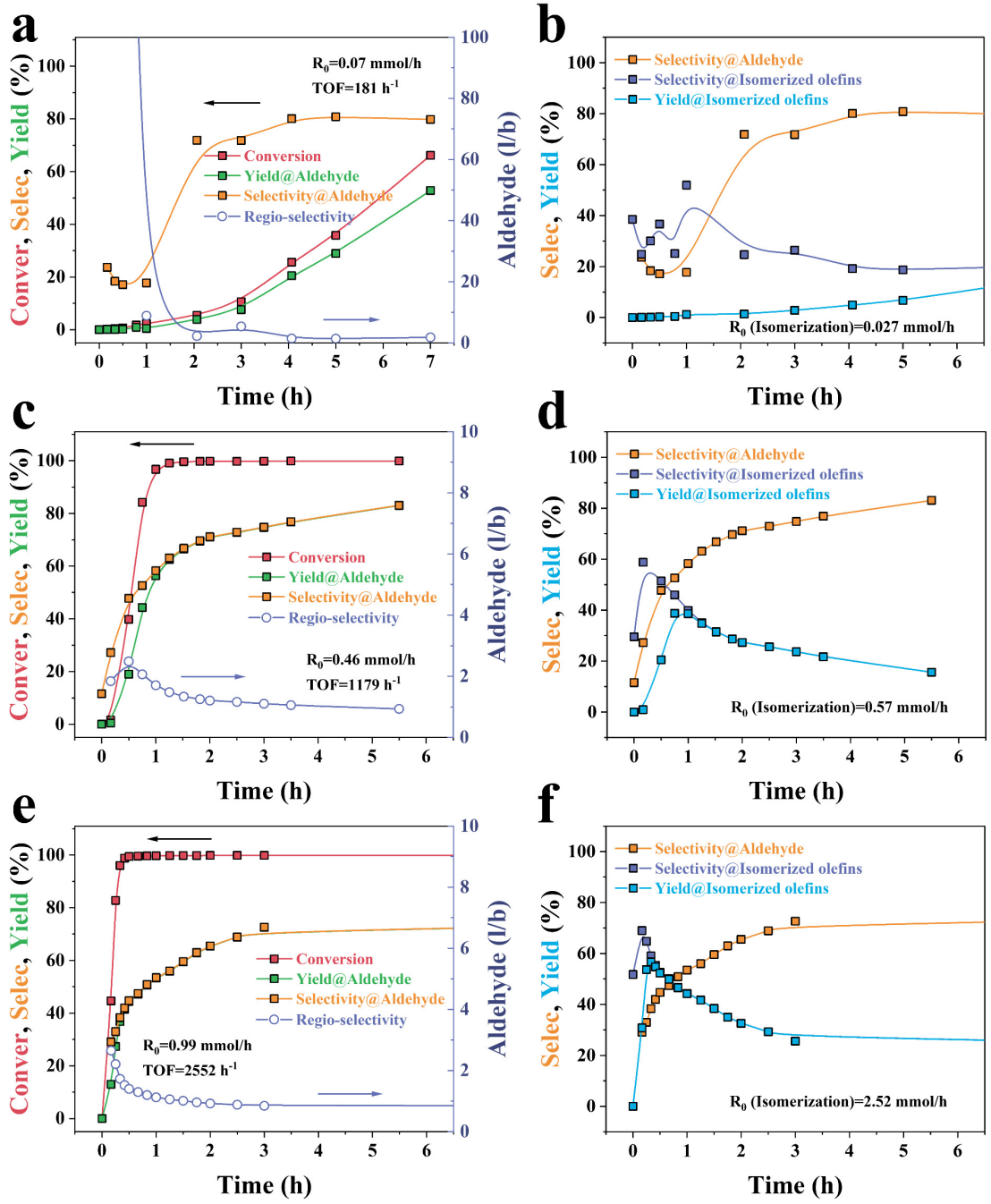


Supplementary Fig. 49. 1-Decene hydroformylation activity of KRh@MFI-Cal catalyst under different reaction temperature. (a) 65 ºC, (b) 80 ºC and (c) 100 ºC (1-Decene conversion, aldehyde yield, aldehyde selectivity and regioselectivity). Reaction condition: 1 mmol LAO, 20 mg catalyst (0.00038 mmol Rh), 20 mg isooctane (internal standard), 4 mL toluene, 40 bar $CO/H_2/Ar$ (45/45/10 vol%), 65-100 ºC, 800 rpm, R_0, TOF and TON are values for linear aldehyde formation.

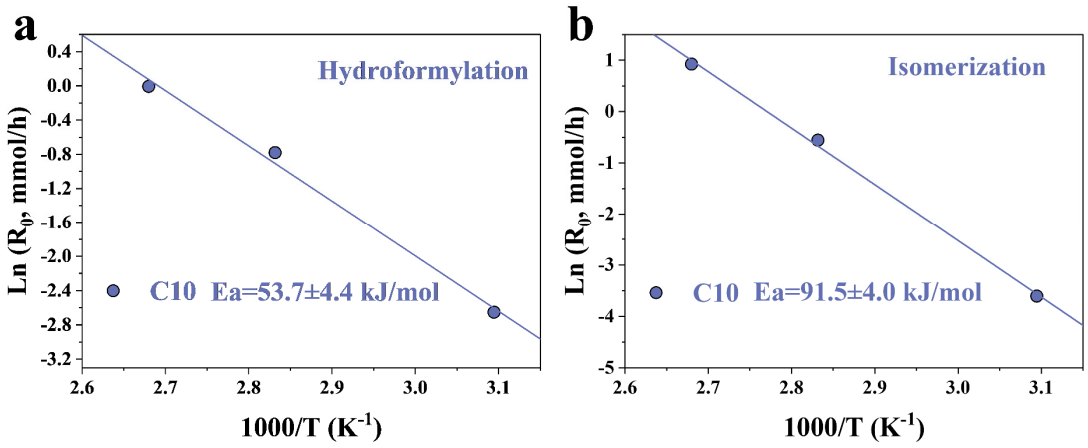


Supplementary Fig. 50. Kinetics. Apparent activation energy of 1-decene hydroformylation on KRh@MFI-Cal catalyst.

2.27. Apparent activation energy of $RhHCO(PPh_3)_3$ catalyst for 1-decene hydroformylation



Supplementary Fig. 51. 1-Decene hydroformylation activity of $RhHCO(PPh_3)_3$ catalyst under different reaction temperatures. (a, b) 50 °C, (c, d) 80 °C, (e, f) 100 °C (1-hexene conversion, aldehyde yield and selectivity, regioselectivity (l/b), isomerized olefins selectivity and yield). Reaction condition: 1 mmol LAO, 0.36 mg catalyst (0.00038 mmol Rh), 20 mg isooctane (internal standard), 4 mL toluene, 40 bar $CO/H_2/Ar$ (45/45/10 vol%), 50-100 °C, 800 rpm, R_0, TOF and TON are values for linear aldehyde formation.



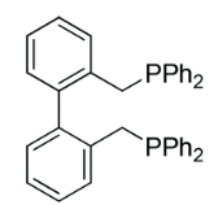
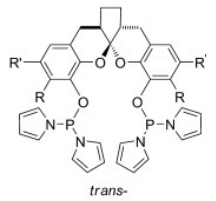
Supplementary Fig. 52. Apparent activation energy of 1-decene. (a) Hydroformylation and (b) isomerization on $RhHCO(PPh_3)_3$ catalyst.

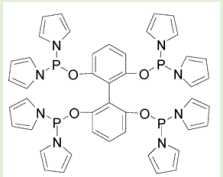
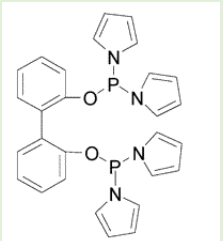
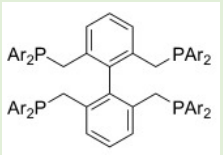
Notes: As shown in Supplementary Fig. 36-39, 45-46, 49-52, the higher apparent activation energy obtained for C8-C10 (56.7 ± 3.5 kJ/mol to 52.0 ± 3.7 kJ/mol) than C6 (38.8 ± 1.2 kJ/mol) on KRh@MFI-Cal catalyst. Further increasing the carbon chain to C10, results in similar values in both the reaction rate and the apparent activation energy than C8. Probably due to the optimal match between the molecular length of C10 and the zig-zag channel dimensions of the MFI zeolite, it brings the reaction performance close to the activity plateau of the different olefins. Besides, the apparent activation energy obtained for C6 and C10 on homogeneous $RhHCO(PPh_3)_3$ Wilkinson catalyst are similar (e.g., C6: 53.2 ± 4.4 kJ/mol for linear aldehyde formation and 94.2 ± 7.8 kJ/mol for isomerization, C10: 53.7 ± 4.4 kJ/mol for linear aldehyde formation and 91.5 ± 4.0 kJ/mol for isomerization). This observation underscores the pronounced influence of zeolite confinement on the heat of alkenes adsorption, which in turn modulates the apparent activation energy observed over the KRh@MFI-Cal catalyst.

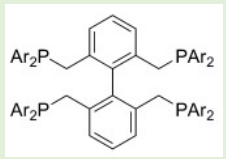
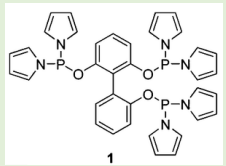
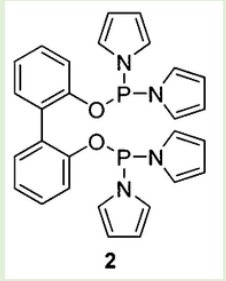
Supplementary Table 13. Comparison with other catalysts. State-of-the art Rh catalyst for LAO (C6-C10) hydroformylation.

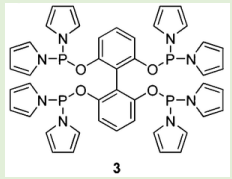
Entry	Catalyst	LAO	Temp. (°C)	Pressure (bar)	Conver. (%)	Selec. (%) aldehydes	Selec. (%) l-aldehyde	l/b ratio of aldehydes	TOF (h^{-1})	Ea (kJ/mol)	Ref
1	KRh@MFI-Cal	C6	80	40	99.5	90.9	85.1	15	872[a]	38.8±1.7	This work
2	KRh@MFI-Cal-500 MP	C6	80	40	99.6	92.8	92.0	112	394[a]	39.0±1.2	This work
3	KRh@MFI-Cal-4000 NMP	C6	80	40	93.8	92.7	92.2	197	469[a]		This work
4	KRh@MFI-Cal-MP as solvent	C6	80	40	98.1	92.6	92.4	428	302		This work
5	Rh-MFI-nano	C6	80	40	96.4	92.1	89.4	32.8	NA		[17]
6	Rh@S-1 zeolite	C6	100	50	99.7	95.5	42.1	0.79	1725[b]		[18]
7	Rh@Hollow S-1 zeolite	C6	100	50	>99	96.0	40.8	0.74	3461[b]		[18]
8	Rh@S-1	C6	85	50	99	100	44.4	0.8	5229	163	[19]
9	K_7^Rh@S-1	C6	85	50	99	100	66.7	2.0	2679[b]	60	[19]
	Rh@S-1-350	C6	85	40	NA	100	52.4	1.1	287		[20]
10	RhC_x@S-1-400	C6	85	40	96	99	54	1.2	1428		[20]
11	Rh_1@S-1	C6	80	40	87.8	45.6	35.7	3.6	NA		[21]
12	Rh_1@S-1	C6	100	40	100	83.5	31.3	0.6	NA		[21]
13	1% Rh@C	C6	60	40	63	72	48.2	2.03	308		[22]
14	1% Rh_2P@C	C6	60	40	96	94	63.0	2.03	563[b]		[22]
15	1% Rh-PPh_3@C	C6	60	40	100	83	45.6	1.22	353[b]		[22]
16	0.5wt% Rh/C	C6	130	30	94.5	44	16.5	0.6			[22]

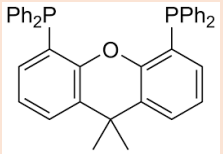
17	Rh_1Co SAA/N-C	C6	100	40	99	95	61.1	1.8	1759	23.8	[23]
18	CoRhHT-1	C6	100	50	99	81	70.0	6.36	5.6[b]		[24]
19	PEG_{4000}-Rh NPs	C6	120	60	100	99	44	0.8			[25]
20	Rh(0) NPs	C6	100	50	100	>99	63.6	1.8			[26]
	RhZn/SBA-15	C6	100	30				-	1341[b]		[27]
21	Rh/RGO	C6	70	50	100	95	49.8	1.1			[28]
22	1% Rh@NaX	C6	100	50	100	>90	38.0	0.73	3047	33.7	[29]
23	PPh_3-1%Rh@NaX	C6	100	50	100	97.5	70.3	2.59	6588		[29]
24	Rh@Y	C6	60	60	99	100	58.3	1.4		60.6	[30]
25	Rh/AC-80	C6	70	50	~85	~68	47.4	~2.3			[31]
26	PPh_3-Rh_{AC-SA}/N-C	C6	100	40	95	96.8	69.9	2.6	6599		[32]
27	Xantphos doped Rh/POPs-PPh_3	C6	100	10	34	88	76.6	6.7	340[b]		[33]
	Rh/SiO_2	C6	100	10		6.9	3.6	1.1	21		[34]
	PPh_3-Rh/SiO_2	C6	100	10		83.5	63.1	3.1	1011		[34]
	$RhHCO(PPh_3)_3$ (Homogeneous)	C6	100	10		87.1	66.4	3.2	1658		[34]
28	$RhHCO(PPh_3)_3$ (Homogeneous)7h	C6	50	40	69.6	82.8	52.1	1.7	180[a]	53.2±4.4	This work
29	$RhHCO(PPh_3)_3$ (Homogeneous)4h	C6	80	40	99.8	86.1	40.8	0.9	1274[a]	53.2±4.4	This work
30	$RhHCO(PPh_3)_3$ (Homogeneous)3h	C6	100	40	99.7	81.0	38.4	0.9	2465[a]	53.2±4.4	This work
31	$RhHCO(PPh_3)_3$	C6	100	40	98.8	98.8	71.0	2.55	2467		[35]

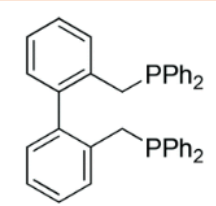
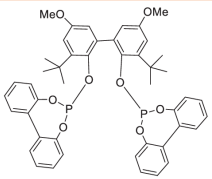
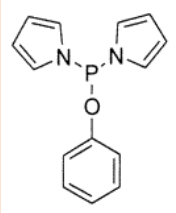
	(Homogeneous)										
32	$RhCl(PPh_3)_3$ (Homogeneous)	C6	60	40	82	67	46.9	2.33	33[b]		[22]
33	$RhCl(PPh_3)_3$ (Homogeneous)	C6	80	40	100	88	41.4	0.89	109[b]		[22]
34	$RhCl(PPh_3)_3$ (Homogeneous)	C6	100	40	95	95	38.8	0.69	674[b]		[22]
	Rh/BISBI (Homogeneous) 	C6	34	6	-	-		66.5	29.4		[36]
	(Homogeneous) R=H, R'=Cl 	C6	100	40	-	82.0	81.5	174.4			[37]
	(Homogeneous) Tetraphosphorus	C6	80	20	-	81.3	81.1	382			[38]

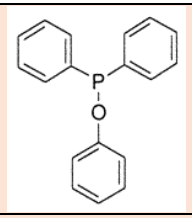
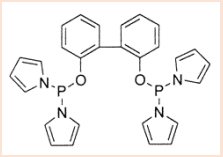
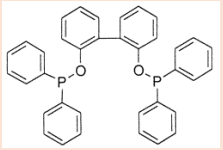
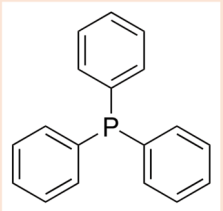
	 Tetraphosphorus ligand **1**										
	(Homogeneous) Bisphosphorus  Bisphosphorus Ligand **2**	C6	80	20	-	87.8	86.7	80.8			[38]
	(Homogeneous) Ar=Ph 	C6	100	20	-	93.4	91.5	48.6	3300		[39]
	(Homogeneous) Ar=3, 5-difluorophenyl	C6	100	20	-	95.8	95.0	125.9	5700		[39]

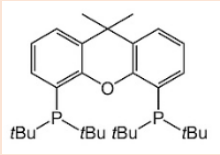
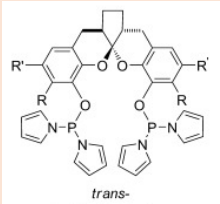
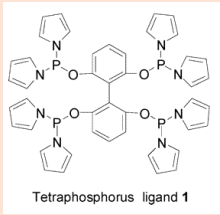
											
	(Homogeneous) Triphosphoramidite 	C6	80	10	-	77.7	77.5	471			[40]
	(Homogeneous) Bis-phosphoramidite 	C6	80	10	-	85.8	85.1	125			[40]
	(Homogeneous) Tetra-phosphoramidite	C6	80	10	-	75.5	75.4	618			[40]

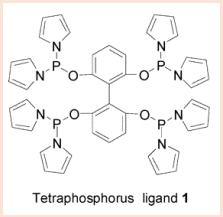
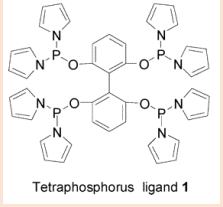
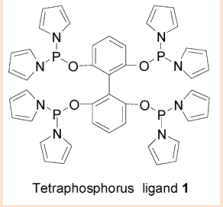
	 3										
Entry	**Catalyst**	**LAO**	**Temp. (°C)**	**Pressure (bar)**	**Conver. (%)**	**Selec. (%) aldehyde**	**Selec. (%) l-aldehyde**	**l/b of aldehyde**	**TOF (h^{-1})**	**Ea (kJ/mol)**	**Ref**
35	KRh@MFI-Cal	C8	80	40	97.9	84.8	81.0	21.7	1979	56.7±3.5	This work
36	KRh@MFI-Cal-500 MP	C8	80	40	96.0	84.2	83.2	82.0	1919		This work
37	KRh@MFI-Cal-4000 NMP	C8	80	40	97.9	85.0	84.8	352	1136		This work
38	KRh@MFI-Cal-MP as solvent	C8	80	40	92.8	82.8	82.6	462	419		This work
39	Rh/S1-OH	C8	110	30	82.3	97.8	38.5	0.65	NA		[41]
40	Rh_2O_3@S-1	C8	80	50	98.1	97.1	49.7	1.05			[42]
41	Rh_2O_3@S-1-II	C8	80	50	97.7	94.2	59.4	1.71			[42]
42	RhC_x@S-1-400	C8	85	40	95	100	50	1.0	NA		[20]
43	Rh@Y	C8	60	60	99	100	52.8	1.12			[30]
44	Rh_1Co SAA/N-C	C8	100	40	94	88	56.6	1.8	1542		[23]
45	Xantphos doped Rh/POPs-PPh_3	C8	100	10	42	87	78.3	9.0	NA		[33]
46	Rh/POPs-PPh_3	C8	100	10	98	46	20.6	0.81	NA		[33]
47	PVP-capped Rh NSs	C8	90	50	90	82.2	41.1	1.0	NA		[43]

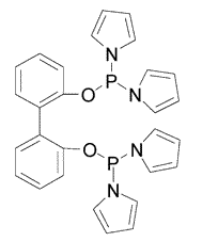
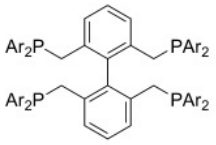
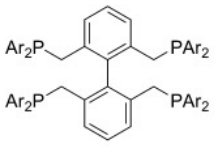
48	CoRhHT-1	C8	100	50	98	96	34.9	0.57	5.5[b]		[24]
49	PEG_{4000}-Rh NPs	C8	120	60	100	99	40.8	0.7			[25]
50	Rh(0) NPs	C8	100	50	100	>99	62.3	1.7			[26]
51	PPh_3-Rh_{AC-SA}/N-C	C8	100	40	66	95.5	67.4	2.4	4324		[32]
52	Rh/POL-PPh_3	C8	90	20	99.4	92.1	42.8	0.87			[44]
53	Rh/POL-dppe	C8	90	20	96.9	99.3	70.6	2.46	NA		[45]
54	Rh/PSA-PPh_3	C8	100	20	96.3	98.4	72.5	2.8	NA		[46]
55	Rh/PSA-Xantphos	C8	120	20	94.7	98.0	95.6	39	NA		[46]
56	Rh@POP-PTBA-HA-50	C8	120	60	87.2	96.3	88.6	11.5	801[b]		[47]
57	Rh-30PTA@MIL-101 (Cr)	C8	70	40	98	89	39.6	0.8	NA		[48]
58	BISBI/Rh=2.3 $Rh(acac)(CO)_2$ (Homogeneous)	C8	95	21	94	76	50.7	2			[49]
59	$RhHCO(PPh_3)_3$ (Homogeneous)	C8	100	40	98.8	98.2	69.5	2.42	1391		[35]
60	$Rh(CO)_2(acac)$ (Homogeneous)	C8	90	20	98.8	50.1	25.9	1.07	NA		[45]
	Rh/Xantphos (Homogeneous) 	C8	80	10		97.7	95.9	53.5	800		[50]

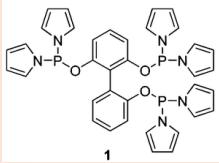
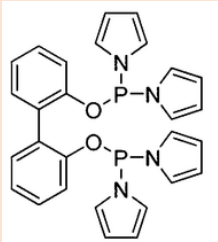
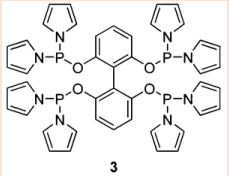
	Rh/BISBI (Homogeneous) 	C8	80	10		89.6	88.5	80.5	850		[50]
61	Rh/BIPHEPHOS (Homogeneous) 	C8	80	20	31	82	80.4	>50	3600		[51]
62	(Homogeneous) 	C8	80	20	35	61	46.1	3.1	10000		[52]
63	(Homogeneous)	C8	80	20	35	68	47.4	2.3	219		[52]

											
64	(Homogeneous) 	C8	80	20	33	86	85.2	107	10000		[52]
65	(Homogeneous) 	C8	80	20	24	80	66.7	5	424		[52]
66	(Homogeneous) PPh_3 	C8	80	10	98	91	65.7	2.6			[53]
67	(Homogeneous) *t*-Bu-XANTPHOS	C8	80	10	31	98	96.0	49			[53]

											
68	(Homogeneous) 	C8	80	10	96	92	88.3	24			[53]
	(Homogeneous) R=H, R'=Cl 	C8	100	40	-	77.4	76.1	58.2			[37]
	(Homogeneous) Tetraphosphorus 	C8	80	20	-	84.7	84.5	372			[38]
	(Homogeneous)	C8	80	10	-	71.7	71.5	405			[38]

	Tetraphosphorus 										
	(Homogeneous) Tetraphosphorus 	C8	80	60	-	92	91.6	242			[38]
	(Homogeneous) Tetraphosphorus 	C8	40	20	-	96.1	95.9	461			[38]
	(Homogeneous) Bisphosphorus	C8	80	20	-	90	88.8	74.1			[38]

	 Bisphosphorus Ligand **2**										
	(Homogeneous) Ar=Ph 	C8	100	20	-	94.4	92.6	50.5	2500		[39]
	(Homogeneous) Ar=3, 5-difluorophenyl 	C8	100	20	-	95.1	93.9	77.9	7400		[39]
	(Homogeneous) Triphosphoramidite	C8	80	10	-	79.4	79.2	415			[40]

	 1										
	(Homogeneous) Bis-phosphoramidite  2	C8	80	10	-	87.8	87.1	117			[40]
	(Homogeneous) Tetra-phosphoramidite  3	C8	80	10	-	77.8	77.7	559			[40]
Entry	**Catalyst**	**LAO**	**Temp. (°C)**	**Pressure (bar)**	**Conver. (%)**	**Selec. (%) aldehyde**	**Selec. (%) l-aldehyde**	**l/b of aldehyde**	**TOF (h^{-1})**	**Ea (kJ/mol)**	**Ref**
69	KRh@MFI-Cal	C10	80	40	99.4	92.1	89.2	30	2096	52.0±3.7	This work
70	KRh@MFI-Cal-	C10	80	40	98.5	96.8	96.5	378	2052		This work

	500 MP										
71	KRh@MFI-Cal-4000NMP	C10	80	40	99.8	95.9	95.8	817	1706		This work
72	KRh@MFI-Cal-MP as solvent	C10	80	40	93.6	95.7	95.6	655	761		This work
73*	KRh@MFI-Cal-4000NMP-1 mol/L	C10	80	40	93.7	93.9	93.8	760	1251		This work
74	Rh-MFI-100-H_2	C10	80	40	89.9	83.9	47.4	1.3	~1700[a]		[17]
75	0.6K-Rh-MFI-100-H_2	C10	80	40	97.4	61.0	46.5	3.2	NA		[17]
76	1.2K-Rh-MFI-100-H_2	C10	80	40	84.5	76.3	71.4	14.5	~1000[a]		[17]
77	1.6K-Rh-MFI-100-H_2	C10	80	40	35.6	84.7	80.5	19.1	NA		[17]
78	2.2K-Rh-MFI-100-H_2	C10	80	40	24.6	89.3	86.6	32.3	~800[a]		[17]
79	Rh-MFI-nano	C10	80	40	>99	89.9	88.1	47.6	~4500[a]		[17]
80	Rh_2O_3@S-1-II	C10	80	50	96.1	95.5	61.3	1.79			[42]
81	Rh_2O_3@S-1-II	C10	80	50	99.3	93.6	81.4	6.65			[42]
82	RhC_x@S-1-400	C10	85	40	49	99	72.2	2.7	NA		[20]
83	Rh@Y	C10	60	60	96	97	52.1	1.16			[30]
84	Rh_1Co SAA/N-C	C10	100	40	70	88	52.8	1.5	1141		[23]
85	PEG_{4000}-Rh NPs	C10	130	60	100	99	44	0.8			[25]
86	CoRhHT-1	C10	100	50	99	96	65.0	2.10	5.6[b]		[24]
87	Rh-Co-Pi/ZnO	C10	100	40	>95	81	54.9	2.1			[54]

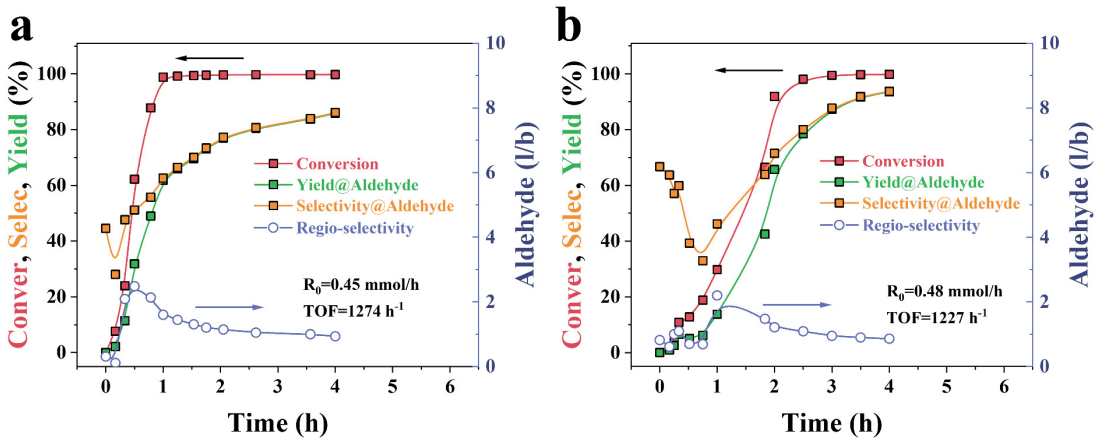
88	Rh(0) NPs	C10	100	50	100	>99	59.4	1.5			[26]
89	$RhHCO(PPh_3)_3$ (Homogeneous)7h	C10	50	40	66.2	80	51.4	1.8	181[a]	53.7±4.4	This work
90	$RhHCO(PPh_3)_3$ (Homogeneous)3h	C10	80	40	99.8	74.8	39.2	1.1	1179[a]	53.7±4.4	This work
91	$RhHCO(PPh_3)_3$ (Homogeneous)3h	C10	100	40	99.9	72.6	32.3	0.8	2552[a]	53.7±4.4	This work
	$RhHCO(PPh_3)_3$ (Homogeneous)	C10	60	27.2	NA	NA	NA	NA	NA	49.2	[55]
92	$RhHCO(PPh_3)_3$ (Homogeneous)	C10	100	40	98.2	92.2	53.1	1.36	961		[35]

[a] Rate for the formation of linear aldehyde/total mmol of Rh.

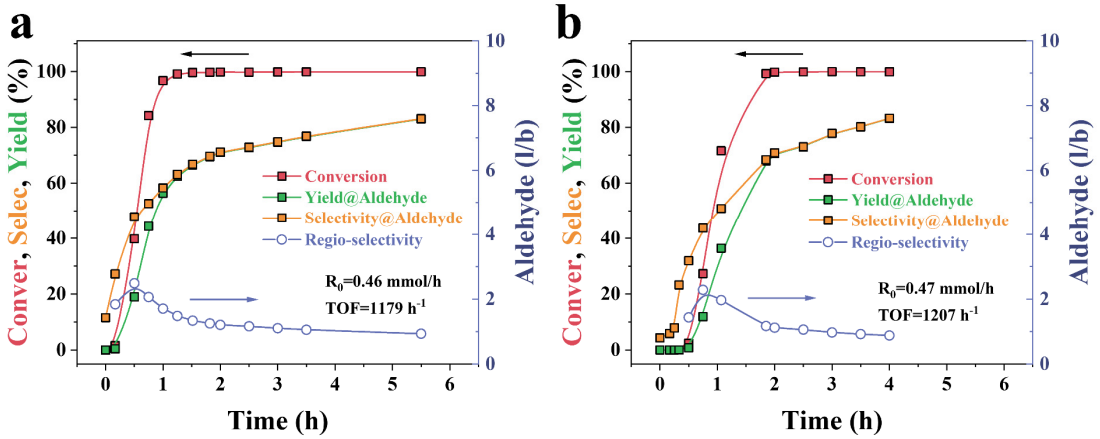
[b] Rate for the formation of (linear + branch aldehyde)/total mmol of Rh.

3. Appendix

3.1. Compare $RhHCO(PPh_3)_3$ and $RhCl(PPh_3)_3$ catalyst



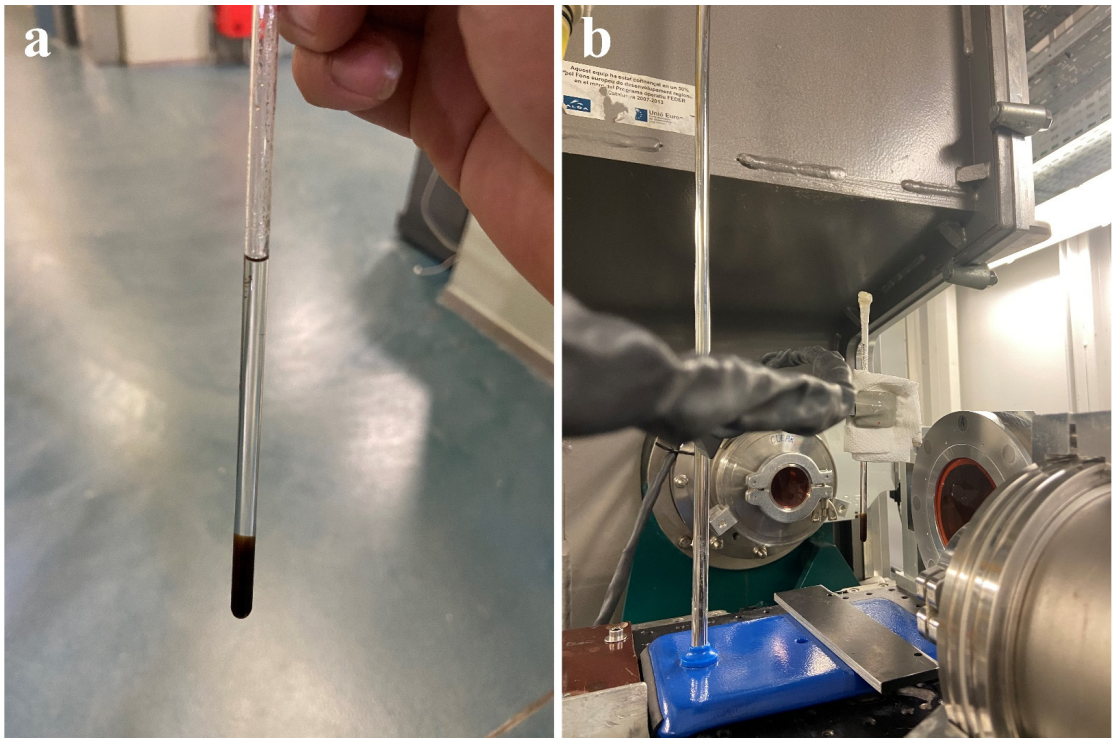
Supplementary Fig. 53. 1-Hexene hydroformylation activity. (a) $RhHCO(PPh_3)_3$ and (b) $RhCl(PPh_3)_3$ catalysts (1-hexene conversion, aldehyde yield, aldehyde selectivity and regioselectivity). Reaction condition: 1 mmol LAO, 0.36 mg catalyst (0.00038 mmol Rh), 20 mg decane (internal standard), 4 mL toluene, 40 bar $CO/H_2/Ar$ (45/45/10 vol%), 80 °C, 800 rpm, R_0, TOF and TON are values for linear aldehyde formation.



Supplementary Fig. 54. 1-Decene hydroformylation activity. (a) $RhHCO(PPh_3)_3$ and (b) $RhCl(PPh_3)_3$ catalysts (1-decene conversion, aldehyde yield, aldehyde selectivity and regioselectivity). Reaction condition: 1 mmol LAO, 0.36 mg catalyst (0.00038 mmol Rh), 20 mg decane (internal standard), 4 mL toluene, 40 bar $CO/H_2/Ar$ (45/45/10 vol%), 80 °C, 800 rpm, R_0, TOF and TON are values for linear aldehyde formation.

Notes: It is clearly observed an induction period on $RhCl(PPh_3)_3$ catalyst for hydroformylation due to the formation of $RhHCO(PPh_3)_3$ active centres during reaction. The final reaction rate, aldehyde selectivity, yield and l/b ratio are similar, thus we use $RhHCO(PPh_3)_3$ as Wilkinson's catalyst for comparison in this work.

3.2. XAS Analysis



Supplementary Fig. 55. XAS measurement. Demonstration of *ex-situ* XAS measurement in CLÆSS 22 beamline of the ALBA synchrotron (Spain).

Notes: To obtain reliable X-ray absorption spectroscopy (XAS) data of KRh@MFI-Cal, KRh@MFI-Cal-CO/H_2 and KRh@MFI-Cal with MP organic additive after the hydroformylation reaction, it is critical to prevent catalysts exposure to air, as rhodium species are highly sensitive to oxidation. Any contact with oxygen could alter their oxidation state or coordination environment, thereby compromising the accuracy of post-reaction structural characterization.

Therefore, following a standard 1-hexene hydroformylation reaction, the batch reactor was transferred into an inert glovebox atmosphere. Inside the glovebox, the reactor was opened, and the solid catalyst together with the remaining liquid phase was carefully transferred into a liquid NMR analysis tube. The tube was immediately sealed to ensure an airtight environment (Supplementary Fig. 55a). Subsequent XAS analysis was performed under inert conditions to preserve and capture the authentic post-reaction state of the catalyst, as shown in Supplementary Fig. 55b.

3.3. Quantification of Rh^{3+}/Rh^{+} species ratio based on IR-CO

Quantifications of Rh^{+} and Rh^{3+} species, requires determination of IR extinction coefficients for Rh^{+}-$(CO)_2$ and Rh^{3+}-(CO) IR bands. We did a semi-quantitative estimation correlating the intensity of the Rh^{+}-$(CO)_2$ and Rh^{3+}-(CO) IR bands with the Rh loading of pre-selected reference compounds, assuming that all Rh of our compound is interacting with CO and that the IR spectra correspond to maxima CO surface coverage.

The experimental procedure used is detailed below:

The Beer-Lambert Law is usually used to estimate the extinction coefficient (ε)[56]:

$$n = \frac{A \cdot S}{\varepsilon \cdot m}$$

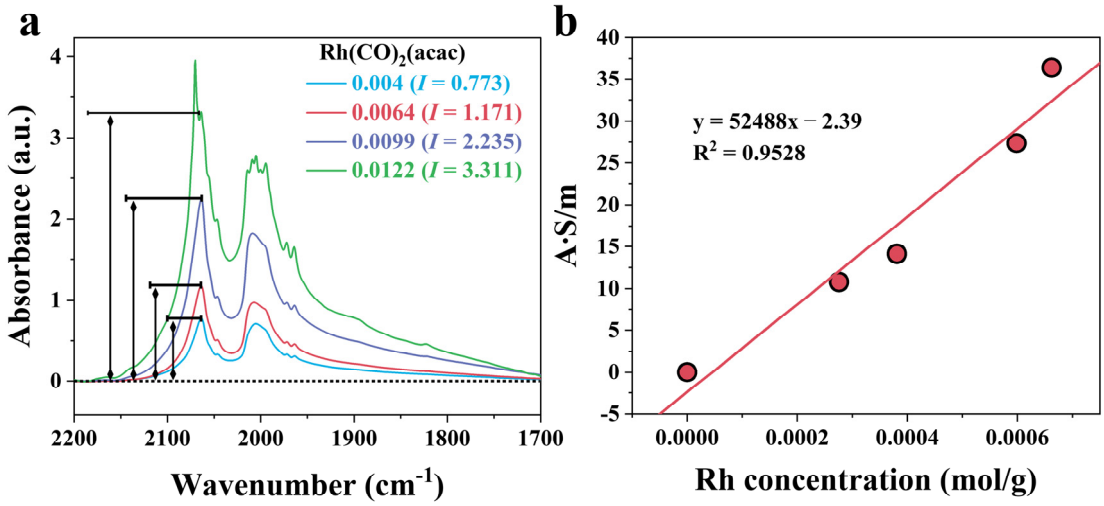
Where n stands for the Rh concentration (mol/g); A is the integrated absorbance area (cm^{-1}) or absorbance intensity (a.u.); S represents the surface area of pellets (cm^2); ε is the extinction coefficient (cm/mol); and m stands for the weight of pellet (g).

For the case of Rh^{+} we used different amounts of $Rh(CO)_2$(acac) (Sigma-Aldrich, 98% purity) mixed with KBr and pressed into 10 mm diameter pellets. In the calculations, we used the intensity of the peak at 2064 cm^{-1} corresponding to the ν_{as} vibration of the di-carbonyl specie interacting with Rh^{+}.

The corresponding data are included in Supplementary Table 14 and plotted in Supplementary Fig. 56.

Supplementary Table 14. Calibration of Rh^{+} concentration. Rh^{+} $(CO)_2$ peak intensity and correlation with Rh^{+} amount.

Samples $Rh(CO)_2$(acac) weight (g)	KBr weight (g)	(m) Pellet weight (g)	Rh concentration ($\times 10^{-3}$ mol/g)	(A) IR $Rh^{+}(CO)_2$ intensity (2064 cm^{-1})	(S) Pellet surface area (cm^2)	A·S/m
0.0040	0.0522	0.0562	0.2758	0.773	0.785	10.80
0.0064	0.0587	0.0651	0.3810	1.171	0.785	14.12
0.0099	0.0542	0.0641	0.5985	2.235	0.785	27.37
0.0122	0.0592	0.0714	0.6622	3.311	0.785	36.40



Supplementary Fig. 56. Calibration of Rh^+ concentration. (a) IR peak of CO corresponding to different amount $Rh(CO)_2(acac)$ mixed KBr samples, (b) correlation of Rh^+ molar concentration and IR $Rh^+(CO)_2$ intensity.

In the case of Rh^{3+}, there are no commercial salts containing CO ligands which can be used as reference, which complicates the analysis of extinction coefficients.

In our previously publication[13], we reported a low-temperature IR-CO protocol for the identification of Rh^{3+} species, involving sample evacuation at 80 ºC followed by CO titration at low temperature of −65 ºC. Rh^{3+} has a weak interaction with CO and is easily reduced to Rh^{+} at increasing CO coverages. Therefore to operate at low temperature is mandatory for a realistic quantification of Rh^{3+} species.

Two KRh@MFI calcined samples with different Rh loadings were prepared: 0.05KRh@MFI-Cal (0.05wt% Rh), and 0.2KRh@MFI-Cal (0.2wt% Rh). Considering that the Rh clusters size is approximately 0.4 nm, corresponding to about 2-3 Rh atoms, the Rh dispersion is close to 100%, and all Rh atoms are accessible to CO.

The IR spectra were acquired at −65 ºC at increasing CO coverage (from 0.16 to 10 mbar) until saturation. At this condition, we assume that all Rh species are interacting with CO, and from curve-fitting of the IR spectra we can determine the peak area of the IR band corresponding to Rh^{3+} at 2137 cm^{-1} (see Supplementary Fig. 57)[13]. Due to the coexistence of a small peak at 2120 cm^{-1} attributed to Rh^{2+}, we have considered both peak areas to define the adsorption coefficient of oxidise Rh^{n+} species (See Supplementary Fig. 57c and d). The inclusion or not of the peak area of Rh^{2+}, results in final errors of ± 30% when calculating the Rh^{3+}/Rh^{+} ratio.

The corresponding data are included in Supplementary Table 15 and 16 and plotted in Supplementary Fig. 57.

Supplementary Table 15. Calibration of Rh^{3+} concentration. Calculation of Rh^{3+} extinction coefficient based on KRh@MFI-Cal.

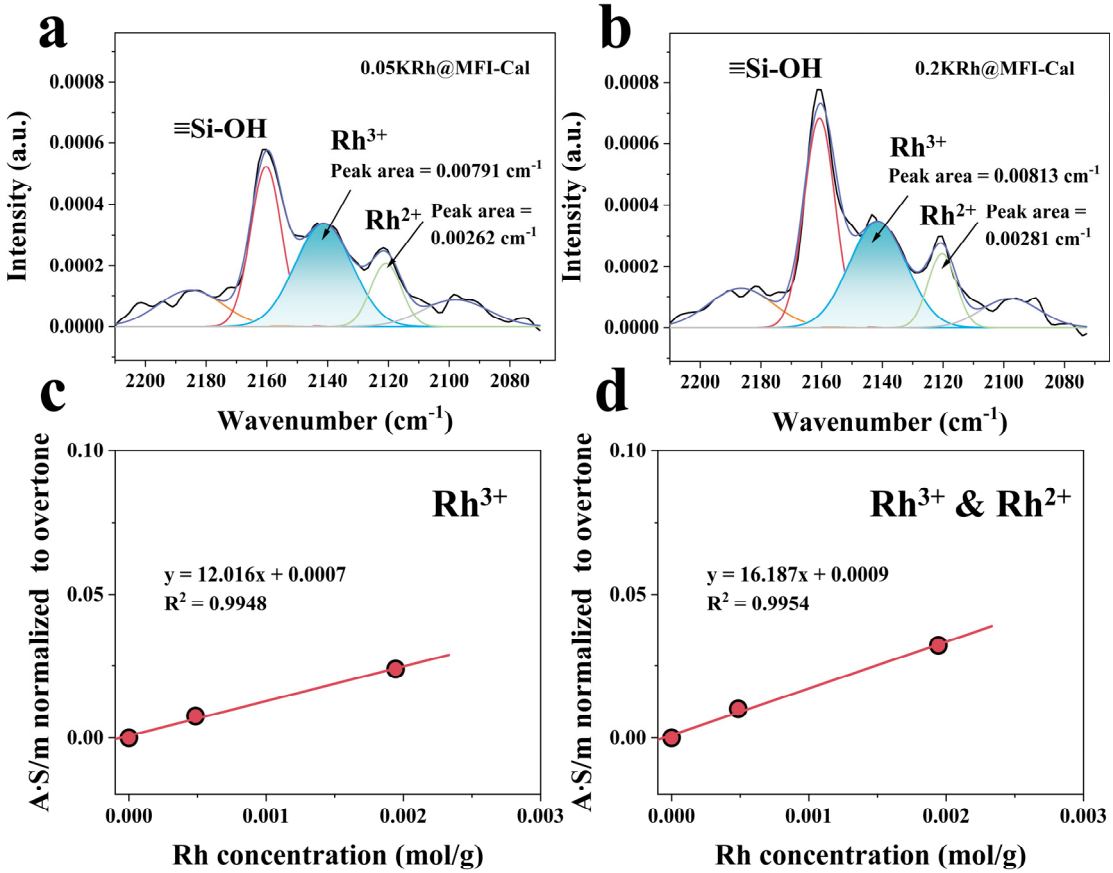
Samples	Rh loading (wt%)	(m) Pellet weight (g)	(S) Pellet surface area (cm^2)	Overtone area	Rh concentration ($\times10^{-3}$ mol/g)	(A) Rh^{3+} peak area ($\times10^{-3}$)	A·S/m normalized to overtone [a]
0.05KRh@MFI-Cal	0.05	0.0163	0.785	50.53	0.486	7.91	0.00754
0.2KRh@MFI-Cal	0.20	0.0089	0.785	30.08	1.943	8.13	0.0238

[a] The A·S/m values were normalized using the SiO_2 overtone band to compensate for variations in sample thickness and IR optical path caused by the heterogeneous nature of powder samples, thereby allowing a more reliable comparison between Rh concentration and peak area.

Supplementary Table 16. Calibration of Rh^{3+} concentration. Calculation of Rh^{3+} & Rh^{2+} extinction coefficient based on KRh@MFI-Cal.

Samples	Rh loading (wt%)	(m) Pellet weight (g)	(S) Pellet surface area (cm^2)	Overtone area	Rh concentration ($\times 10^{-3}$ mol/g)	(A) Rh^{3+} & Rh^{2+} peak area ($\times 10^{-3}$)	A·S/m normalized to overtone [a]
0.05KRh@MFI-Cal	0.05	0.0163	0.785	50.53	0.486	10.53	0.0100
0.2KRh@MFI-Cal	0.20	0.0089	0.785	30.08	1.943	10.94	0.0321

[a] The A·S/m values were normalized using the SiO_2 overtone band to compensate for variations in sample thickness and IR optical path caused by the heterogeneous nature of powder samples, thereby allowing a more reliable comparison between Rh concentration and peak area.

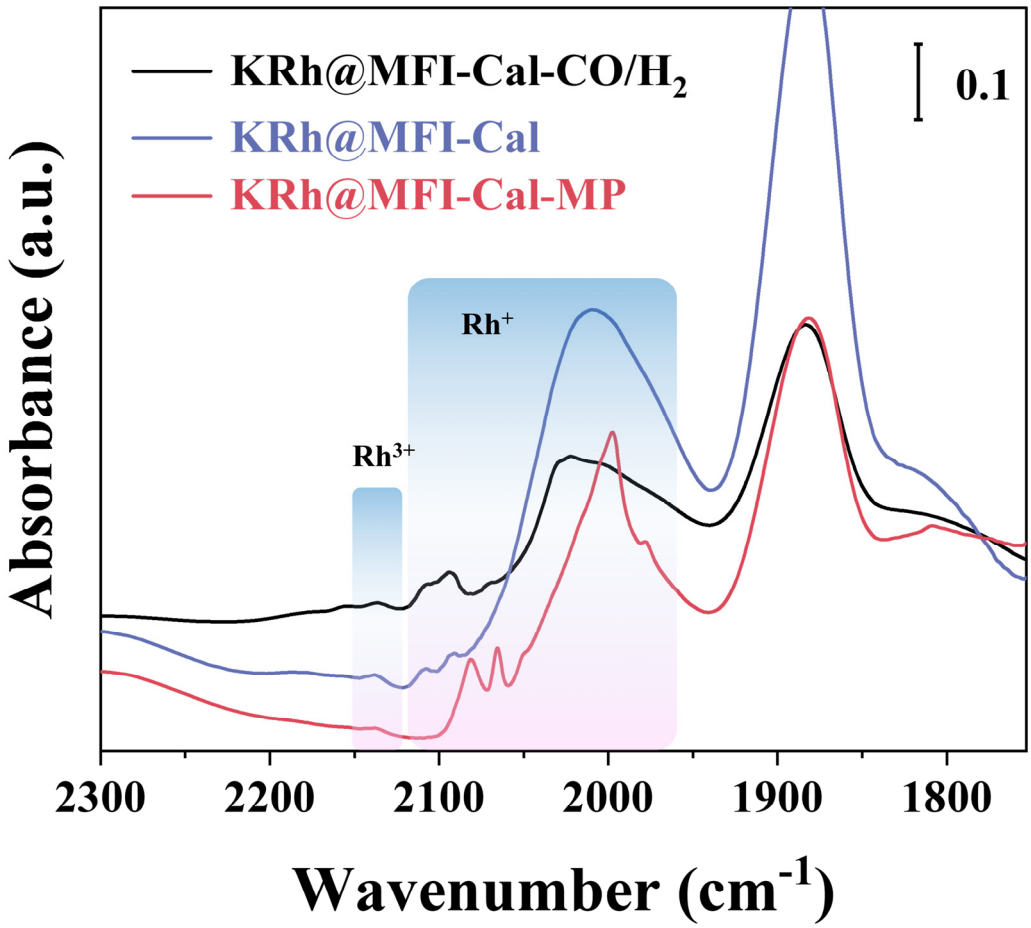


Supplementary Fig. 57. Calibration of Rh^{3+} concentration. (a) Deconvolution of Rh^{3+} and Rh^{2+} species on 0.05KRh@MFI-Cal sample, (b) deconvolution of Rh^{3+} and Rh^{2+} species on 0.2KRh@MFI-Cal sample, (c) correlation Rh concentration and IR normalized Rh^{3+} integrated area. (d) correlation Rh concentration and IR normalized Rh^{3+} plus Rh^{2+} integrated areas.

Based on the above correlations, it is clear that at the same Rh concentration, the peak intensity for $Rh^{+}(CO)_2$ is higher than that for $Rh^{3+}(CO)$. This is reasonable considering the different electronic configuration of both Rh^{3+} and Rh^{+} species. Indeed, Rh^{+} has a d^8 electronic configuration, which enables strong π backdonation to adsorbed CO molecules. Electrons from the Rh d orbitals are donated into the π* antibonding orbitals of CO, significantly altering the dipole moment of the C-O bond and resulting in extremely high infrared absorption intensity. Consequently, even at very low concentrations, the characteristic of $Rh^{+}(CO)_2$ doublet is easily detected in IR spectrum.

In contrast, Rh^{3+} exhibits a d^6 electronic structure with a higher positive charge and much stronger electron binding ability, which largely suppresses π-backdonation to CO. As a result, CO adsorption on Rh^{3+} is dominated by σ-donation from CO to the metal center. In this case, the variation in dipole moment during C-O vibration is low, leading to weak IR absorption intensity of Rh^{3+} carbonyl species.

With these results in hand, we have estimated the relative amount of Rh^{3+} versus Rh^{+} in the KRh@MFI-Cal-CO/H_2 and in others KRh@MFI-Cal catalysts included in our work in Supplementary Fig. 58. This is summarized in Supplementary Table 17.



Supplementary Fig. 58. IR-CO results. IR-CO at −65 ºC and 2 mbar CO coverage spectra for KRh@MFI-Cal-Toluene-CO/H_2, KRh@MFI-Cal after 1-hexene hydroformylation reaction, and KRh@MFI-Cal-500MP after 1-hexene hydroformylation reaction.

Supplementary Table 17. **Quantification results.** Rh^{3+}, Rh^{+} concentrations in KRh@MFI-Cal catalysts system.

Samples	(m) Pellet weight (g)	(S) Pellet surface area (cm^2)	Overtone area	Rh^{3+} peak area	Rh^{+} peak intensity	Rh^{3+} concentration ($\times10^{-3}$ mol/g) [a]	Rh^{+} concentration ($\times10^{-5}$ mol/g)	Rh^{3+}/ Rh^{+} molar ratio [a]
KRh@MFI-Cal (After reaction)	0.0192	0.785	103.69	0.07201	0.01138	1.7 - 2.3	5.4	31.2 - 42.4
KRh@MFI-Cal-500MP (After reaction)	0.0161	0.785	43.363	0.03919	0.06153	2.7 - 3.6	10.3	26.0 - 35.1
KRh@MFI-Cal-CO/H_2	0.0146	0.785	41.072	0.08158	0.02547	6.5 - 8.8	7.2	91.3 - 123.3

[a] The range was determined by taking the equations in Supplementary Fig. 57c and 57d into consideration.

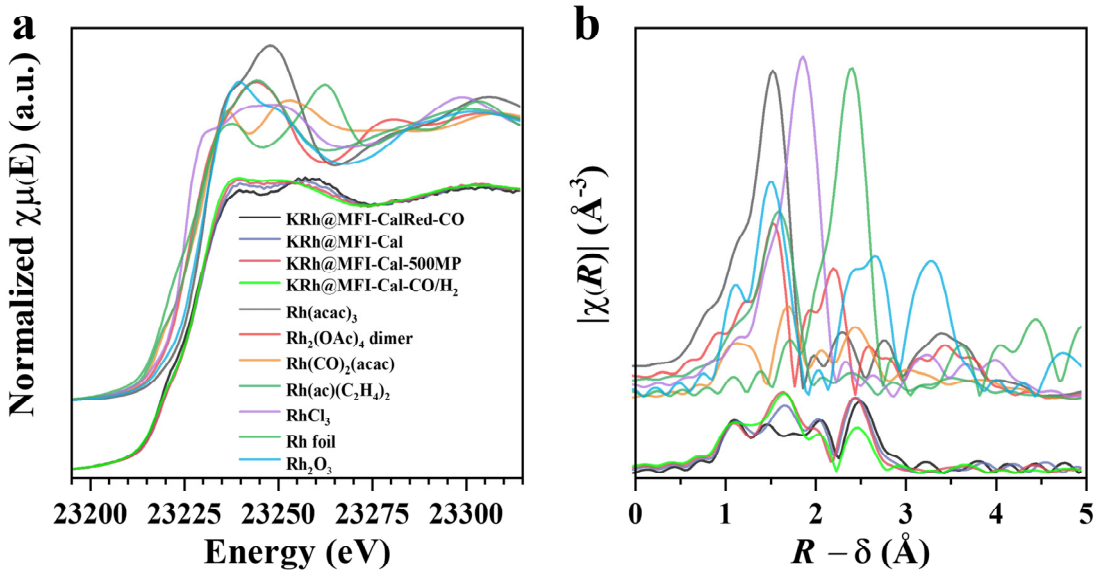
We would like to admit that this calculation method involves uncertainties, primarily due to the lack of a well-defined Rh^{3+} reference system, the potential partial reduction of Rh^{3+} under low-temperature CO titration conditions, the lack of accurate quantification of sites interacting with CO and the absence of a pure Rh^{3+} containing reference sample. Nevertheless, this approach still provides a useful semi-quantitative indication of the relative Rh^{3+}/Rh^{+} molar ratio, offering insight into the predominant Rh species distribution. This IR-CO quantification clearly confirms that Rh^{3+} species are the predominant Rh form in the KRh@MFI-Cal-CO/H_2, KRh@MFI-Cal and KRh@MFI-Cal-MP samples.

3.4. Quantification of Rh^{3+}/Rh^{+} species ratio based on XAS

Herein, Rh_2O_3, $Rh(CO)_2(acac)$, and Rh foil have been identified as the most close references to represent the data set for comparison with KRh@MFI-Cal based catalysts. In particular, the Fourier Transform (FT) of the k^2 weighted EXAFS oscillations was suggesting a high fraction of CO ligand contribution in the samples, but its effect on the XANES region was not discussed.

It is challenging to quantify the Rh oxidation state based on the XAS spectra in the present case. Both linear combinations fitting (LCF) and Multivariate Curve Resolution Analysis (MCR) were attempted (Supplementary Table 18 and 19). While similar trends are obtained by LCF and MCR, the MCR analysis allowed a better reconstruction of the sample spectra (Supplementary Table 19). Indeed, the LCF, even if it allows to represent the already discussed trends, it did not satisfactorily reproduce the experimental spectral features, indicating that the available reference dataset is not fully representative of the local environments present in the samples. Indeed, the quantitative estimation of the Rh^{3+}/Rh^{+} ratio which can be extracted do not agree with the data obtained by CO-FTIR.

The MCR approach was confirming the closeness of the main three components expected in the dataset, allowing at the same time to slightly variate them. Such flexibility is not possible within an LCF approach. The analysis converged in two components exactly overlapping with Rh metal (Rh^0) and Rh_2O_3 (Rh^{3+}) reference spectra, and a third component which slightly differs from $Rh(CO)_2(acac)$. Such contribution seems to corresponds to $Rh^{\delta+}$ oxidation state, with a local structure similar to the one of the $Rh(CO)_2(acac)$ reference and a slightly different electronic distribution. The quantitative results obtained by these two approaches are reported in Supplementary Table 18 and 19.



Supplementary Fig. 59. XAS analysis. (a) Normalized XANES spectra and (b) k^2-weighted FT of the EXAFS oscillations of KRh@MFI catalysts compared with the full references data set. The FT of Rh foil was scale down by factor 2 for better representation.

Supplementary Table 18. XAS analysis. Results of the Athena-based LCF using Rh_2O_3, $Rh(CO)_2(acac)$, and Rh foil as references. The analysis was carried out over an energy range from −70 to +130 eV.

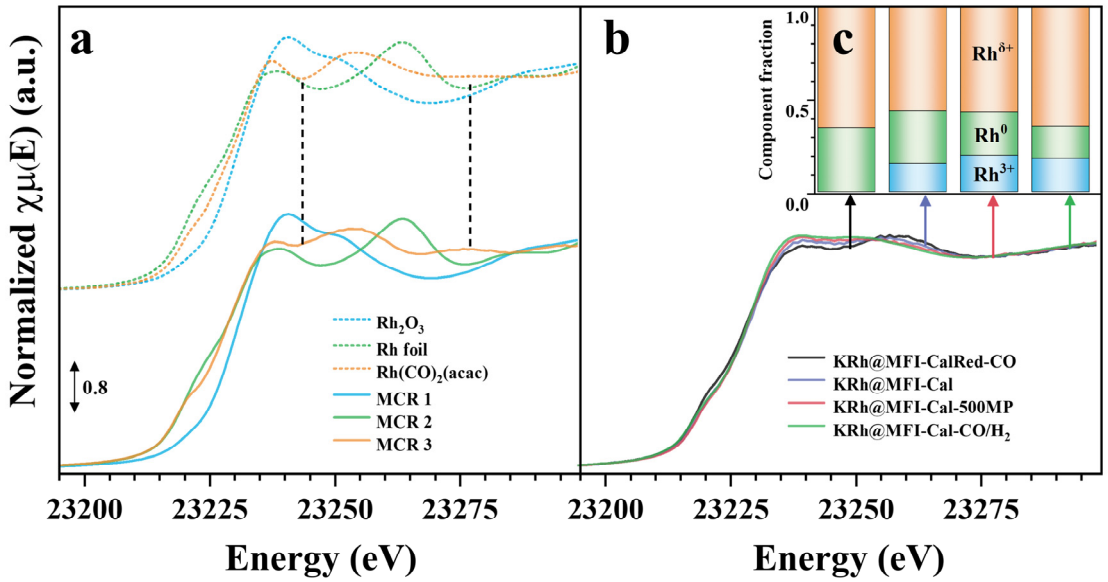
Sample	Rh^0 weight	Rh^+ weight	Rh^{3+} weight	R-factor
KRh@MFI-CalRed-CO	0.355 (0.043)	0.557 (0.039)	0.088 (0.019)	0.0012
KRh@MFI-Cal (After reaction)	0.252 (0.038)	0.541 (0.034)	0.207 (0.017)	0.0009
KRh@MFI-Cal-500MP (After reaction)	0.208 (0.032)	0.536 (0.029)	0.255 (0.014)	0.0006
KRh@MFI-Cal-CO/H_2	0.171 (0.038)	0.577 (0.034)	0.252 (0.017)	0.0009

Supplementary Table 19. XAS analysis. Results of the MCR analysis performed in ProQEXAFS[57]. The analysis was carried out over an energy range from −70 to +130 eV.

Sample	Rh^0 weight	$Rh^{\delta+}$ weight	Rh^{3+} weight	LOF, %*
KRh@MFI-CalRed-CO	0.343	0.657	0.0	0.33
KRh@MFI-Cal (After reaction)	0.283	0.566	0.151	0.07
KRh@MFI-Cal-500MP (After reaction)	0.232	0.571	0.196	0.35
KRh@MFI-Cal-CO/H_2	0.169	0.649	0.182	0.61

*The error metric is provided as lack of fit (LOF).

While similar trends are obtained from both LCF and MCR analyses, the MCR allowed a better reconstruction of the sample spectra. Supplementary Fig. 60a compares the reference spectra with the obtained MCR components, where the difference between the third component and $Rh(CO)_2(acac)$ standard spectrum are highlighted by dashed lines. The catalyst KRh@MFI-CalRed-CO spectrum can now be satisfactorily reconstructed without requiring any Rh^{3+} contribution, in agreement with the IR data. To quantify the average Rh oxidation state would imply to know the oxidation state corresponding to the MCR 3rd component spectrum. Comparing the here reported results with the IR spectra it seems that the MCR 3rd component corresponds to overlapping Rh^+ and Rh^{3+} contributions.



Supplementary Fig. 60. XAS analysis. (a) MCR components (solid) and the corresponding reference XANES spectra (dotted). (b) Normalized XANES spectra of the samples. (c) MCR component concentration fraction (the color code is consistent across panels a, b, and c). The arrows indicate the correspondence between the spectra and their respective concentration profiles.

Supplementary Table 20. EXAFS fitting results. EXAFS analysis using Multi (k^1, k^2, k^3)-weighted fits carried out in r-space (1-3.2 Å) over a k-range of 3-13.5 $Å^{-1}$ using a Hannings window (dk 1), and $S_0^2 = 0.9$. Bond distances and disorder parameters (Δr_{eff} and σ^2) were allowed to float having initial values of 0.0 Å and 0.003 $Å^2$ respectively, with a universal E_0 and $\Delta E_0 = 0$ eV.

KRh@MFI-Cal (Before reaction)

	R_{FACTOR}	X^2_ν	Var. No.	k-range ($Å^{-1}$)	r-range (Å)	ΔE_0 (eV)
	0.023	15.7	4	3-13.5	1-3.2	−3.4(1.3)

PATHS

Rh-C/N/O	**CN**	**r (Å)**	**σ^2 (x10^3 $Å^2$)**
	4.8	2.04 (0.01)	3.0 (0.5)
Rh-Rh	**CN**	**r (Å)**	**σ^2 (x10^3 $Å^2$)**
	1.0	3.09 (0.01)	4.6 (1.3)

KRh@MFI-CalRed-CO

	R_{FACTOR}	X^2_ν	Var. No.	k-range ($Å^{-1}$)	r-range (Å)	ΔE_0 (eV)
	0.009	0.8	**7**	3-13.5	1-3.2	−5.6 (0.7)

PATHS

Rh-C (Rh-CO)	**CN**	**r (Å)**	**σ^2 (x10^3 $Å^2$)**
	0.85	1.79 (0.01)	3.4 (1.3)
Rh-O (Rh_2O_3)	**CN**	**r (Å)**	**σ^2 (x10^3 $Å^2$)**
	1.0	1.93 (0.01)	5.0 (1.2)
Rh-Rh (Rh^0)	**CN**	**r (Å)**	**σ^2 (x10^3 $Å^2$)**
	2.0	2.73 (0.01)	5.7 (0.4)
Rh-O (Rh-CO)	**CN**	**r (Å)**	**σ^2 (x10^3 $Å^2$)**
	0.85	2.94 (0.01)	3.4 (1.3)
Rh-O-C (Rh-CO)	**CN**	**r (Å)**	**σ^2 (x10^3 $Å^2$)**
	1.28	2.94 (0.01)	3.4 (1.3)

KRh@MFI-Cal (After reaction)

	R_{FACTOR}	X^2_ν	Var. No.	k-range ($Å^{-1}$)	r-range (Å)	ΔE_0 (eV)
	0.011	1.3	**7**	3-13.5	1-3.2	−4.8 (0.8)

PATHS

Rh-C (Rh-CO)	**CN**	**r (Å)**	**σ^2 (x10^3 $Å^2$)**
	0.8	1.80 (0.01)	2.6 (1.3)
Rh-O (Rh_2O_3)	**CN**	**r (Å)**	**σ^2 (x10^3 $Å^2$)**
	1.9	2.0 (0.01)	6.6 (1.0)
Rh-Rh (Rh^0)	**CN**	**r (Å)**	**σ^2 (x10^3 $Å^2$)**
	2.0	2.72 (0.01)	5.6 (0.4)
Rh-O (Rh-CO)	**CN**	**r (Å)**	**σ^2 (x10^3 $Å^2$)**
	0.8	2.95 (0.01)	2.6 (1.3)
Rh-O-C (Rh-CO)	**CN**	**r (Å)**	**σ^2 (x10^3 $Å^2$)**
	1.2	2.95 (0.01)	2.6 (1.3)

KRh@MFI-Cal-500MP (After reaction)

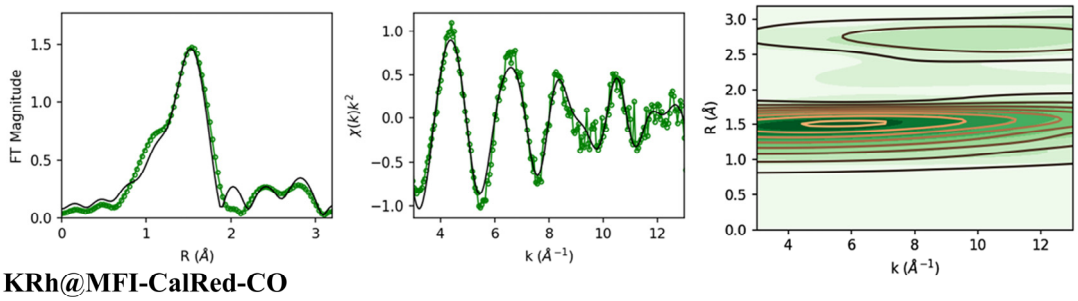
	R_{FACTOR}	X^2_ν	Var. No.	k-range ($Å^{-1}$)	r-range (Å)	ΔE_0 (eV)
	0.014	1.6	**7**	3-13.5	1-3.2	−3.4 (1.0)

PATHS

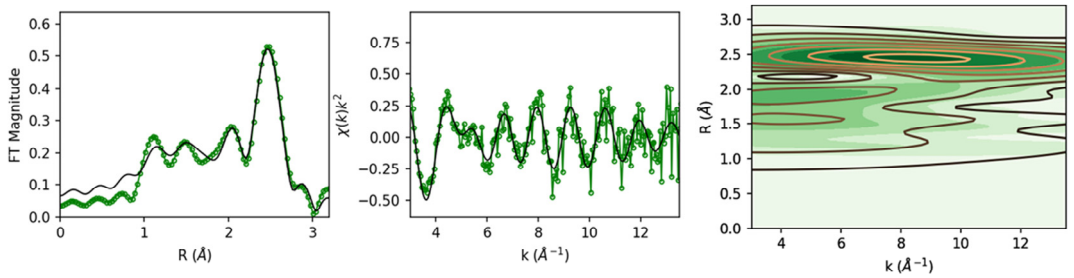
Rh-C (Rh-CO)	**CN**	**r (Å)**	**σ^2 (x10^3 $Å^2$)**
	0.5	1.80 (0.02)	3.1 (2.5)
Rh-O (Rh_2O_3)	**CN**	**r (Å)**	**σ^2 (x10^3 $Å^2$)**
	2.0	2.01 (0.01)	5.5 (0.8)
Rh-Rh (Rh^0)	**CN**	**r (Å)**	**σ^2 (x10^3 $Å^2$)**
	2.0	2.71 (0.01)	6.2 (0.6)
Rh-O (Rh-CO)	**CN**	**r (Å)**	**σ^2 (x10^3 $Å^2$)**
	0.5	2.95 (0.02)	3.1 (2.5)
Rh-O-C (Rh-CO)	**CN**	**r (Å)**	**σ^2 (x10^3 $Å^2$)**
	0.75	2.95 (0.02)	3.1 (2.5)

KRh@MFI-Cal-CO/H_2						
	R_{FACTOR}	**X^2_ν**	**Var. No.**	**k-range ($Å^{-1}$)**	**r-range (Å)**	**ΔE_0 (eV)**
	0.018	15.7	**7**	3-13.5	1-3.2	−1.1 (1.6)
PATHS						
Rh-C (Rh-CO)	**CN**		**r (Å)**		**σ^2 (x10^3 $Å^2$)**	
	0.55		1.86 (0.03)		4.0 (3.6)	
Rh-O (Rh_2O_3)	**CN**		**r (Å)**		**σ^2 (x10^3 $Å^2$)**	
	2.1		2.03 (0.01)		5.7 (1.0)	
Rh-Rh (Rh^0)	**CN**		**r (Å)**		**σ^2 (x10^3 $Å^2$)**	
	2.0		2.75 (0.01)		4.4 (1.2)	
Rh-O (Rh-CO)	**CN**		**r (Å)**		**σ^2 (x10^3 $Å^2$)**	
	0.55		3.0 (0.03)		4.0 (3.6)	
Rh-O-C (Rh-CO)	**CN**		**r (Å)**		**σ^2 (x10^3 $Å^2$)**	
	0.83		3.0 (0.03)		4.0 (3.6)	

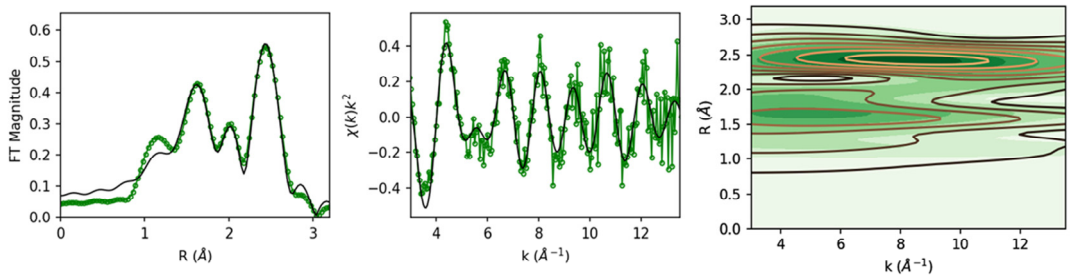
KRh@MFI-Cal (Before reaction)



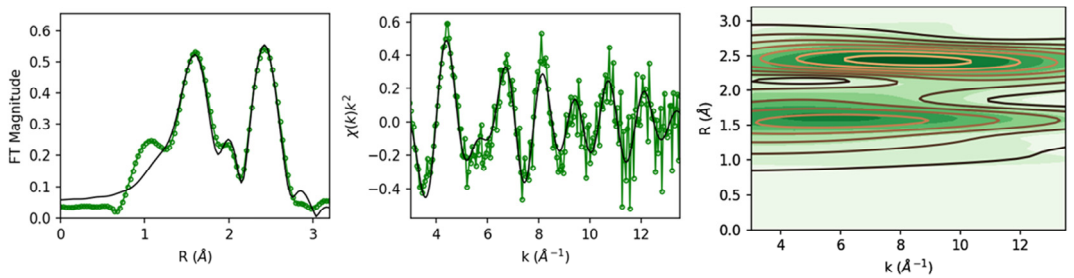
KRh@MFI-CalRed-CO



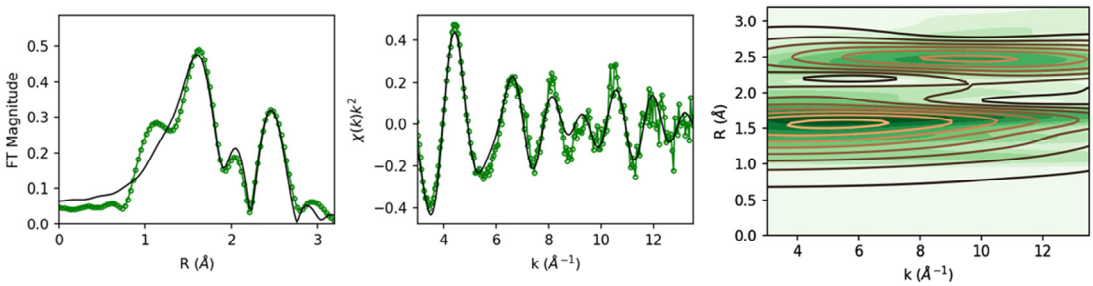
KRh@MFI-Cal (After reaction)



KRh@MFI-Cal-500MP (After reaction)



KRh@MFI-Cal-CO/H_2



Supplementary Fig. 61. EXAFS fitting results. EXAFS fitting results of KRh@MFI samples presented in **Supplementary Table 20**.

3.5. 1-Decene hydroformylation on Rh@zeolite with different topology type zeolite

Herein, Rh@Na-FER sample was synthesized by a one-pot hydrothermal method using colloidal silica (Ludox AS-40) as the silica source and ethylenediamine (EDA) as the organic template. Briefly, 0.33g of $NaAlO_2$, 0.077g of NaOH, and 12.9g of Milli-Q water were mixed under stirring to get transparent solution. Then, Ludox AS-40, 1.83g of EDA, 1.63g Milli-Q water and desired amount of Rh-EDA solution were added separately. The resulting synthesis gel was stirred for 2h before being transferred into a 35 mL Teflon-lined stainless-steel autoclave and crystallized at 175 ^oC under continuous agitation for 3 days. After crystallization, the solid product was recovered by filtration, thoroughly washed with deionized water, and dried overnight at 80 ^oC. The organic template was subsequently removed by calcination in air (RT to 550 °C, 1.5 °C/min and held at 550 °C for 6h). The obtained sample was named Rh@Na-FER-Cal.

Rh@Na-FAU sample was synthesized by a one-pot hydrothermal method using a synthesis gel with a molar composition of SiO_2: Al_2O_3: Na_2O: H_2O = 7.8: 1: 2.2: 174. Typically, 8g Ludox AS-40, 1.12g $NaAlO_2$, 0.66g NaOH, 14.36 g Milli-Q water and desired amount of Rh-EDA solution were mixed and kept stirring overnight. The resulting synthesis gel was transferred to a 35 mL Teflon-lined stainless-steel autoclave and crystallized statically at 100 °C for 4 days. After crystallization, the solid product was recovered by filtration, thoroughly washed with deionized water, and dried overnight at 80 ^oC. The organic template was subsequently removed by calcination in air (RT to 550 °C, 1.5 °C/min and held at 550 °C for 6 h). The obtained sample was named Rh@Na-FAU-Cal.

The samples show good crystallinity based on the XRD pattern and STEM images (Supplementary Fig. 62 and Fig. 63, respectively).

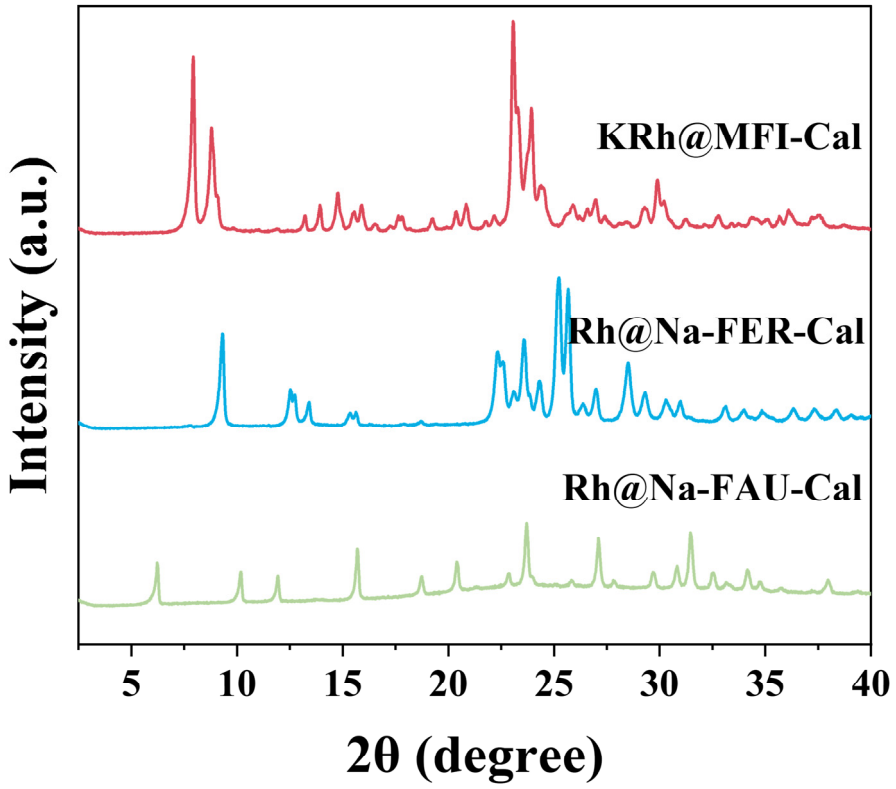
As shown in Supplementary Table 22 and Supplementary Fig. 64 and 65, both Rh@Na-FER and Rh@Na-FAU exhibit pronounced olefin isomerization. Upon the addition of MP or NMP, both the isomerization and hydroformylation activities are significantly suppressed. This could be related on the one hand to an accumulation of MP/NMP inside the zeolite channels (as found from the elemental analysis, see Supplementary Table 23), which restrict the access of the olefin to the active sites lowering catalytic activity, and on the other hand to a different local environment of Rh^+ (as evidenced from the IR-CO studies, see Supplementary Fig. 66 and 67) which makes MP/NMP interaction weaker and not so efficient as in the KRh@MFI zeolite.

Thus, the additives alone are not enough to achieve high regioselectivity. Instead, the combination of the MFI zeolite topology (silicalite-1), confined Rh^{3+} active sites, and MP/NMP additives are essential for highly regioselective α-olefin hydroformylation.

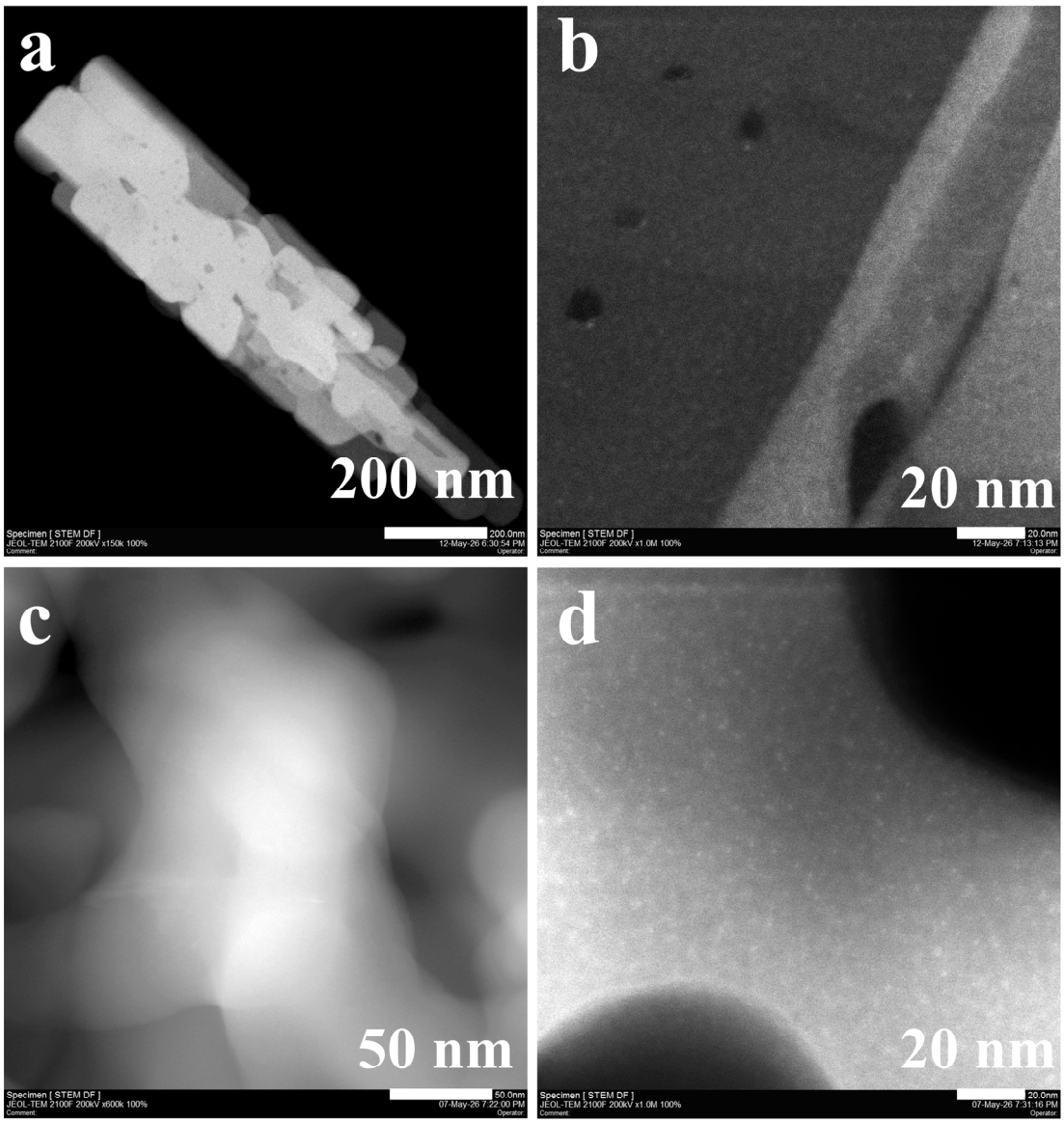
Supplementary Table 21. Characterizations. Physicochemical properties of Rh-based catalysts.

Catalysts	K (wt%) [a]	Na (wt%) [a]	Al (wt%) [a]	Si/Al molar ratio [a]	Rh (wt%) [a]
KRh@MFI-Cal	1.0	-	-	-	0.20
Rh@Na-FER-Cal	-	1.5	6.0	6.2	0.10
Rh@Na-FAU-Cal	-	10.6	10.4	3.0	0.13

[a] Measured by inductively coupled plasma optical emission spectroscopy (ICP-OES) analysis.

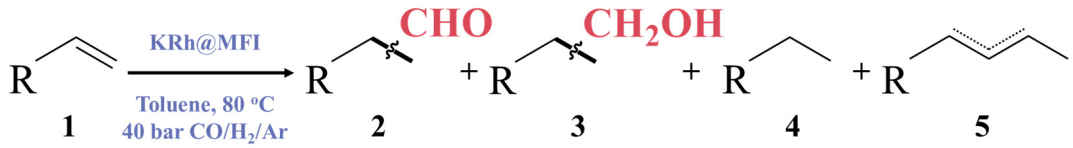


Supplementary Fig. 62. X-ray diffraction results. XRD of KRh@MFI-Cal, Rh@Na-FER-Cal and Rh@Na-FAU-Cal samples.



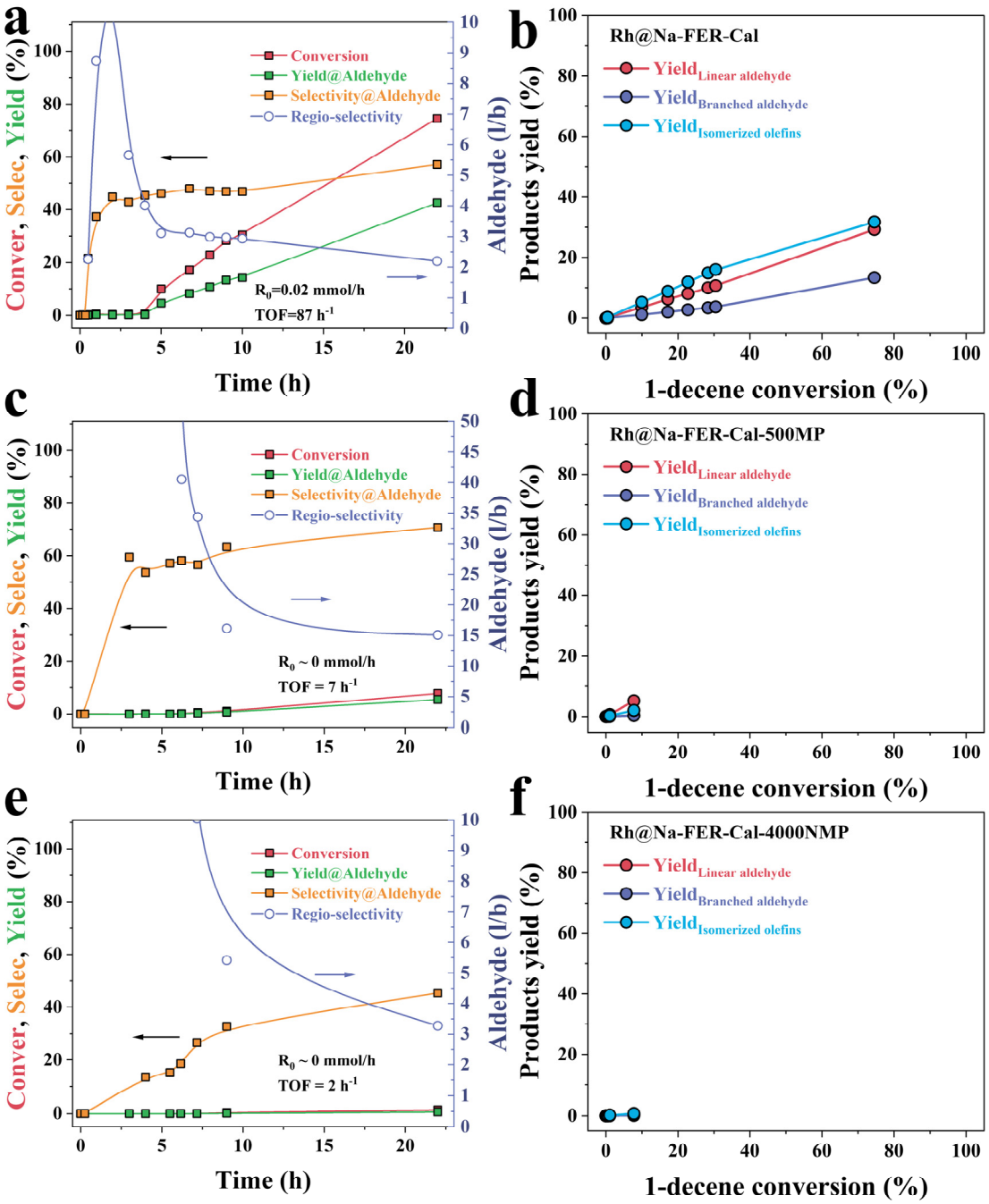
Supplementary Fig. 63. Microscopic results. STEM images of (a, b) Rh@Na-FER-Cal, and (c, d) Rh@Na-FAU-Cal-catalysts.

Supplementary Table 22. 1-Decene hydroformylation activity. Catalytic results for KRh@MFI-Cal, Rh@Na-FER-Cal, and Rh@Na-FAU catalysts of 1-decene hydroformylation at 80 ºC.[a]

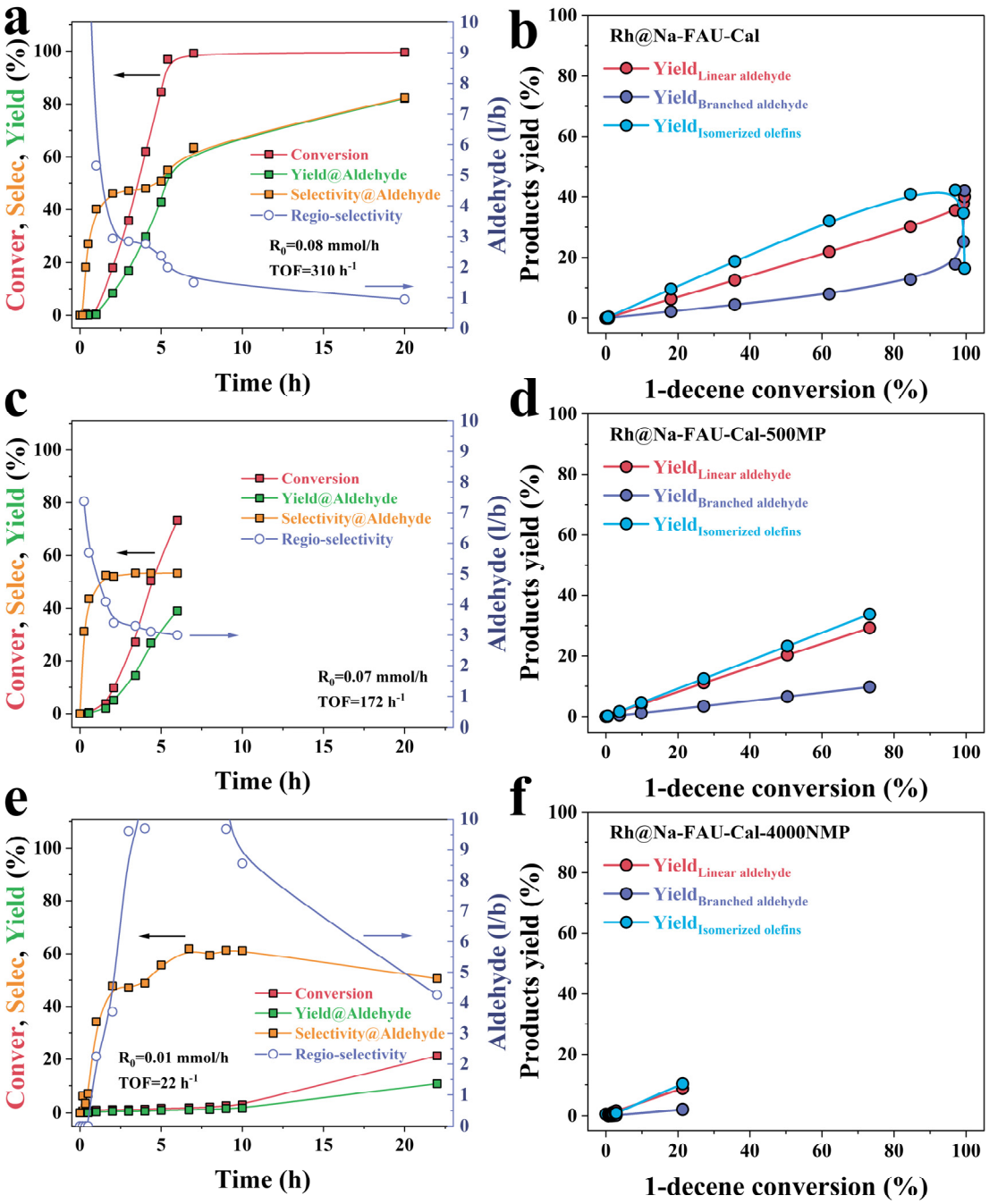


Entry	Catalysts	Conv. (%)	Selec. (%) Aldehyde (L)[b]	l/b[c]	Yield (%)				R_0 (mmol/h)[d] L-Aldehyde	R_0 (mmol/h)[d] Iso-Alkenes	TON[e]	TOF (h^{-1})[f]
					2	3	4	5				
1	KRh@MFI-Cal	99.4	92.1 (89.2)	30	91.6	0	1.2	6.6	0.85	0.036	2137	2096
2	KRh@MFI-Cal-500MP	98.5	96.8 (96.5)	378	95.3	0	0.5	2.6	0.82	0.018	2279	2052
4[g]	KRh@MFI-Cal-4000NMP	99.8	95.9 (95.8)	817	95.7	0	1.0	3.1	0.67	0.017	2406	1706
5[h]	Rh@Na-FER-Cal	74.5	57.2 (39.3)	2.2	42.6	0	0.2	31.7	0.02	0.040	1543	87
6[h]	Rh@Na-FER-Cal-500MP	7.8	70.7 (66.3)	15	5.5	0	0.3	2.0	1.4×10^{-3}	0.19×10^{-3}	199	7
7[h]	Rh@Na-FER-Cal-4000NMP	1.3	45.4 (34.8)	3.3	0.6	0	0	0.7	0.5×10^{-3}	0.27×10^{-3}	211	2
8[i]	Rh@Na-FAU-Cal	99.3	63.6 (38.2)	1.5	63.1	0	1.5	34.7	0.08	0.117	1523	310
9[j]	Rh@Na-FAU-Cal-500MP	73.2	53.3 (39.9)	3.0	39.0	0	0.5	33.8	0.07	0.08	790	172
10[h]	Rh@Na-FAU-Cal-4000NMP	15.4	50.6 (40.9)	4.3	7.8	0	0.2	7.4	0.01	0.008	321	22

[a] Reaction conditions: 1 mmol LAO, 20 mg catalyst, 20 mg isooctane (internal standard), 4 mL toluene, 40 bar $CO/H_2/Ar$ (45/45/10 vol%), 80 ºC, 800 rpm and 3h reaction.
[b] Total aldehyde selectivity (L=Linear aldehyde selectivity).
[c] Ratio of the linear aldehyde to the branched aldehyde.
[d] Reaction rate for linear aldehyde formation and reaction rate for isomerized alkenes formation, mmol/h, calculated when LAO conversion is < 20%.
[e] mmol of linear aldehyde/total mmol of Rh at 3h reaction time.
[f] Rate for the formation of linear aldehyde/total mmol of Rh.
[g] 9h reaction.
[h] 22h reaction.
[i] 7h reaction.
[j] 6h reaction.



Supplementary Fig. 64. 1-Decene hydroformylation. (a) Time profiles of activity on Rh@Na-FER-Cal catalyst and (b) yield of linear aldehyde, branched aldehyde, isomerized olefins as a function of 1-decene conversion. (c) Time profiles of activity Rh@Na-FER-Cal-500MP catalyst and (d) yield of linear aldehyde, branched aldehyde, isomerized olefins as a function of 1-decene conversion. (e) Time profiles of activity Rh@Na-FER-Cal-4000NMP catalyst and (f) yield of linear aldehyde, branched aldehyde, isomerized olefins as a function of 1-decene conversion. Reaction condition: 1 mmol LAO, 20 mg catalyst, 20 mg isooctane (internal standard), 4 mL toluene, 40 bar $CO/H_2/Ar$ (45/45/10 vol%), 80 ºC, 800 rpm, R_0, TOF and TON are values for linear aldehyde formation.



Supplementary Fig. 65. 1-Decene hydroformylation. (a) Time profiles of activity on Rh@Na-FAU-Cal catalyst and (b) yield of linear aldehyde, branched aldehyde, isomerized olefins as a function of 1-decene conversion. (c) Time profiles of activity Rh@Na-FAU-Cal-500MP catalyst and (d) yield of linear aldehyde, branched aldehyde, isomerized olefins as a function of 1-decene conversion. (e) Time profiles of activity Rh@Na-FAU-Cal-4000NMP catalyst and (f) yield of linear aldehyde, branched aldehyde, isomerized olefins as a function of 1-decene conversion. Reaction condition: 1 mmol LAO, 20 mg catalyst, 20 mg isooctane (internal standard), 4 mL toluene, 40 bar $CO/H_2/Ar$ (45/45/10 vol%), 80 ºC, 800 rpm, R_0, TOF and TON are values for linear aldehyde formation.

Supplementary Table 23. Characterizations. Elemental analysis results on Rh@Na-FER catalysts.

Sample	C (wt%) [a]	H (wt%) [a]	N (wt%) [a]	S (wt%) [a]	Rh (wt%) [b]	MP/Rh molar ratio [c]
Rh@Na-FER-Cal-500MP (After reaction)	2.10	1.37	0.78	0	0.1	57
Rh@Na-FER-Cal-4000NMP (After reaction)	1.90	1.34	0.62	0	0.1	46

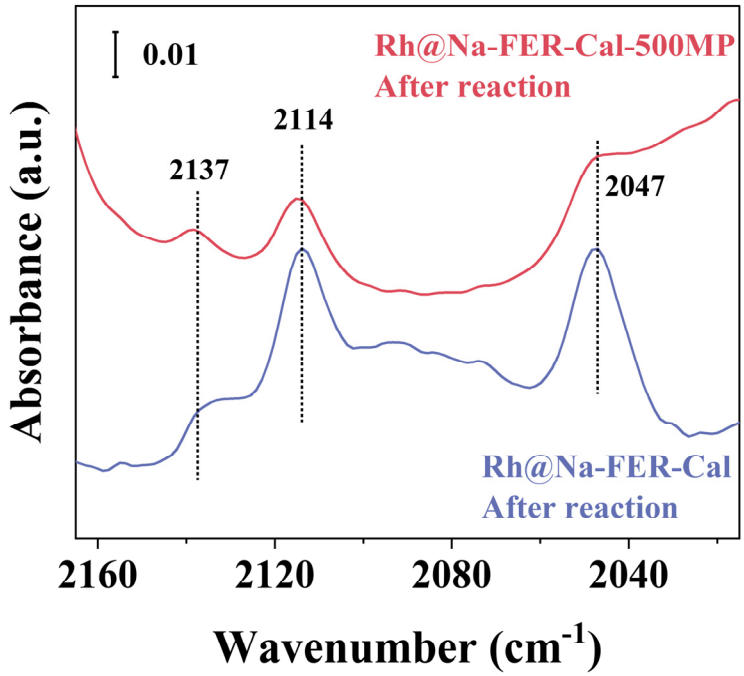
[a] Measured by elemental analysis.
[b] Measured by ICP-AES.
[c] The MP content was calculated based on the nitrogen content, and the molar ratio of residual MP to Rh in the catalyst was determined.

Herein, IR-CO studies on the Rh@Na-FER-Cal and Rh@Na-FAU-Cal samples, after reaction in the presence of MP and compared to the corresponding samples in absence of MP additive.

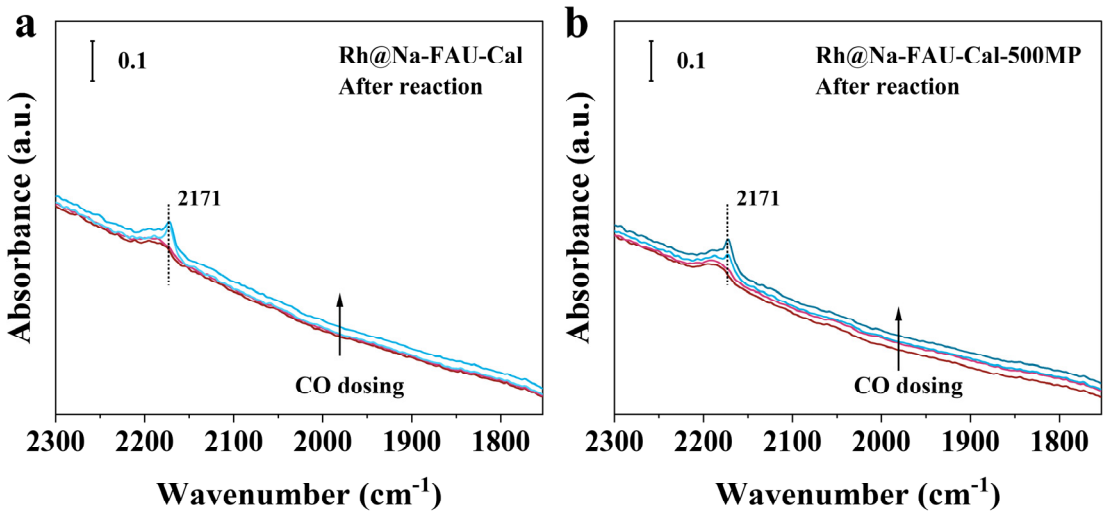
In the case of the Rh@Na-FER-Cal sample (Supplementary Fig. 66), both Rh^{3+} (2137 cm^{-1}) and Rh^{+} (2114 and 2047 cm^{-1}) are not influenced by the addition of MP. Furthermore, the $Rh^{+}(CO)_2$ dicarbonyl vibration appears at 2114 and 2047 cm^{-1}, which differs to that obtained in the KRh@MFI-Cal-500MP sample (2065 and 1996 cm^{-1}). These differences are related to the different Rh^{+} Lewis acidity related to the different zeolite topology.

The absence of the Rh^{+} site blocking in the presence of MP could be related to the lower Lewis acidity of the Rh^{+} site which may influence the MP interaction.

In the case of the Rh@Na-FAU-Cal sample, the only signal we found is relative to Na^{+}-CO[58] (2171 cm^{-1}; see Supplementary Fig. 67), which is due to the high Na loading in the sample (10.6wt% Na loading based on ICP-OES analysis, Supplementary Table 23).



Supplementary Fig. 66. IR-CO results. IR-CO at –65 ºC and 2 mbar CO coverage spectra for Rh@FER-Cal and Rh@FER-Cal-500MP, both after 1-decene hydroformylation reactions.



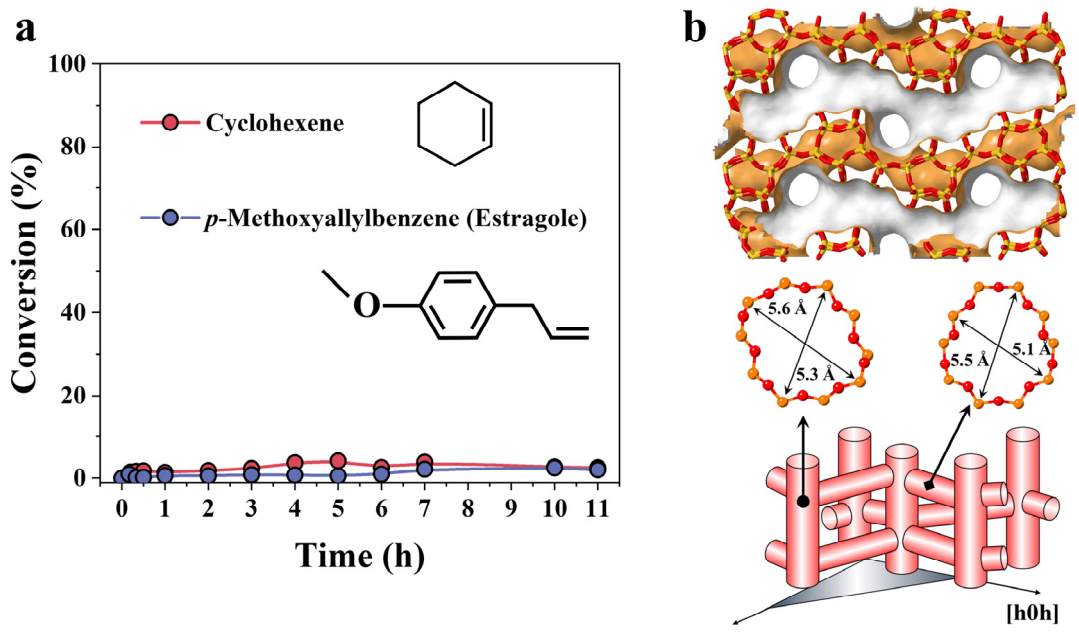
Supplementary Fig. 67. IR-CO results. IR-CO at −65 ºC and at increasing CO coverage (0.01-2 mbar) for (a) Rh@Na-FAU-Cal and (b) Rh@Na-FAU-Cal-500MP after 1-decene hydroformylation reactions.

3.6. Hydroformylation of bulky olefins over KRh@MFI-Cal

Herein, the hydroformylation of cyclohexene and *p*-methoxyallylbenzene over KRh@MFI-Cal catalyst were investigated. Both substrates exhibited nearly ~0% activity over 11h reaction (Supplementary Fig. 68a). No Rh leaching was observed in both cases. The ~0% activity can be attributed to the relatively large kinetic diameter of cyclohexene (5.85-6.0 Å)[59,60], which is comparable to or exceeds the pore aperture of MFI zeolite channels (Supplementary Fig. 68b).

Even if partial diffusion into the MFI channels is possible due to zeolite framework flexibility, the subsequent C=C coordination to the Rh center preferentially located in the sinusoidal channels is still strongly hindered, as cyclohexene lacks sufficient conformational adaptability to properly align its double bond within the confined environment. Moreover, the corresponding hydroformylation product (cyclohexanecarboxaldehyde), bearing an additional aldehyde substituent and a rigid chair conformation, is unable to diffuse out of the MFI channels due to increased steric constraints.

A similar explanation can be applied to *p*-methoxyallylbenzene and other bulky cyclic substrates with large kinetic diameters.



Supplementary Fig. 68. Hydroformylation of bulky olefins over KRh@MFI-Cal. (a) Cyclohexene and *p*-methoxyallybenzene hydroformylation on KRh@MFI-Cal catalyst. Reaction condition: 1 mmol LAO, 20 mg catalyst, 20 mg isooctane (internal standard), 4 mL toluene, 40 bar $CO/H_2/Ar$ (45/45/10 vol%), 80 ºC, 800 rpm. (b) Illustration of MFI zeolite channel and corresponding straight channel size and sinusoidal channel size.

3.7. Summary of the identification of Rh species by IR-CO

Supplementary Table 24. Rh carbonyl assignments. Vibrational frequencies of gem-dicarbonyls, linear carbonyls, and bridged carbonyls of rhodium supported on zeolites and metal oxides.

Initial forms of catalyst	Pre-treatment	Temperature of IR-CO (°C)	O-RhCO		ν_s Rh(CO)$_2$	ν_{as} Rh(CO)$_2$	RhCO	Rh$_2$CO	Ref
			Rh^{3+}	Rh^{2+}	Rh^+	Rh^+	Rh^0	Rh^0	
Supported molecular Rh complex									
$Rh(C_2H_4)_2$/H-Beta	None	25			2115	2048			61
$Rh(CO)_2$/DAY zeolite	None	25			2116	2050			62
$Rh(C_2H_4)_2$/SAPO 37	None	25			2115	2052			63
$Rh(C_2H_4)_2$/ZSM-5	None	25			2116	2049			64
$Rh(C_2H_4)_2$/HY	None	25			2118	2052			61
$RhCl_3 \cdot 3H_2O/Al_2O_3$	None	25	2135		2088	2016			65
$Rh_6(CO)_{16}/Al_2O_3$	CO, 25 °C	25			2095	2020			65
$Rh_6(CO)_{16}/Al_2O_3$	O_2, 200 °C	200	2135						65
$Rh_6(CO)_{16}/Al_2O_3$	CO, 100 °C	100			2095	2020			65
$RhCl_3/SiO_2$	He, 30 °C	30	2145		2102	2036			66
$RhCl_3 \cdot 3H_2O/Al_2O_3$	Vacuum	25	2136		2098	2029			67
$RhCl_3 \cdot 3H_2O/Al_2O_3$	H_2, 150-400 °C	25			2096-2102	2022-2032	2042-2076	1845-1875	67
Supported Rh nanoparticles/clusters/atoms									
Rh/Al_2O_3	H_2 500 °C, then O_2 27 °C	27		2128	2110	2038			68
Rh/NaY			2138						69
Rh/HY	H_2, 300 °C	50			2114, 2100	2049, 2025	1990	1843	70
Rh/KY	H_2, 300 °C	50			2109, 2092	2042, 2014	1999	1812	70
Rh/SiO_2	H_2, 350 °C	25					2067	1901	71
Rh/Al_2O_3	H_2, 250 °C	23		2120	2091	2020		1810-1835	72
Rh/Al_2O_3	H_2, 100 °C		2142	2120	2090	2017			73
Rh/SiO_2	H_2, 200 °C	25			2104	2042	2048-2067	1900-1925	74
Rh/DAY zeolite	Air, 400 °C	25			2118	2053			75
	H_2, 300 °C	25			2093	2036	2075	1860	75
Rh/Na-Y zeolite	CO, 100 °C	25			2086	2010			76
Rh/TiO_2	H_2, 200 °C	−120			2097	2031			77
	H_2, 300 °C	−120			2094	2030	2070		77
	H_2, 300 °C	25			2094	2027			77
Rh/DeAl-Beta	H_2, 200 °C	30			2093-2113	2037-2048	2069	1915	78
RhZn/DeAl-Beta	H_2, 200 °C	30			2096	2030	2066		78
RhCo/DeAl-Beta	H_2, 200 °C	30			2096	2025	2064		78

4. Reference

1. Simonelli, L. *et al.* CLÆSS: The hard X-ray absorption beamline of the ALBA CELLS synchrotron. *Cogent Phys.* **3**, 1231987 (2016).
2. Ravel, B. & Newville, M. ATHENA, ARTEMIS, HEPHAESTUS: data analysis for X-ray absorption spectroscopy using IFEFFIT. *J. Synchrotron Radiat.* **12**, 537-541 (2005).
3. Newville, M. EXAFS analysis using FEFF and FEFFIT. *J. Synchrotron Radiat.* **8**, 96-100 (2001).
4. Rehr, J. J. & Albers, R. C. Theoretical approaches to x-ray absorption fine structure. *Rev. Mod. Phys.* **72**, 621-654 (2000).
5. Newville, M. Larch: An Analysis Package for XAFS and Related Spectroscopies. *J. Phys. Conf. Ser.* **430**, 012007 (2013).
6. Perdew, J. P. *et al.* Atoms, molecules, solids, and surfaces: Applications of the generalized gradient approximation for exchange and correlation. *Phys. Rev. B* **46**, 6671-6687 (1992).
7. Perdew, J. P. & Wang, Y. Accurate and simple analytic representation of the electron-gas correlation energy. *Phys. Rev. B* **45**, 13244-13249 (1992).
8. Kresse, G. & Furthmüller, J. Efficient iterative schemes for ab initio total-energy calculations using a plane-wave basis set. *Phys. Rev. B* **54**, 11169-11186 (1996).
9. Blöchl, P. E. Projector augmented-wave method. *Phys. Rev. B* **50**, 17953-17979 (1994).
10. Henkelman, G. & Jónsson, H. A dimer method for finding saddle points on high dimensional potential surfaces using only first derivatives. *J. Chem. Phys.* **111**, 7010-7022 (1999).
11. Grimme, S., Antony, J., Ehrlich, S. & Krieg, H. A consistent and accurate ab initio parametrization of density functional dispersion correction (DFT-D) for the 94 elements H-Pu. *J. Chem. Phys.* **132**, 154104 (2010).
12. Neese, F. The ORCA program system. *WIREs Comput. Mol. Sci.* **2**, 73-78 (2012).
13. Zhao, M. *et al.* Low-temperature hydroformylation of ethylene by phosphorous stabilized Rh sites in a one-pot synthesized Rh-(O)-P-MFI zeolite. *Nat. Commun.* **14**, 7174 (2023).
14. Bara-Estaún, A. *et al.* Multi-nuclear, high-pressure, operando Flow NMR spectroscopic study of Rh/PPh_3-catalysed hydroformylation of 1-hexene. *Faraday Discuss.* **229**, 422-442 (2021).
15. Zhang, X. *et al.* Regioselective hydroformylation of propene catalysed by rhodium-zeolite. *Nature* **629**, 597-602 (2024).
16. Evans, D., Osborn, J. A. & Wilkinson, G. Hydroformylation of alkenes by use of rhodium complex catalysts. *J. Chem. Soc. A*, 3133-3142 (1968).
17. Dou, X. *et al.* Structure-Reactivity Relationship of Zeolite-Confined Rh Catalysts for Hydroformylation of Linear α-Olefins. *J. Am. Chem. Soc.* **147**, 2726-2736 (2025).
18. Sun, G., Fan, S., Lv, J. & Zhao, T. Effective hollow Rh@H-S-1 catalyst for hydroformylation of 1-hexene. *J. Catal.* **439**, 115770 (2024).
19. Zhang, J. *et al.* Enhancing regioselectivity via tuning the microenvironment in heterogeneous hydroformylation of olefins. *J. Catal.* **387**, 196-206 (2020).
20. Huang, L. *et al.* Tuning the regioselectivity of heterogeneous hydroformylation by engineering carbon species microenvironment around Rh sites. *J. Catal.* **447**, 116095 (2025).
21. Yu, Z. *et al.* Suppressing Metal Leaching and Sintering in Hydroformylation Reaction by Modulating the Coordination of Rh Single Atoms with Reactants. *J. Am. Chem. Soc.* **146**, 11955-11967 (2024).

22. Galdeano-Ruano, C., Lopes, C. W., Motta Meira, D., Corma, A. & Oña-Burgos, P. Rh_2P Nanoparticles Stabilized by Carbon Patches for Hydroformylation of Olefins. *ACS Appl. Nano Mater.* **4**, 10743-10753 (2021).

23. Zhang, X. *et al.* Carbon matrix anchored RhCo single-atom alloy catalyst for robust hydroformylation with wide substrate generality. *AlChE J.* **n/a**, e18798 (2025).

24. Sharma, D., Ganesh, V. & Sakthivel, A. Rhodium incorporated monometallic cobalt hydrotalcite-type materials: Preparation and its applications for the hydroformylation of alkenes. *Appl. Catal., A* **555**, 155-160 (2018).

25. Sun, Z. *et al.* Poly(ethylene glycol)-stabilized Rh nanoparticles as efficient and recyclable catalysts for hydroformylation of olefins. *Catal. Commun.* **27**, 78-82 (2012).

26. Bruss, A. J., Gelesky, M. A., Machado, G. & Dupont, J. Rh(0) nanoparticles as catalyst precursors for the solventless hydroformylation of olefins. *J. Mol. Catal. A: Chem.* **252**, 212-218 (2006).

27. Chen, M. *et al.* Intermetallic Nanocatalyst for Highly Active Heterogeneous Hydroformylation. *J. Am. Chem. Soc.* **143**, 20907-20915 (2021).

28. Tan, M. *et al.* Active and regioselective rhodium catalyst supported on reduced graphene oxide for 1-hexene hydroformylation. *Catal. Sci. Technol.* **6**, 1162-1172 (2016).

29. Sun, G. *et al.* In situ synthesis of Rh@NaX catalyst for 1-hexene hydroformylation. *Fuel* **373**, 132327 (2024).

30. Shang, W. *et al.* Efficient Heterogeneous Hydroformylation over Zeolite-Encaged Isolated Rhodium Ions. *CCS Chem.* **5**, 1526-1539 (2022).

31. Tan, M. *et al.* Enhancing catalytic performance of activated carbon supported Rh catalyst on heterogeneous hydroformylation of 1-hexene via introducing surface oxygen-containing groups. *Appl. Catal., A* **527**, 53-59 (2016).

32. Yang, D. *et al.* Construction of $Rh\text{-}N_4$ single atoms and Rh clusters dual-active sites for synergistic heterogeneous hydroformylation of olefins with ultra-high turnover frequency. *Chem. Eng. J.* **479**, 147505 (2024).

33. Li, C. *et al.* Xantphos doped Rh/POPs-PPh_3 catalyst for highly selective long-chain olefins hydroformylation: Chemical and DFT insights into Rh location and the roles of Xantphos and PPh_3. *J. Catal.* **353**, 123-132 (2017).

34. Zhu, H. J. *et al.* The PPh_3 ligand modified Rh/SiO_2 catalyst for hydroformylation of olefins. *Catal. Today* **93-95**, 389-393 (2004).

35. Mukhopadhyay, K., Mandale, A. B. & Chaudhari, R. V. Encapsulated $HRh(CO)(PPh_3)_3$ in Microporous and Mesoporous Supports: Novel Heterogeneous Catalysts for Hydroformylation. *Chem. Mater.* **15**, 1766-1777 (2003).

36. Casey, C. P. *et al.* Diphosphines with natural bite angles near 120º increase selectivity for n-aldehyde formation in rhodium-catalyzed hydroformylation. *J. Am. Chem. Soc.* **114**, 5535-5543 (1992).

37. Jia, X., Wang, Z., Xia, C. & Ding, K. Spiroketal-Based Phosphorus Ligands for Highly Regioselective Hydroformylation of Terminal and Internal Olefins. *Chem. Eur. J.* **18**, 15288-15295 (2012).

38. Yan, Y., Zhang, X. & Zhang, X. A Tetraphosphorus Ligand for Highly Regioselective Isomerization-Hydroformylation of Internal Olefins. *J. Am. Chem. Soc.* **128**, 16058-16061 (2006).

39. Yu, S. *et al.* Synthesis and Application of Tetraphosphane Ligands in Rhodium-Catalyzed Hydroformylation of Terminal Olefins: High Regioselectivity at High Temperature. *Chem. Eur. J.* **16**, 4938-4943 (2010).

40. Chen, C., Qiao, Y., Geng, H. & Zhang, X. A Novel Triphosphoramidite Ligand for Highly

Regioselective Linear Hydroformylation of Terminal and Internal Olefins. *Org. Lett.* **15**, 1048-1051 (2013).

41. Liu, Y. *et al.* Rhodium nanoparticles supported on silanol-rich zeolites beyond the homogeneous Wilkinson's catalyst for hydroformylation of olefins. *Nat. Commun.* **14**, 2531 (2023).

42. Liu, C., Zhang, J., Liu, H., Qiu, J. & Zhang, X. Heterogeneous Ligand-Free Rhodium Oxide Catalyst Embedded within Zeolitic Microchannel to Enhance Regioselectivity in Hydroformylation. *Ind. Eng. Chem. Res.* **58**, 21285-21295 (2019).

43. Duan, H. *et al.* Ultrathin rhodium nanosheets. *Nat. Commun.* **5**, 3093 (2014).

44. Sun, Q., Dai, Z., Meng, X. & Xiao, F.-S. Enhancement of hydroformylation performance via increasing the phosphine ligand concentration in porous organic polymer catalysts. *Catal. Today* **298**, 40-45 (2017).

45. Sun, Q. *et al.* Highly Efficient Heterogeneous Hydroformylation over Rh-Metalated Porous Organic Polymers: Synergistic Effect of High Ligand Concentration and Flexible Framework. *J. Am. Chem. Soc.* **137**, 5204-5209 (2015).

46. Dong, K. *et al.* Bio-inspired creation of heterogeneous reaction vessels via polymerization of supramolecular ion pair. *Nat. Commun.* **10**, 3059 (2019).

47. Zhao, K. *et al.* Confinement of atomically dispersed Rh catalysts within porous monophosphine polymers for regioselective hydroformylation of alkenes. *J. Catal.* **401**, 321-330 (2021).

48. Sartipi, S. *et al.* Dynamic Release-Immobilization of a Homogeneous Rhodium Hydroformylation Catalyst by a Polyoxometalate Metal-Organic Framework Composite. *ChemCatChem* **7**, 3243-3247 (2015).

49. Raghuvanshi, K. *et al.* Highly Efficient 1-Octene Hydroformylation at Low Syngas Pressure: From Single-Droplet Screening to Continuous Flow Synthesis. *ACS Catal.* **10**, 7535-7542 (2020).

50. Kranenburg, M. *et al.* New Diphosphine Ligands Based on Heterocyclic Aromatics Inducing Very High Regioselectivity in Rhodium-Catalyzed Hydroformylation: Effect of the Bite Angle. *Organometallics* **14**, 3081-3089 (1995).

51. van Rooy, A. *et al.* Bulky Diphosphite-Modified Rhodium Catalysts: Hydroformylation and Characterization. *Organometallics* **15**, 835-847 (1996).

52. van der Slot, S. C., Duran, J., Luten, J., Kamer, P. C. J. & van Leeuwen, P. W. N. M. Rhodium-Catalyzed Hydroformylation and Deuterioformylation with Pyrrolyl-Based Phosphorus Amidite Ligands: Influence of Electronic Ligand Properties. *Organometallics* **21**, 3873-3883 (2002).

53. Breit, B. & Seiche, W. Hydrogen Bonding as a Construction Element for Bidentate Donor Ligands in Homogeneous Catalysis: Regioselective Hydroformylation of Terminal Alkenes. *J. Am. Chem. Soc.* **125**, 6608-6609 (2003).

54. Wei, B. *et al.* Effectively Regulating the Microenvironment of Atomically Dispersed Rh through Co and Pi to Promote the Selectivity in Olefin Hydroformylation. *ACS Appl. Mater. Interfaces* **13**, 15113-15121 (2021).

55. Divekar, S. S., Deshpande, R. M. & Chaudhari, R. V. Kinetics of hydroformylation of 1-decene using homogeneous $HRh(CO)(PPh_3)_3$ catalyst: a molecular level approach. *Catal. Lett.* **21**, 191-200 (1993).

56. Boutros, M. *et al.* Reduced forms of Rh(III) containing MCM-41 silicas as hydrogenation catalysts for arene derivatives. *J. Mol. Catal. A: Chem.* **259**, 91-98 (2006).

57. Clark, A. H., Imbao, J., Frahm, R. & Nachtegaal, M. ProQEXAFS: a highly optimized parallelized rapid processing software for QEXAFS data. *J. Synchrotron Radiat.* **27**, 551-557 (2020).

58. Hadjiivanov, K. I. & Vayssilov, G. N. Characterization of oxide surfaces and zeolites by carbon monoxide as an IR probe molecule. *Adv. Catal.* **47**, 307-511 (2002).

59. Wei, W. *et al.* Thermodynamic and Kinetic Separation Within a Flexible Hydrogen Bonded Organic Framework for Ternary Benzene/Cyclohexene/Cyclohexane Mixture. *Angew. Chem. Int. Ed.* **65**, e19313 (2026).

60. Zhou, D.-D. *et al.* Inversed Benzene/Cyclohexene/Cyclohexane Adsorption Selectivities for One-Step Purification of Cyclohexene and Beyond. *J. Am. Chem. Soc.* **147**, 17342-17349 (2025).

61. Hoffman, A. S., Fang, C.-Y. & Gates, B. C. Homogeneity of Surface Sites in Supported Single-Site Metal Catalysts: Assessment with Band Widths of Metal Carbonyl Infrared Spectra. *J. Phys. Chem. Lett.* **7**, 3854-3860 (2016).

62. Goellner, J. F., Gates, B. C., Vayssilov, G. N. & Rösch, N. Structure and Bonding of a Site-Isolated Transition Metal Complex: Rhodium Dicarbonyl in Highly Dealuminated Zeolite Y. *J. Am. Chem. Soc.* **122**, 8056-8066 (2000).

63. Perez-Aguilar, J. E., Chen, C.-Y., Hughes, J. T., Fang, C.-Y. & Gates, B. C. Isostructural Atomically Dispersed Rhodium Catalysts Supported on SAPO-37 and on HY Zeolite. *J. Am. Chem. Soc.* **142**, 11474-11485 (2020).

64. Shan, J., Li, M., Allard, L. F., Lee, S. & Flytzani-Stephanopoulos, M. Mild oxidation of methane to methanol or acetic acid on supported isolated rhodium catalysts. *Nature* **551**, 605-608 (2017).

65. Smith, A. K. *et al.* Surface-supported metal cluster carbonyls. Chemisorption decomposition and reactivity of hexadecacarbonylhexarhodium supported on alumina, silica-alumina, and magnesia. *Inorg. Chem.* **18**, 3104-3112 (1979).

66. Chuang, S. S. C., Srinivas, G. & Mukherjee, A. Infrared Studies of the Interactions of C_2H_4 and H_2 with $Rh^+(CO)_2$ and CO Adsorbed on $RhCl_3/SiO_2$ and $Rh(NO_3)_3/SiO_2$. *J. Catal.* **139**, 490-503 (1993).

67. Rice, C. A., Worley, S. D., Curtis, C. W., Guin, J. A. & Tarrer, A. R. The oxidation state of dispersed Rh on Al_2O_3. *J. Chem. Phys.* **74**, 6487-6497 (1981).

68. Primet, M. Infrared study of CO chemisorption on zeolite and alumina supported rhodium. *J. Chem. Soc., Faraday Trans. 1 F* **74**, 2570-2580 (1978).

69. Lefebvre, F., Gelin, P., Elleuch, B., Diab, Y. & Taarit, Y. Metal Carbonyl Compounds Entrapped Within Zeolite Cavities. Preparation, Characterization and Catalytic Properties. *Stud. Surf. Sci. Catal.* **18**, 257-272 (1984).

70. Lepage, M. *et al.* Promotion Effects in the Oxidation of CO over Zeolite-Supported Rh Nanoparticles. *J. Phys. Chem. C* **112**, 9394-9404 (2008).

71. Stevenson, S. A., Lisitsyn, A. & Knoezinger, H. Adsorption of carbon monoxide on manganese-promoted rhodium/silica catalysts as studied by infrared spectroscopy. *J. Phys. Chem.* **94**, 1576-1581 (1990).

72. Trautmann, S. & Baerns, M. Infrared Spectroscopic Studies of CO Adsorption on Rhodium Supported by SiO_2, Al_2O_3, and TiO_2. *J. Catal.* **150**, 335-344 (1994).

73. Guerrero-Ruiz, A., Bachiller-Baeza, B., Ferreira-Aparicio, P. & Rodríguez-Ramos, I. Preparation, Characterization, and Activity forn-Hexane Reactions of Alumina-Supported Rhodium-Copper Catalysts. *J. Catal.* **171**, 374-382 (1997).

74. Basu, P., Panayotov, D. & Yates, J. T. Rhodium-carbon monoxide surface chemistry: the involvement of surface hydroxyl groups on alumina and silica supports. *J. Am. Chem. Soc.* **110**, 2074-2081 (1988).

75. Miessner, H. *et al.* The formation of a well defined rhodium dicarbonyl in highly dealuminated rhodium-exchanged zeolite Y by interaction with CO. *J. Chem. Soc., Faraday Trans. 1 F* **85**, 2113-2126 (1989).

76. Conners, L., Hollis, T., Johnson, D. A. & Blyholder, G. Mobility and Clustering of Rh and Ru in Zeolite. Experiment and Theory. *J. Phys. Chem. B.* **102**, 10112-10116 (1998).

77. Zhang, Z., Kladi, A. & Verykios, X. E. Spectroscopic Study of the Effects of Carrier Doping on the Surface Structure of Rh/TiO_2 Catalysts and On Their Interaction with CO and H_2. *J. Phys. Chem.* **98**, 6804-6811 (1994).

78. Qi, L. *et al.* Ethene Hydroformylation Catalyzed by Rhodium Dispersed with Zinc or Cobalt in Silanol Nests of Dealuminated Zeolite Beta. *J. Am. Chem. Soc.* **145**, 2911-2929 (2023).